Stephen E. Schrenk

243 Words

Inclusive and Exclusive Decays of B Mesons to Charmonium States at the Upsilon(4S) Resonance

We have used the CLEO-II detector at the Cornell Electron Storage Ring to study the inclusive and exclusive production of charmonium mesons in a sample of 2.15 million $B\overline{B}$ events. We find inclusive branching fractions of (1.13±0.04±0.06)% for $B \to J/\psi$X, (0.34±0.04±0.03)% for $B \to \psi'$X, and (0.40±0.06±0.04)% for $B \to \chi_{c1}$X. We also find some indication of the inclusive production of χ_{c2}. Momentum spectra for inclusive J/ψ and ψ' production are presented. These measurements are compared to theoretical calculations and are used to probe for evidence of color suppression.

We find exclusive branching fractions or upper limits for B-meson decay to specific final states with only a J/ψ, ψ' or χ_{c1} and a K^-, K^0, K^{*-} or K^{*0}. Of special note, we find branching fractions of (0.104±0.010±0.006)% for $B \to J/\psi K^-$, (0.092±0.018±0.008)% for $B \to J/\psi K^0$, and (0.087±0.025±0.009)% for $B \to \chi_{c1} K^-$. The value of $|a_2|$ in the Wirbel, Stech and Bauer model, as updated by Neubert *et al.*, for two body decays of B mesons is found to be 0.24±0.01±0.01.

The branching fractions presented here are significant improvements over current world averages. In addition to providing interesting tests of strong-interaction phenomena, they are also important engineering numbers for experiments at higher energies, where charmonium production is used as a tag for B-meson decay. Some of the processes studied are CP eigenstates and thus are of interest for future experiments that will search for CP violations in the B-meson sector.

UNIVERSITY OF MINNESOTA

This is to certify that I have examined this bound copy of a doctoral thesis by

Stephen E. Schrenk

and have found that it is complete and satisfactory in all respects and that any and all revisions required by the final examining committee have been made.

Professor Ronald A. Poling
(Faculty Adviser)

GRADUATE SCHOOL

Inclusive and Exclusive Decays of B Mesons to Charmonium States at the Upsilon(4S) Resonance

A THESIS
SUBMITTED TO THE FACULTY OF THE GRADUATE SCHOOL
OF THE UNIVERSITY OF MINNESOTA
BY

Stephen E. Schrenk

IN PARTIAL FULFILLMENT OF THE REQUIREMENTS
FOR THE DEGREE OF
DOCTOR OF PHILOSOPHY

July, 1994

Inclusive and Exclusive Decays of B Mesons to Charmonium States at the Upsilon(4S) Resonance

by Stephen E. Schrenk

Under the supervision of Professor Ronald A. Poling

ABSTRACT

We have used the CLEO-II detector at the Cornell Electron Storage Ring to study the inclusive and exclusive production of charmonium mesons in a sample of 2.15 million $B\overline{B}$ events. We find inclusive branching fractions of $(1.13\pm0.04\pm0.06)\%$ for $B\to J/\psi$X, $(0.34\pm0.04\pm0.03)\%$ for $B\to\psi'$X, and $(0.40\pm0.06\pm0.04)\%$ for $B\to\chi_{c1}$X. We also find some indication of the inclusive production of χ_{c2}. Momentum spectra for inclusive J/ψ and ψ' production are presented. These measurements are compared to theoretical calculations and are used to probe for evidence of color suppression.

We find exclusive branching fractions or upper limits for B-meson decay to specific final states with only a J/ψ, ψ' or χ_{c1} and a K^-, K^0, K^{*-} or K^{*0}. Of special note, we find branching fractions of $(0.104\pm0.010\pm0.006)\%$ for $B\to J/\psi K^-$, $(0.092\pm0.018\pm0.008)\%$ for $B\to J/\psi K^0$, and $(0.087\pm0.025\pm0.009)\%$ for $B\to\chi_{c1}K^-$. The value of $|a_2|$ in the Wirbel, Stech and Bauer model, as updated by Neubert *et al.*, for two body decays of B mesons is found to be $0.24\pm0.01\pm0.01$.

The branching fractions presented here are significant improvements over current world averages. In addition to providing interesting tests of strong-interaction phenomena, they are also important engineering numbers for experiments at higher energies, where charmonium production is used as a tag for B-meson decay. Some of the processes studied are CP eigenstates and thus are of interest for future experiments that will search for CP violations in the B-meson sector.

Acknowledgements

A thesis is always a product of more people than the one whose name appears on the author page. This thesis is not only built upon the work of the thousands of scientists who have "gone before," but more directly it is built on the contributions of the several hundred physicists that make up the CLEO-II collaboration and the CESR accelerator staff. Of these many scientists, a few stand out for special mention. First, and foremost, is my advisor Ron Poling, who suggested the thesis topic and who made the first measurement of $B \to \chi_{c1} X$. This thesis also benefitted greatly from Ron's legendary editing skills. Special thanks should also go to my "grand advisor," Ed Thorndike who "supervised" my original research efforts. Yuichi Kubota contributed through many discussions.

Two Cleons of my own generation also deserve special thanks. Jeff Nelson provided an encyclopedic knowledge of the CLEO experiment and could answer just about any question I could ask. He also put up with three years of having me as an office mate. Roy Wang helped out in a variety of ways including the lepton studies and skims. He made not only a wonderful office mate and soccer opponent but also a great house mate (just ask me about the "secret" sauce he uses in his "Chinese" cooking). Other "Minnesotans" whose help over the years is appreciated are Dave Perticone, Dan Riley, Vladimir Savinov, Mark Lattery, and Simon Patton. Cleons of note include but are not limited to Mark Battle, Kevin Sparks, Klaus Honscheid, David Kreinick, Sheldon Stone, and David Besson.

I would like to thank my parents Ann and Lorenz Schrenk for bringing me into this world and kindling my interest in science. My sisters Lisa and Janet, and my grandmother Mrs. Charles T. Sweeney for their support over the years. And finally, I would like to thank Cindy Bates for being such a good friend.

Table of Contents

List of Tables

List of Figures

"Happy Day"

– Dalai Lama

Chapter 1

INTRODUCTION

Our search for the building blocks of nature has taken us from Anaximenes' water, air, earth and fire model through Mendeleev's periodic table to the current Standard Model. As in the first two models, the Standard Model seeks to build all of nature from a few fundamental objects. In the Standard Model two sets of particles, leptons and quarks, provide the building blocks while a third set provides the glue. In an atom, electrons (a type of lepton) circle a nucleus composed of protons and neutrons (nucleons) which in turn are composed of quarks. The electrons are bound to the nucleus by the electromagnetic force through the exchange of "virtual" photons, while the nucleons and the quarks within are bound by the "strong" force mediated by "gluons." Another force is responsible for nuclear decay (the "weak" force) and a final force, not considered part of the Standard Model, is responsible for gravity.

The Standard Model can be divided into two parts, Quantum Electrodynamics (QED), the theory of the electromagnetic and weak forces, and Quantum Chromodynamics (QCD), the theory of the strong force. QED has been wildly successful: in some cases theory and experiment agree to less than a millionth of one percent. QCD, although inspired by QED in many ways, has an additional complication that makes calculations much more difficult, forcing us to rely on empirical models. This thesis

describes measurements of the decay of B mesons to charmonium mesons. (Mesons are the bound state of a quark with an antiquark.) The measurements can be used to check the validity of the various models and provide guidance for future theoretical work.

An additional motivation for this work is that other experiments, both current and proposed, rely on knowing the "branching ratios"[1] and other parameters for various B-meson decays. This thesis presents the first measurements of several of these branching ratios, and significant improvements of many that have been measured before.

Before one can delve into the intricacies of this research it is necessary to have a foundation in the theory and experimental techniques of this field. Chapter 1 contains an overview of the Standard Model with an emphasis on the necessary background to understand this thesis. Chapter 2 covers hardware: the accelerator and detector. Chapter 3 explains the software: event reconstruction and simulation. Chapter 4 presents the experimental technique and Chapter 5 the conclusions.

1.1 LEPTONS

The electron (e^-) is the most familiar lepton. There are also two "heavy" electrons, the muon (μ^-) and the tau (τ^-), both with the same magnitude electrical charge as the electron. The muon and tau are unstable and quickly decay. Leptons have an intrinsic spin of 1/2 and thus belong to the fermion class of particles. Each of these leptons forms a family with a neutral partner, the electron, muon and tau neutrinos (ν_e, ν_μ, ν_τ). Each lepton also has a corresponding antiparticle with the opposite charge. The antiparticle of the electron is the positron. The symbol for an antiparticle is the same as for the matching particle, but with either a change of sign or a bar on top.

Each lepton has a lepton "quantum" number assigned to it depending on the family it belongs to. The electron and electron neutrino have a value $\mathrm{L}_e = 1$ while the matching

[1]The probability a particle decays via a given mode is known as the branching ratio or fraction for that mode.

Name	Symbol	Charge Q/|e|	Mass MeV/c^2
Electron	e^-	-1	0.511
Electron Neutrino	ν_e	0	0(?)
Muon	μ^-	-1	105.7
Muon Neutrino	ν_μ	0	< 0.27
Tau	τ^-	-1	1784
Tau Neutrino	ν_τ	0	< 35

Table 1.1: Leptons[1].

antiparticles have a value $L_e = -1$. Particles in the muon family have a value $L_\mu = 1$, while those in the tau family have a value of $L_\tau = 1$. The values of L_e, L_μ and L_τ are zero for leptons of the other families. Lepton numbers are additive and are conserved in all interactions (i.e. the sums before and after an interaction are the same). For example, when a muon decays to an electron, both a muon neutrino and an electron antineutrino must also be emitted so that the total of L_μ is 1 and L_e is 0 both before and after.

1.2 QUARKS

Quarks are the basic building blocks of two types of subatomic particles, mesons and baryons, collectively called hadrons. Quarks come in six "flavors" labeled, u, d, s, c, b and t. Particles composed of the first five have been seen, while evidence for the sixth (t) is indirect. Like the leptons, the quarks are fermions, and are paired in three doublets. One partner in each doublet has a charge of $+2/3$ and the other $-1/3$ (see Table 1.2). The lowest mass pair, u and d, make up normal matter (neutrons and protons). Each quark has a matching antiquark with the same mass, but with opposite charge. Quarks are also assigned "internal" flavor quantum numbers: the s, c, b and t quarks have flavor quantum numbers of S $= -1$, C $= 1$, B $= -1$ and T $= 1$, respectively. The negative values for S and B are a historical accident. The matching antiquarks have

Name	Symbol	Charge Q/|e|	Mass MeV/c^2
Down	d	$-1/3$	10
Up	u	$+2/3$	10
Strange	s	$-1/3$	200
Charm	c	$+2/3$	1500
Bottom (Beauty)	b	$-1/3$	5000
Top (Truth)	t	$+2/3$	150000

Table 1.2: Quarks are classed into three families. Masses are approximate[1]. Charge is the fraction of the absolute value of the electron charge.

flavor values of opposite sign. Flavor quantum numbers are conserved by all but the "weak" interactions, as is discussed later. In other words, if a particle with S $= -1$ is created, then it must be accompanied by the creation of a particle with S $= 1$.

Each quark has a property or "charge" called color. The color charge should not be confused with the color that an eye can see. Instead it serves as an analogy for how the property is used in quantum mechanics, much in the same way that negative and positive are used to describe the electric charge. The three color "charges" are red (r), blue (b) and green (g). Antiparticles have anti-red ($\overline{r}$), anti-blue ($\overline{b}$), or anti-green ($\overline{g}$) color charges. Like flavor, color is a conserved quantity. From experimental observation we never see the bare color charges, and thus never see single quarks. The particles we detect are color neutral (just as when one mixes the three primary colors to make white we do not see any of the three colors).

There are two ways in which quarks are observed to combine into color-neutral particles. The first is to match a quark of one color with an antiquark that has the matching anti-color. Particles made up of quark-antiquark pairs are called mesons. The actual pairing must be in a color singlet state. This means that if one were to substitute one color for another the state must be unchanged. Thus the quark-antiquark pair is actually a mixed state containing equal amounts of $r\overline{r}$, $b\overline{b}$ and $g\overline{g}$.[2] Table 1.3 lists some

[2]Suppose you where to swap r and $\overline{r}$ for b and $\overline{b}$ then the state $(r\overline{r} + b\overline{b} + g\overline{g})$ becomes $(b\overline{b} + r\overline{r} + g\overline{g})$

of the known mesons. The quarks are held together by gluons, discussed below.

The quarks in mesons are bound together in a similar way to the binding between the electron and proton in the hydrogen atom. The quark-antiquark pair can be in an excited state. This leads to different mesons with the same quark pairings but different masses. Excitations can come about in two ways. First, in analogy to the excited states of electrons in atoms, there can be orbital excitations. Examples of this are the 1S, 2S, 3S and 4S states of the $c\overline{c}$ or $b\overline{b}$ systems, which are the families of the ψ and Υ resonances. Second, the spins of the two quarks can be either parallel or anti-parallel. This is the difference between the K and K* mesons.

In Table 1.3 one will notice that the π^0 meson is described by $\sqrt{1/2}(u\overline{u} - d\overline{d})$. When two quark-antiquark pairs have the same charges, and masses that are not too far apart, the actual physical states (those we see in the laboratory) can be mixtures of those pairs. The quark pairs $u\overline{u}$, $d\overline{d}$ and $s\overline{s}$ have the same net charge (zero) and masses that are close enough for mixing. The amount of each pair in the π^0, η and η' has been experimentally determined. The meson states K^0 ($d\overline{s}$) and $\overline{\mathrm{K}^0}$ ($\overline{d}s$) also mix to form the K^0_S and K^0_L mesons in a similar way.

The second way of combining quarks in a color neutral way is to combine three quarks with r, b and g (or with $\overline{r}$, $\overline{b}$ and $\overline{g}$) colors, since $r+b+g$=white. Particles made up this way are called baryons. Conservation of color at the quark level implies that baryons must be produced in matter, antimatter pairs. Nucleons (the building blocks of the atom's nucleus; e.g. protons and neutrons) are baryons. Table 1.4 lists some typical baryons.

---

which is just the original state rewritten.

Meson	Quarks	Mass (MeV/c^2)	J$^{P(C)}$
π^+	$u\overline{d}$	139.6	0^-
π^0	$\sqrt{\frac{1}{2}}(u\overline{u}-d\overline{d})$	135.0	0^{-+}
η	$\sqrt{\frac{1}{6}}(u\overline{u}+d\overline{d}-2s\overline{s})$	547.5	0^{-+}
η'	$\sqrt{\frac{1}{3}}(u\overline{u}+d\overline{d}+s\overline{s})$	957.8	0^{-+}
K^+	$u\overline{s}$	493.7	0^-
K^0	$d\overline{s}$	497.7	0^-
K^{*+}	$u\overline{s}$	891.6	1^-
K^{*0}	$u\overline{s}$	896.1	1^-
D^+	$c\overline{d}$	1869.3	0^-
D^0	$c\overline{u}$	1864.5	0^-
$\eta_c(1S)$	$c\overline{c}$	2979	0^{-+}
$J/\psi(1S)$	$c\overline{c}$	3096.9	1^{--}
$h_c(1P)$	$c\overline{c}$	3525[2]	1^{+-}
$\chi_{c0}(1P)$	$c\overline{c}$	3415	0^{++}
$\chi_{c1}(1P)$	$c\overline{c}$	3510.5	1^{++}
$\chi_{c2}(1P)$	$c\overline{c}$	3556.2	2^{++}
$\psi'(2S)$	$c\overline{c}$	3686.0	1^{--}
B^+	$u\overline{b}$	5279	0^-
B^0	$d\overline{b}$	5279	0^-
$\Upsilon(1S)$	$b\overline{b}$	9460	1^{--}
$\Upsilon(2S)$	$b\overline{b}$	10023	1^{--}
$\Upsilon(3S)$	$b\overline{b}$	10355	1^{--}
$\Upsilon(4S)$	$b\overline{b}$	10580	1^{--}

Table 1.3: Mesons that appear in this thesis[1]. Mesons have partners made by exchanging each quark with its antiquark, i.e. π^- is the partner of π^+ and is made up of $\overline{u}d$. Some particles, such as the π^0, are their own partner. J is the total angular momentum, P the parity and C the charge conjugation of the state.

Baryon	Quarks	Mass (MeV/c^2)	J^P
p	uud	938.3	$\frac{1}{2}^+$
n	udd	939.6	$\frac{1}{2}^+$
Λ	uds	1115.6	$\frac{1}{2}^+$
Λ_c^+	udc	2285	$\frac{1}{2}^+$

Table 1.4: Baryons[1]. Baryons have partners made by exchanging each quark with its antiquark, i.e. $\overline{\text{p}}$ is the partner of p and is made up of $\overline{uud}$. J is the total angular momentum and P is the parity.

1.3 QUANTUM NUMBERS

Lepton numbers and flavor are only a few of the quantum numbers which serve to distinguish the many different leptons, mesons and baryons. In the last column of Table 1.3 and Table 1.4, J is the total angular momentum, P is the parity, and C is the charge conjugation of the meson or baryon. Angular momentum of all particles before an interaction must equal the total after an interaction. This requirement dictates the angular distribution of decay products. P and C are multiplicative quantum numbers, e.g. the C or P number of a group of particles is the product of all particles' C or P numbers. The C number only is defined for neutral particles. P and C are conserved in electromagnetic and strong interactions but not always in weak interactions. These quantities are further discussed in Appendix A.

1.4 FORCES

Four types of fundamental forces exist in nature. They are the gravitational, electromagnetic, weak and strong forces. Each force is mediated by one or more "gauge" particles. The gauge particles are emitted or absorbed by the different "charges." These interactions can be attractive or repulsive, and they can lead to the annihilation or creation of particles.

We are most familiar with gravity, the weakest of the forces. The gauge particle responsible for gravity has not yet been discovered. The theory of gravity is still in its infancy and it is not considered to be part of the Standard Model. Gravity plays a role only on a macroscopic scale and as such will not be mentioned again in this thesis.

The next two forces are linked together in the theory of Quantum Electrodynamics (QED). The first of these is the electromagnetic force. It is mediated by the familiar photon or quantum of light. The second of these forces, the weak force, is responsible for nuclear decay. It is mediated by the three massive particles, the Z^0, W^+ and W^-.

Name	Symbol	Electrical Charge Q/|e|	Mass GeV/c^2
Photon	γ	0	0
W Minus	W^-	-1	80.2
W Plus	W^+	1	80.2
Z Zero	Z^0	0	91.2
Gluon	g	0	0

Table 1.5: Gauge Bosons[1].

These gauge particles are collectively known by the intimidating name "intermediate vector bosons." The masses limit the range of the weak force.

The final force, named the strong force, binds quarks in hadrons as well as nucleons in atomic nuclei. Eight gluons mediate the strong force, interacting with the color charges of the quarks. This part of the Standard Model is called Quantum Chromodynamics or QCD.

1.5 FEYNMAN DIAGRAMS

The great physicist Richard Feynman invented an easy way to diagram particle interactions. The basic interaction is shown in the Feynman diagram in Fig 1.1a. Here particle A emits a gauge particle C. In most, but not all, cases particle B is the same as particle A. In Fig 1.1b, the diagram is rotated. This is still the same fundamental interaction but here we interpret it as a gauge particle decaying into a particle-antiparticle pair. Note that the arrow for particle B is pointed backward, this represents an antiparticle moving forward in time. Fig 1.1c represents the absorption of a gauge particle and Fig 1.1d represents the creation of a gauge particle by annihilation of a particle and antiparticle.

Attractive or repulsive forces result when two particles, each with the same type of "charge" exchange gauge particles (see Fig. 1.2a). The charges both create and absorb the gauge particles. Since the creation of the gauge particle violates energy and

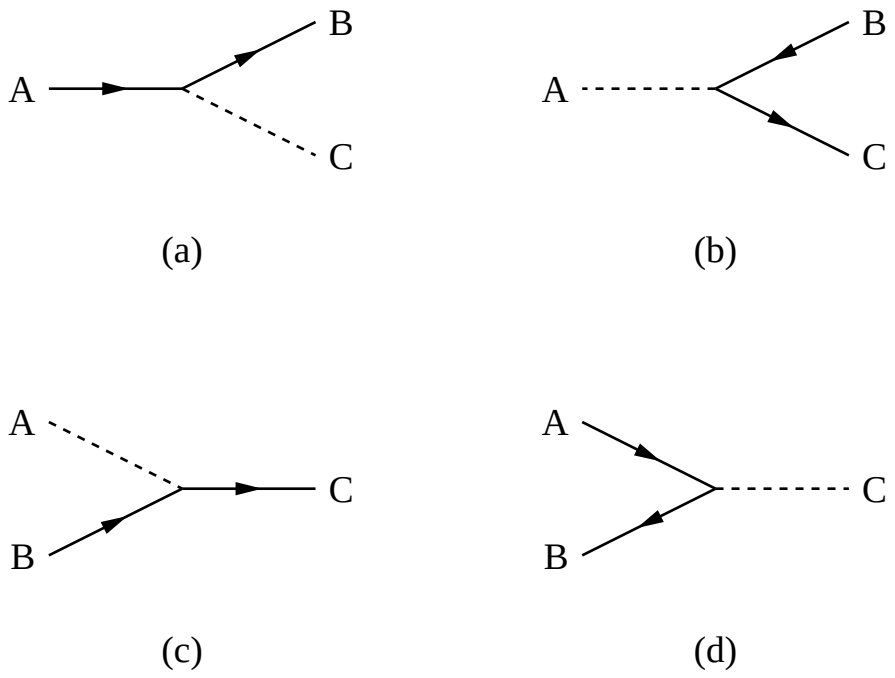

Figure 1.1: The basic interactions: (a) Emission of a gauge particle, (b) Creation of a particle and antiparticle by decay of a gauge particle, (c) Absorption of a gauge particle, (d) Creation of a gauge particle by annihilation of a particle and antiparticle.

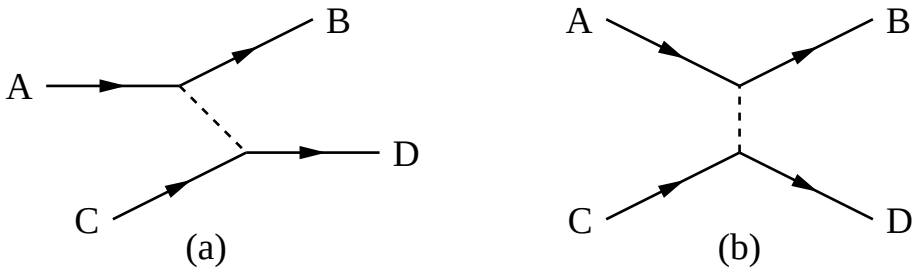

Figure 1.2: The exchange interaction.

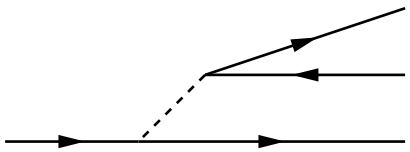

Figure 1.3: Particle decay diagram.

momentum conservation, the gauge particle is said to be virtual. Virtual particles are allowed by the Uncertainty Principle, but they can only exist for a very short time. This has the effect of limiting the range of a force when the gauge particle is massive. Overall energy and momentum conservation between the initial and final particles is required. In practice, we can not tell which particle emitted the gauge particle and which one absorbed it. Thus we use the diagram in Fig. 1.2b rather than in Fig. 1.2a.

Heavy leptons and quarks can decay into lighter particles by emitting a "weak" force gauge particle (see Fig. 1.3). The gauge particle then decays into a particle-antiparticle pair. This is discussed further in the Weak force section below.

1.6 MATRIX ELEMENTS

From a Feynman diagram it is relatively easy to write down the equations that describe an interaction. The likelihood that two particles interact or the likelihood that a particle decays is proportional to the square of the "matrix element" $\mathcal{M}$. Using the "bra" and "ket" notation developed by Dirac we have

$$\mathcal{M} = \langle \mathrm{f}|\mathrm{H}|\mathrm{i}\rangle \,. \tag{1.1}$$

The f and i represent the final-state and the initial-state wave functions respectively. The wave function is the complete description of the particles prior to or after the

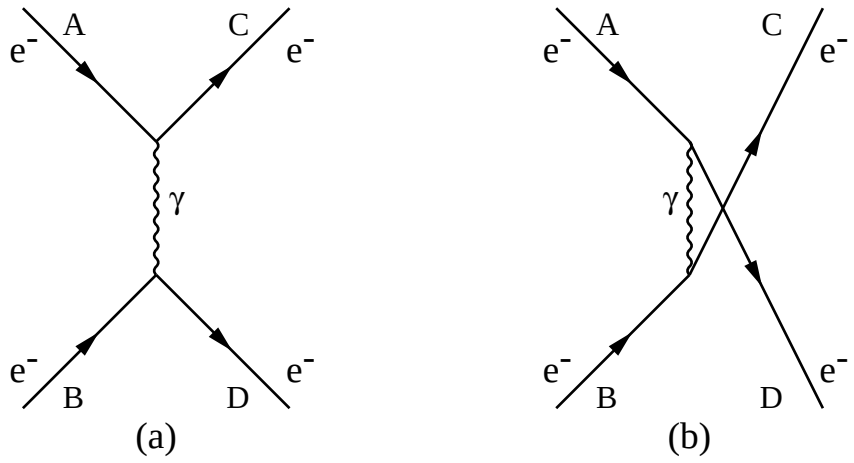

Figure 1.4: Interaction between two electrons, known as Møller scattering.

interaction, including, for example, their momentum, energy, and spin. H is the symbol for the "Hamiltonian" which describes the interaction. Essentially one integrates over the initial and final state wave functions with the Hamiltonian sandwiched in between. The Hamiltonian contains a factor for each vertex and "propagator" in the Feynman diagram. A propagator corresponds to any particle that is both created and destroyed in the interaction, like the gauge bosons in Fig. 1.2. The factor at each vertex is proportional to the square root of the "coupling constant." The coupling constant is just the charge (electrical or color) expressed in dimensionless units. If there are more than one Feynman diagram that can link the initial and final states then H is the sum of all such diagrams.

1.7 QED

1.7.1 Electromagnetic Interactions

In Fig. 1.4a. is an example of a Feynman diagram where one electron interacts with another electron via the exchange of a photon. The exchange results in a repulsive

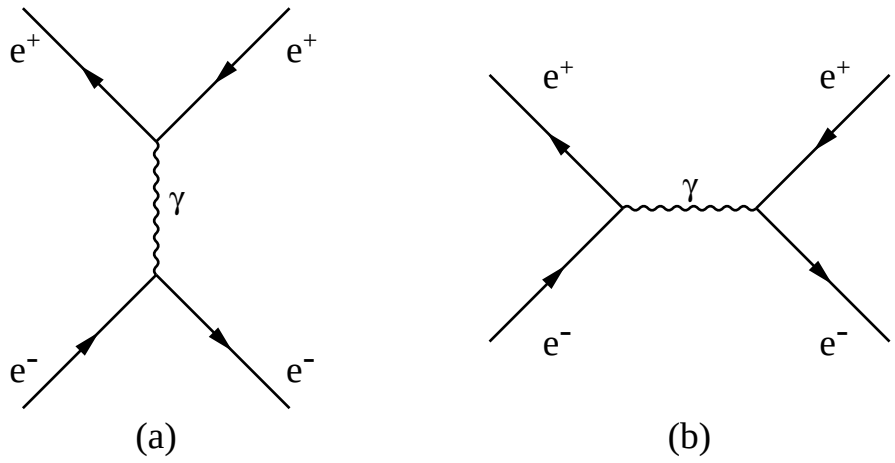

Figure 1.5: Bhabha scattering.

force between the two electrons. The electrons are said to have scattered off each other. We can not distinguish if electron C is the same as electron A or electron B. Thus the second diagram (Fig 1.4b) is also possible and the interaction Hamiltonian must include terms representing both diagrams.

We can go one step further by scattering an electron off a positron. This is shown in Fig. 1.5a. A second Feynman diagram is again possible. In Fig. 1.5b the electron first annihilates the positron, producing a virtual photon, which subsequently materializes as a new electron-positron pair. Viewed in the center of mass rest frame of the electron and positron, the photon can have no momentum. This violates the relativistic requirement that massless particles must move at the speed of light and dictates that the photon is virtual and must decay. While the two diagrams of Fig. 1.5 are distinct, with very different angular distributions, they cannot be distinguished on an event-by-event basis experimentally. Note that Fig. 1.5b is just Fig. 1.4a rotated by 90° with B and D flipped.

The virtual photon in Fig. 1.5b can decay to other particle-antiparticle pairs, with the constraint that the final state conserves the energy of the initial electron and positron.

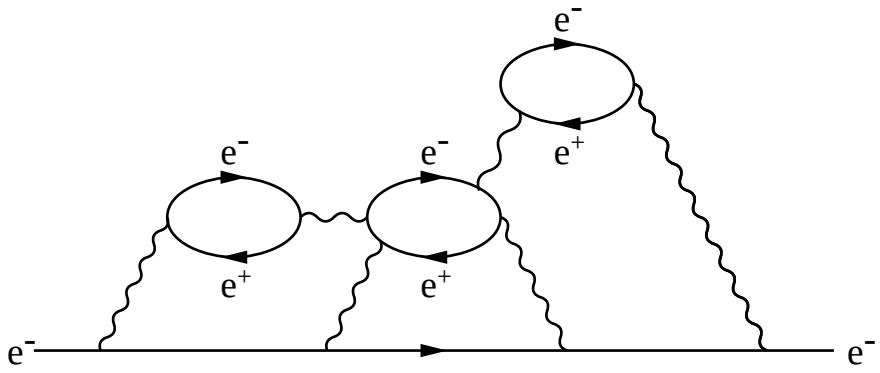

Figure 1.6: The virtual cloud around a real electron.

This allows experimentalists to create a variety of different particles in the laboratory, including the B mesons studied in this thesis. The Z^0 can also mediate the exchange. The probability that this happens is great when the energy of the system is near the mass of the Z^0 (thus the Z^0 is almost real). At the energies used in this thesis, the Z^0 plays a negligible role.

Virtual particles play a role in "screening" the actual electrical charge of a particle. Consider the electron in Fig. 1.6. The electron as it moves through time continually emits and absorbs virtual photons. These virtual photons in turn can produce virtual electron-positron pairs. The positron in the pair moves towards the real electron while the virtual electron moves away. This effectively screens the real electron's charge. The electric charge we measure at a distance is less than that we measure when we use a high energy particle to probe within the virtual cloud surrounding the electron. Thus the effective value of the electric charge we measure is larger in higher energy electron-positron collisions. The electric charge or coupling constant α measured outside the virtual cloud of the electron is 1/137.

The diagrams in Fig. 1.5 are not the only possible ones. Some additional possible

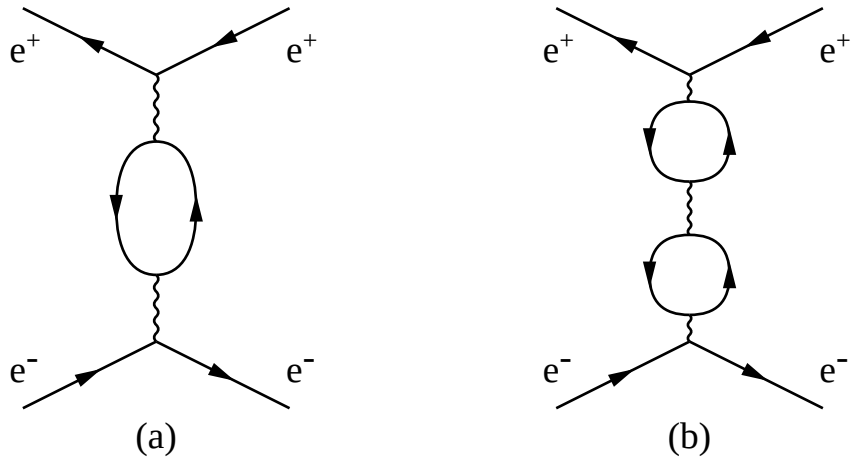

Figure 1.7: Additional contributions to bhabha scattering.

diagrams are depicted in Fig. 1.7. The strength of the interaction between the electron and positron is proportional to the square of the sum of the amplitudes for ALL possible diagrams. The effect of additional diagrams is small, however, as each additional vertex suppresses the contribution of that diagram by a factor of $\sqrt{\alpha}$, i.e. the diagram in Fig. 1.7a contributes roughly 1/137 of that of either of the two diagrams in Fig. 1.5.

1.7.2 Weak Interactions

The weak force mediates interactions within lepton or quark families. The emission or absorption of a W^+ or W^- changes one member of a family to another, e.g. $e^- \rightarrow \nu_e$ or $c \rightarrow s$. The decay of a W produces a lepton or quark with its partner's antiparticle, e.g. $W^- \rightarrow e^- \overline{\nu}_e$ or $W^- \rightarrow s\overline{c}$. Fig. 1.8 shows a typical "weak" decay. The emission and absorption of the W is referred to as a "charged current" since the W carries a charge from one vertex to another.

For quarks, the mass "eigenstates" that are produced are not quite the same as those "seen" by the weak interaction. For example the "b" which participates in the weak interaction is a mixture of mostly the b-mass state, with a bit of s and d. If this

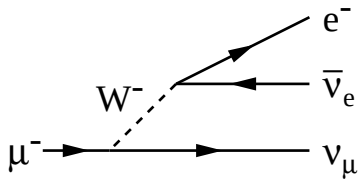

Figure 1.8: Example of weak decay: decay of $\mu^- \rightarrow e^- \overline{\nu}_e \nu_\mu$.

were not the case, the b would not decay, since its partner, the t, is more massive. The probability that the b mass state will decay into a c or u is proportional to the square of the amount of this mixture. In practice, one is free to choose either the set of $+2/3$ charged quarks (u, c, t) or the set of $-1/3$ charge quarks (d, s, b) to be mixed, with the other set unmixed. By convention the latter set is chosen to be mixed. The amount of mixing can be parameterized by the 3×3 Cabbibo-Kobayashi-Maskawa (CKM) matrix:

$$\begin{pmatrix} d' \\ s' \\ b' \end{pmatrix} = \begin{pmatrix} \mathrm{V}_{ud} & \mathrm{V}_{us} & \mathrm{V}_{ub} \\ \mathrm{V}_{cd} & \mathrm{V}_{cs} & \mathrm{V}_{cb} \\ \mathrm{V}_{td} & \mathrm{V}_{ts} & \mathrm{V}_{tb} \end{pmatrix} \begin{pmatrix} d \\ s \\ b \end{pmatrix}.$$

The approximate value of the matrix is[1]

$$\begin{pmatrix} 0.975 & 0.22 & 0.003 \\ 0.22 & 0.97 & 0.04 \\ 0.01 & 0.04 & 0.999 \end{pmatrix}.$$

Note that the diagonal elements are nearly one. Decays between families are suppressed, and are rarely observed unless there is no other decay channel open, as in the case of the b. Since V_{cb} is much larger than V_{ub}, the b quark prefers to decay to a c quark rather than a u quark. Some of the terms may be complex.

The Z^0 also interacts with the "weak" charge, but it does not change flavors and thus it acts like a heavy photon.

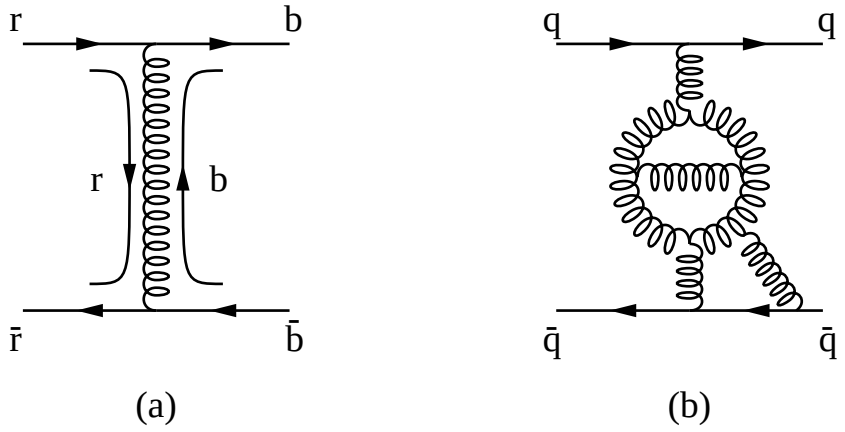

Figure 1.9: Gluon exchange: (a) The r ("red") quark becomes a b ("blue") quark by emitting a gluon with color charge $r\overline{b}$, or equivalently, the r quark becomes a b quark by absorbing a gluon with color charge $b\overline{r}$. (b) A possible diagram where some of the gluons serve as sinks and sources of other gluons.

1.8 QCD

Quantum chromodynamics (QCD) describes the force mediated by gluons. Quarks are bound together by the exchange of gluons. The gluons interact with the color charges of the quarks, thus the "chromo" in quantum chromodynamics. Gluons carry a color and an anticolor charge. Fig. 1.9a show a quark-antiquark pair exchanging a gluon. The gluon carries the charge $r\overline{b}$ or $\overline{r}b$, depending on which particle emitted it. There are nine possible color-anticolor pairs:

$$r\overline{b},\ r\overline{g},\ b\overline{r},\ b\overline{g},\ g\overline{r},\ g\overline{b},\ \frac{1}{\sqrt{2}}(r\overline{r}-b\overline{b}),\ \frac{1}{\sqrt{6}}(r\overline{r}+b\overline{b}-2g\overline{g}),\ \frac{1}{\sqrt{3}}(r\overline{r}+b\overline{b}+g\overline{g}). \qquad (1.2)$$

The last is a color singlet and can not transfer color between different states, thus there are only eight gluons.

QCD shares many features of QED, but there is an important difference. Since gluons carry color charge they can serve as sources or sinks of additional gluons (Fig. 1.9b). This has an important implication. In the case of the electromagnetic force, the virtual

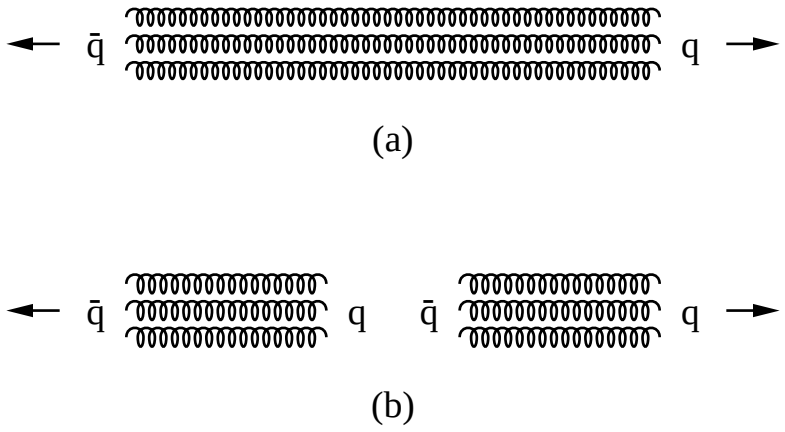

Figure 1.10: Quark popping.

cloud around the electron masks the true electron charge. In the case of color, the effect is just the opposite. The farther one goes away from a color charge, the stronger the effective charge. Thus as two quarks in a meson are pulled apart (as they might be in a high energy collision), the force grows stronger and stronger until there is enough potential energy to "pop" a new quark-antiquark pair out of the vacuum (see Fig. 1.10). Each part of the new pair joins one part of the old pair to form two new mesons. If the quarks in the new pairs do not have momenta that match well, the process can repeat itself. The process through which bare quarks combine into hadrons by popping quark-antiquark pairs is termed fragmentation or hadronization. The fragmentation process often preserves the directions of the original quarks, giving rise to "jets" of hadrons in high energy events.

The corollary to the above is that two quarks close together act as if they are free. This is called "asymptotic freedom." In processes that probe close to the quark the strong coupling constant α_s is small, and the standard techniques of QED work in describing the quarks' state. But when the quarks are pulled apart, α_s becomes large and it becomes difficult to make calculations. We call α_s a "running" coupling constant

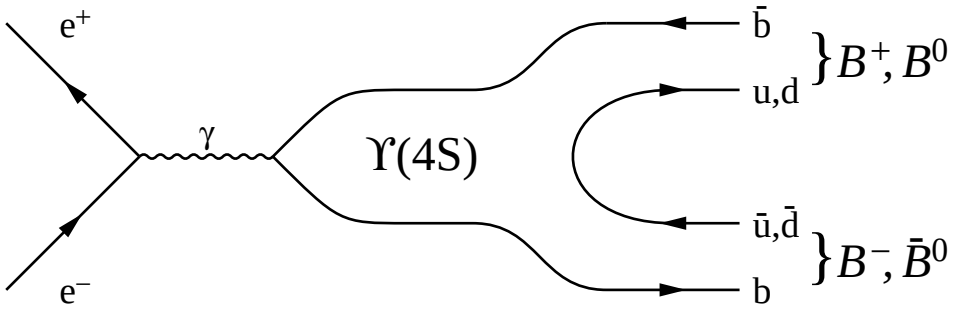

Figure 1.11: Production of B mesons in e^+e^- collisions.

because its value depends upon the energy scale of the interactions.

1.9 FORMATION OF B MESONS

This thesis is about the decay of B mesons to charmonium states. In order to create the B mesons we collide high-energy electrons and positrons in the middle of a large detector (see Chapter 2). An electron and positron that collide and annihilate produce a virtual photon which then decays into a particle-antiparticle pair. These two particles can bind together to make a meson. If the total energy of the electron and positron is about the mass of a meson with the same quantum numbers of the virtual photon, there can be an enhancement in the cross section for interaction. This is called a resonance. For our experiment the e^+e^- center of mass energy is chosen to be that of the Υ(4S) resonance. The Υ(4S) mass is just larger than the sum of the mass of a B meson ($\overline{b}u$ or $\overline{b}d$) and its antiparticle $\overline{B}$ meson ($b\overline{u}$ or $b\overline{d}$) (see Fig. 1.11). While the experimental evidence is not conclusive, the Υ(4S) resonance is believed to decay to $B\overline{B}$ 100% of the time.

1.10 CHARMONIUM

Charmonium is the bound state of the c and $\overline{c}$ quarks. In many ways the $c\overline{c}$ system mirrors that of an atom, with the same types of excitations. There are two important differences. The first is that in the hydrogen atom, the mass of the electron is much smaller than that of the nucleus (roughly a factor of 2000) and one can think of the electron interacting with a fixed nucleus. In contrast, in a charmonium meson the masses of the quark and antiquark are the same, and the interaction of the particles must be described relative to their center of mass.

The second major difference is that the atom is bound by the electromagnetic force, while the quarks are bound by the strong force. The effect of virtual particles surrounding an electric charge can conveniently be accounted for by adjusting the magnitude of the charge. The forces between two electric charges sufficiently far apart is then just inversely proportional to the distance between the charges. Knowing the force allows one to calculate very accurately the energy levels of simple atoms. On the other hand, the farther one moves away from a color charge, the more important the virtual gluons become, and the more difficult it is to predict the binding force. Thus calculating the energy levels in charmonium is much more difficult than calculating the energy levels in the hydrogen atom.

The mass spectrum of known charmonium states below threshold for $D\overline{D}$ production is illustrated in Fig 1.12. The $\eta_c(1S)$ is the ground state of the $c\overline{c}$ system. The spins of the two quarks are antiparallel (J = 0, see Appendix A). The J/ψ meson[3] and the ψ' are the 1S and 2S orbital excitations of charmonium, where the spins are parallel (J = 1). The χ_c states are the 2P orbital excitations, with the quark spins parallel. The physical evidence for h_c, the 1P state with the spins antiparallel, and the η_c', the 2S state with spins antiparallel, is weak. Other states are possible, but the energy of

[3]The J/ψ was discovered at the same time by groups at Brookhaven and SLAC. The Brookhaven group named it the J and the SLAC group named it the ψ.

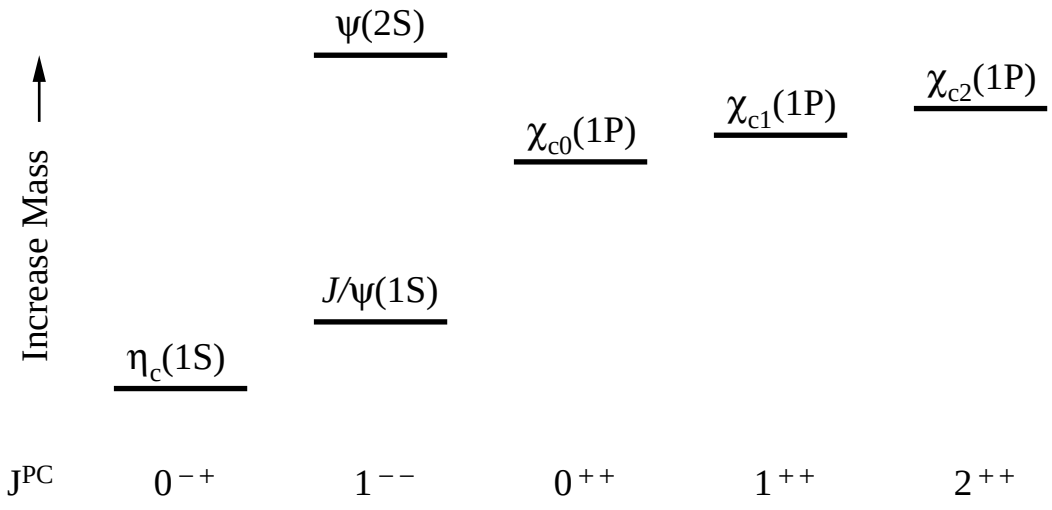

Figure 1.12: The various known charmonium states below the threshold for $D\overline{D}$ production.

those states would be above the threshold needed for producing $D\overline{D}$ pairs ($c\overline{u}$ and $\overline{c}u$, or $c\overline{d}$ and $\overline{c}d$). The states above the threshold are very short-lived.

Conservation laws dictate that only certain transitions are allowed between the various charmonium states. Except for $\psi' \rightarrow J/\psi$ decays all observed charmonium to charmonium transitions occur by emission of a photon. The photon has an odd charge conjugation number ($C = -1$), and thus can only link states with opposite charge conjugation. The ψ' decays to J/ψ by emitting either two pions ($\pi^+\pi^-$ or $\pi^0\pi^0$), a single π^0, or an η.

All states below the threshold for $D\overline{D}$ production decay to non-charmonium states through the annihilation of the c and $\overline{c}$. Depending on the quantum numbers of the charmonium state, either two or three gluons or photons are emitted. The $J^{PC} = 1^{--}$ states can also decay through a virtual photon (see Fig. 1.13). This decay is important, as it has a unique experimental signature, a high energy lepton-antilepton pair.

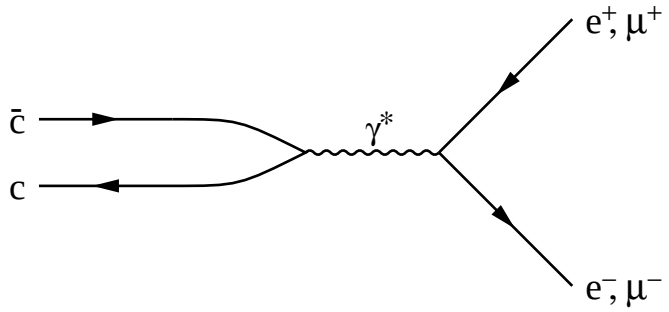

Figure 1.13: Charmonium decay through a virtual photon to a e^+e^- or $\mu^+\mu^-$.

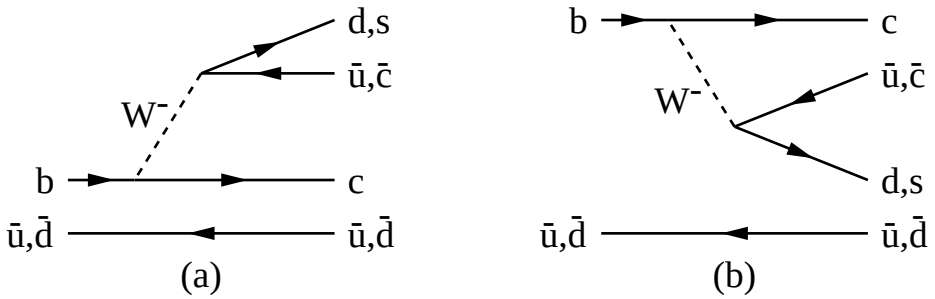

Figure 1.14: Spectator decay Feynman diagram.

1.11 *B*-MESON DECAYS

1.11.1 Spectator Decays

Most decays of B mesons can be described by the spectator diagrams in Fig 1.14. The name spectator comes from the feature that the quark bound to the b plays no role in the decay process. The basic interaction Hamiltonian is

$$\mathrm{H}_{Weak} = \frac{G_F}{\sqrt{2}} \mathrm{V}_{cb} \left[\mathrm{V}^*_{ud} (\overline{d}u) + \mathrm{V}^*_{cs} (\overline{s}c) \right] (\overline{c}b), \tag{1.3}$$

where V_{cb}, V_{ud}, and V_{cs} are the CKM matrix elements. The terms $(\overline{d}u)$, $(\overline{s}c)$, and $(\overline{c}b)$ represent the interactions at each vertex. Here $\overline{d}$ represents the creation of a

d or the annihilation of a $\overline{d}$ quark. The term $(\overline{d}u)$ also includes restrictions on the possible quantum numbers of the two particles. The term G_F is the Fermi constant which includes the coupling constant factor from the two vertices, and the effect of the massive W propagator (to within a factor of 2, $G_F \approx \alpha/\mathrm{M}_\mathrm{W}^2$). Since we are only interested in charmonium states we will drop the $(\overline{d}u)$ term:

$$\mathrm{H}_{Weak} = \frac{G_F}{\sqrt{2}} \mathrm{V}_{cb}\mathrm{V}_{cs}^*(\overline{s}c)(\overline{c}b). \tag{1.4}$$

Note that everything that is described here also applies if every particle is replaced by its corresponding antiparticle (and every antiparticle is replaced by its matching particle).

For the decay of B mesons to charmonium states, the $\overline{c}$ from the W must combine with the c from the b (see Fig. 1.14b). This is called an internal spectator diagram. The c-quark color must match the $\overline{c}$-quark color to form a color neutral meson state. For the external spectator diagram (Fig. 1.14a) the color requirement is automatically satisfied, since the W does not carry color charge and the c preserves the color of the b. For the external spectator diagram there are nine color pairs possible when the W decays, three of which have matching color. Thus there is a one-in-three chance that the color of the c matches that of the $\overline{c}$. One would therefore naively expect that the matrix element for the internal spectator decay would be one third of that for the external diagram. Thus the decay rate for the B meson to a charmonium state would be one ninth of that expected without accounting for color[3].

While the spectator mechanism provides a simple model of B-meson decay, it is not the whole picture. Virtual gluon interactions can take place between the quarks, leading to an "effective neutral current." The transformation of a b into an s is not allowed by the Standard Model. However, virtual gluons can "rearrange" the final state quarks, swapping the c created when the b decays with the s created from the W^- decay (see Fig. 1.15b). The gluon interactions lead to an additional term in the interaction

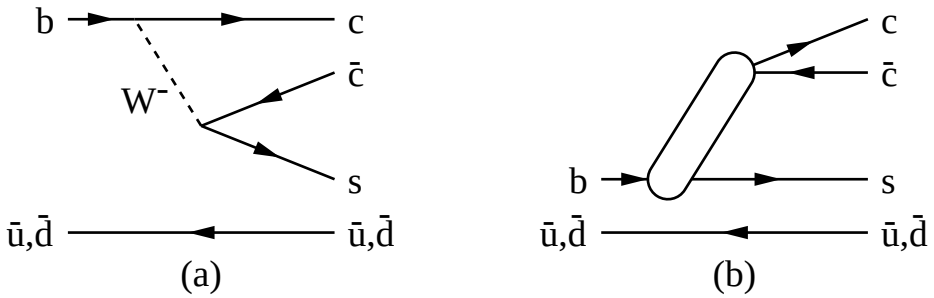

Figure 1.15: The two diagrams leading to charmonium production in B decay; (a) is the internal spectator diagram while (b) is the effective neutral current diagram. The oval represents both the W^- exchange and the gluon interactions.

Hamiltonian with the quark pairings $(\overline{s}b)$ and $(c\overline{c})$:

$$\mathrm{H}_{Effective} = \frac{G_F}{\sqrt{2}} \mathrm{V}_{cb}\mathrm{V}^*_{cs} \left[c_1(\mu)(\overline{s}c)(\overline{c}b) + c_2(\mu)(\overline{c}c)(\overline{s}b) \right]. \tag{1.5}$$

The "Wilson" coefficients $c_1(\mu)$ and $c_2(\mu)$ account for the gluon interactions. They can in principle be calculated from QCD:

$$c_\pm(\mu) = c_1(\mu) \pm c_2(\mu), \tag{1.6}$$

$$c_\pm(\mu) = \left(\frac{\alpha_\mathrm{s}(M_W^2)}{\alpha_\mathrm{s}(\mu)} \right)^{\frac{-6\gamma_\pm}{(33-2n_f)}}, \tag{1.7}$$

where $\gamma_- = -2\gamma_+ = 2$ and n_f is the number of flavors that have a mass near or below the mass of the decaying quark (five for B-meson decay). The term α_s needs to be evaluated at the appropriate energy squared. For the α_s in the denominator it is unclear what value of μ is appropriate. Typically the energy corresponding to the mass of the b is chosen.

To find the total decay rate of B mesons to charmonium one needs to combine the internal spectator diagram with the effective neutral current diagram. Theoretically one can extract the contribution to charmonium from Eq. 1.4 by performing a Fierz-transformation:

$$(\overline{c}_a b_a)(\overline{s}_b c_b) = \frac{1}{3}(\overline{s}_a b_a)(\overline{c}_b c_b) + \frac{1}{2}(\overline{s}\lambda_i b)(\overline{c}\lambda_i c), \tag{1.8}$$

where λ_i are SU(3) color matrices and the subscript explicitly keeps track of the color[4]. The relevant part of the Hamiltonian is then

$$\mathrm{H}_{Effective} = \frac{G_F}{\sqrt{2}} \mathrm{V}_{cb}\mathrm{V}^*_{cs} \left[\left(\frac{1}{3} c_1(\mu) + c_2(\mu) \right) (\overline{c}c)(\overline{s}b) + \frac{1}{2} c_1(\mu)(\overline{s}\lambda_i b)(\overline{c}\lambda_i c) \right]. \qquad (1.9)$$

The first part of equation (1.9) transforms as a color singlet with the $\frac{1}{3}$ reflecting color suppression. The second part transforms as a color octet. Kühn, Nussinov and Rückl argue that the latter term cannot contribute to the formation of charmonium since a meson must be in a color-singlet state[4]. In this case, decay of B mesons to the charmonium states h_c, χ_{c0} and χ_{c2} are forbidden by conservation rules (see Appendix B). They predict the ratio of production in B decay of charmonium to be $0.57 : 1 : 0.27 : 0.31$ for $\eta_c : J/\psi : \chi_{c1} : \psi'$.

Recently, Bodwin, Bratten, Yuan and Lepage have stated that charmonium can also be formed in the decay of a B meson to the $c\overline{c}$ color-octet in an S-wave state[5]. The $c\overline{c}$ color-octet can then radiate a soft gluon to form a color-singlet P-wave state. Bodwin, *et al.* find the ratio of production of $h_c : \chi_{c0} : \chi_{c1} : \chi_{c2}$ to be equal to $1.3 : 0.3 : 1 : 1.3$.

1.11.2 Factorization

The two non-charm quarks in both the internal spectator (charged current) and effective neutral current diagrams form one or more mesons in a process called hadronization. If the momenta of the two quarks are well matched they can form a single meson, but if their momenta are significantly different they will separate and pop quark-antiquark pairs out of the vacuum to form multiple mesons.

When only one meson is formed from the non-charm quarks, it is possible to separate the Hamiltonian into two parts, one part describing the formation of the charmonium state, and the other the formation of a meson from the non-charm quarks. This "factorization" works extremely well in semileptonic decays, where the W decays into a lepton and antineutrino. Leptons have no color, so that they do not interact with the

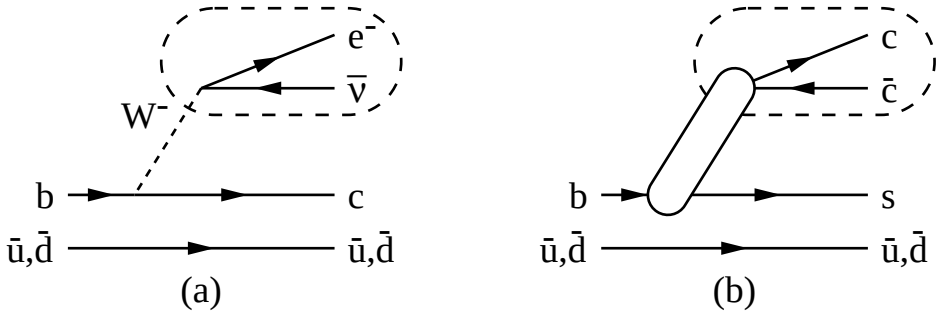

Figure 1.16: Factorization: The two vertices of the current can be considered separately if the particles at one vertex do not interact with the particles at the other. In the semileptonic decay (a) the circled vertex consists of leptons which cannot interact via gluons with the particles at the other vertex. In the hadronic decay to charmonium (b) if the $c\overline{c}$ pair moves away from the interaction region quickly enough then it may be possible to ignore gluon interactions between the pair and the quarks of the other side. It is assumed that the gluon interactions necessary to produce the $c\overline{c}$ pair have already been accounted for.

c or spectator quarks. Fig. 1.16a shows a semileptonic decay. The matrix element for semileptonic decay can be factored as follows:

$$\mathcal{M} = < e^-, \overline{\nu}_e, h|(e\overline{\nu}_e)(\overline{b}c)|\overline{B} >, \tag{1.10}$$

$$= < e^-, \overline{\nu}_e|(e\overline{\nu}_e)|0 >< h|(\overline{b}c)|\overline{B} >, \tag{1.11}$$

where $(e\overline{\nu}_e)$ represents the creation of an electron and an electron antineutrino and $<\ e^-,\ \overline{\nu}_e\ , h\ |$ represents the final state wave functions of the e^-, $\overline{\nu}_e$ and meson. $|\overline{B}>$ is the initial state wave function of the $\overline{B}$ meson. The first part, $< e^-\overline{\nu}_e|(e\overline{\nu}_e)|0 >$, should be the same for all semileptonic decays to electron and electron antineutrino pairs. The second part will vary depending on the final state meson.

We can extend this factorization to diagrams where the W decays to quark-antiquark pairs. The assumption here is that once the quarks from the W are formed they move away from the interaction region quickly enough that gluon interactions with the remaining quarks are negligible. The quark-antiquark pair form a color singlet that is resistant to external color interactions. One is even tempted to apply factorization

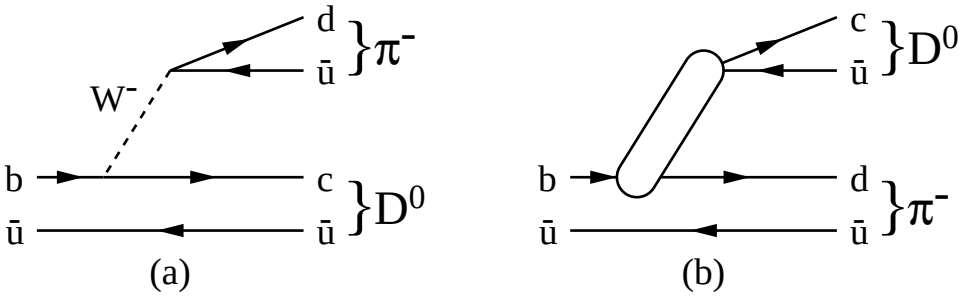

Figure 1.17: Example of decays to identical final states via the a_1 and a_2 terms.

to effective neutral currents (Fig. 1.16b), despite the requirement that there be some gluon interactions.

Bauer, Stech and Wirbel (BSW) modify Equation 1.5 to be

$$H_{eff} = \frac{G_F}{\sqrt{2}} V_{cb} V_{cs}^* \left[a_1 (\overline{s}_b c_b)(\overline{c}_a b_a) + a_2 (\overline{c}_b c_b)(\overline{s}_a b_a) \right], \tag{1.12}$$

where $a_1 \simeq c_1 + \xi c_2$ and $a_2 \simeq c_2 + \xi c_1$, ξ is a color factor which is nominally equal to $1/\mathrm{N}_c$ (N_c is the number of colors, N_c=3 in QCD)[6]. Notice that a_2 is the same coefficient that is before the equivalent term in Equation 1.9 if $\xi = \frac{1}{3}$. The coefficients a_1 and a_2 are determined from experiment.

In this scheme all B-meson decays to two mesons can be divided into three groups. The first group consists of decays where the charged current directly produces a meson. The second group consists of decays where the effective neutral current produces a meson. In the third group are decays in which both the charged and effective neutral currents produce a meson (an example is $B^- \rightarrow \mathrm{D}^0 \pi^-$, see Fig. 1.17). Decays to charmonium states are all in the second group. For this reason measurements of decays to J/ψ provide the best measurement of a_2. The Bauer, Stech and Wirbel model and Equation 1.12 thus provide predictions of relative rates rather than absolute branching ratios. These prediction, as updated by Neubert *et al.* are summarized in Table 1.6[7]. Comparisons of these predicted relative rates with experiment provides an important

Decay	Branching Fraction (%)
$B^- \to J/\psi \mathrm{K}^-$	$1.819 a_2^2$
$B^- \to J/\psi \mathrm{K}^{*-}$	$2.932 a_2^2$
$\overline{B}^0 \to J/\psi \overline{\mathrm{K}^0}$	$1.817 a_2^2$
$\overline{B}^0 \to J/\psi \overline{\mathrm{K}}^{*0}$	$2.927 a_2^2$
$B^- \to \psi' \mathrm{K}^-$	$1.068 a_2^2$
$B^- \to \psi' \mathrm{K}^{*-}$	$1.971 a_2^2$
$\overline{B}^0 \to \psi' \overline{\mathrm{K}^0}$	$1.065 a_2^2$
$\overline{B}^0 \to \psi' \overline{\mathrm{K}}^{*0}$	$1.965 a_2^2$

Table 1.6: The predictions of the BSW model as updated by Neubert *et al.* for the exclusive branching fractions of $B \to J/\psi \mathrm{K}^{(*)}$ and $B \to \psi' \mathrm{K}^{(*)}$ in terms of the constant a_2^2[6, 7].

test of the BSW model.

The goal of this thesis is to test the various QCD calculations of B-meson decays to charmonium. The inclusive decays test color suppression and the color-octet mechanism. A significant branching fraction for $B \to \chi_{c2}$ would support the idea of the color octet mechanism. The exclusive decays contribute to the testing of the usefulness of the idea of factorization in B-meson decays.

The results presented in this thesis are also useful to other experimentalists. The rate for $B \to J/\psi \mathrm{K}^0_{\mathrm{S}}$ is a direct input into the luminosity needed at at B "factory" to measure CP violation in the B system. Previous to this thesis, the value for this branching fraction was known only to 50%[1]. Experiments at higher $\sqrt{s}$ use charmonium as a tag of B decay. Thus they need the branching fractions and momentum distributions as inputs to their calculation of their B-detection efficiency. The branching fraction for $B \to J/\psi \mathrm{X}$ was know only to 14% and for $B \to \psi'$ X only to 43%[1]. The ψ' momentum spectrum has never been measured.

Chapter 2

THE APPARATUS: CESR and CLEO II

2.1 THE CESR ACCELERATOR

We collected the data used in this thesis at the Cornell Electron Storage Ring (CESR) utilizing its companion detector CLEO II.[1] CESR resides in a tunnel 768 meters in circumference under the athletic practice fields at Cornell University in Ithaca, New York. CESR was built from 1977 through 1979 as an addition to an earlier electron accelerator located in the same tunnel. Within the storage ring bunches of electrons circulate counterclockwise (as viewed from above) while bunches of positrons (anti-electrons) circulate clockwise. Electrons and positrons have the same mass but opposite charge, so the same bending magnets keep them within the storage ring circulating in opposite directions. The bunches collide at the center of the detector (see Fig 2.1).

The acceleration process begins with the production of a stream of electrons off a hot cathode, in the same manner as in a cathode ray tube (i.e. a television). A linear

[1] A play on the acronym CESR.

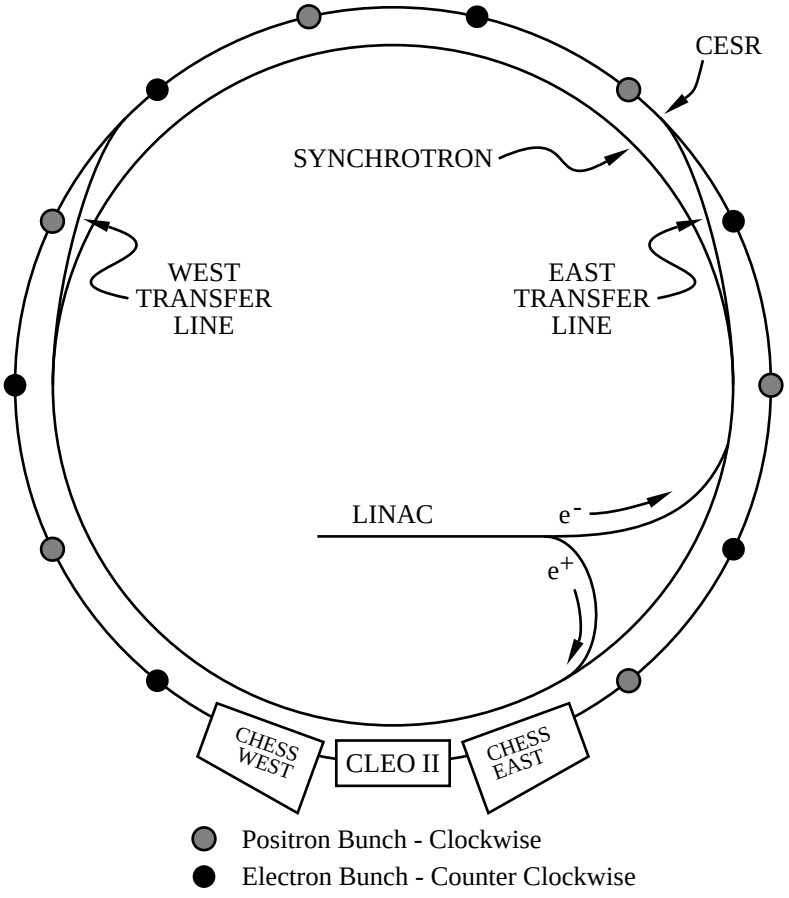

Figure 2.1: Cornell Electron Storage Ring (CESR).

accelerator (linac) boosts the energy of the electrons to about 150 MeV[2], and then injects the electrons into the synchrotron. The synchrotron accelerates the electrons up to their full energy, typically around 5 GeV,[3] with the use of radio-frequency (RF) cavities.[4] A short pulse of an electromagnet kicks the fully accelerated electrons into the storage ring. This process continues until the CESR operator has stored the desired number of electrons. CESR normally runs with the electrons grouped in seven bunches spaced around the ring. A typical bunch contains 2×10^{12} electrons in a volume similar to a flattened pencil lead (r.m.s. of 18mm $\times$ 500μm $\times$ 10μm).

Positron injection begins when electrons in the linac bombard a tungsten target. The collision produces positron-electron pairs. The positrons are then accelerated in the linac, and then bending magnets focus and steer them into the synchrotron in the opposite direction from the electrons. The positrons then follow the same acceleration process as the electrons do. In practice, the CESR operator stores the positrons first, because they are more difficult to fill.

The orbits of the electrons and positrons are engineered so that the bunches oscillate around the center of the storage ring pipe in such away that when electron and positron bunches pass each other they miss except at the one point located in the center of the detector. This minimizes the defocusing effects of beam-beam interactions. At this special point electrons and positrons collide. In normal operation interesting collisions occur about ten to twenty times a second.

As the electrons and positrons circulate, they radiate energy in the form of x-rays (synchrotron radiation), losing an average of 1 MeV per turn per particle. The RF cavities add this energy back on every loop. While high energy physicists view the energy loss as a problem, other scientist make use of the very intense and well focused

---

[2]An MeV is a million eV, the energy an electron or other singly charged particle gains when it transverse a voltage difference of one Volt.

[3]A GeV is a billion eV.

[4]The electrons ride on the RF wave similar to the way a surfer rides on a water wave.

x-rays for the study of materials. Cornell has set up a facility called CHESS (Cornell High Energy Synchrotron Source) to exploit this phenomenon.

As the particles circulate, some collide with the residual gas (the synchrotron ring has a very high but imperfect vacuum, typically 10^{-9} torr[5]) and some drift too far off the proper orbit and collide with the walls of the ring. Positron-electron collisions in the interaction region also remove particles from the bunches. As a result, the intensity of the beams decays. Typically after about an hour of running, the operators take ten or fifteen minutes to rejuvenate the beams.

2.2 THE DETECTOR: INTRODUCTION

We use the CLEO-II detector to measure the direction and momentum as well as to determine the identity of particles produced in the collisions of the electrons and positrons. Only "long lived" detectable particles are observed (photons, electrons, muons, charged pions, charged kaons and protons). We combine the information about the particles which are detected to try to reconstruct their parent particles.[6] A more complete description of the components of the detector follows this elementary introduction.

Particles interact electromagnetically with the medium they pass through. In a typical interaction, a charge particle knocks off outer electrons of atoms, leaving a trail of ionization. We can detect and measure this trail and thus determine where the particle passed. We exploit this phenomenon in our three tracking chambers and our muon detectors (described below) by collecting the charge liberated by the ionization of the gas on wires. We exploit a similar phenomenon in our "time-of-flight" detectors by detecting the light given off when an atom excited by the passage of a charged particle

[5] A torr is a millimeter of Mercury.

[6] Knowing the daughter particles' energies and momenta, we exploit energy and momentum conservation to calculate the parent's energy and momentum. Then using the relationship $M^2 = \sqrt{E^2 - P^2}$ where M is mass, E is energy and P is momentum, we can calculate the "invariant mass" of the hypothetical parent particle.

returns to the ground state.

A combination of two phenomena leads to the production of electromagnetic showers. Electrons also lose energy through the process called bremsstrahlung. The relatively light electron radiates photons when abruptly decelerated by the electric field of a nucleus. High-energy photons lose energy through the creation of electron-positron pairs in the field of nearby nuclei. The combination of bremsstrahlung and pair production leads to electromagnetic cascade showers, where a high energy electron radiates a high energy photon that then produces a high energy electron-positron pair, which both radiate photons, etc. High energy photons can just as easily trigger a cascade. Eventually all the energy of the initial electron or photon ends up in a large number of particles of low energy. The low energy particles lose their energy through ionization. A measure of the total ionization in a shower reflects the energy of the initial photon or electron. Note that heavier particles such as muons leave very little energy behind by this process, passing through material with relatively little deflection. We take advantage of showers in our cesium iodide crystal detector both to both measure the energy of photons and to identify electron tracks.

2.3 THE CLEO-II DETECTOR

The CLEO collaboration designed the CLEO-II detector (see Fig 2.2 and Fig 2.3) to have excellent charged and neutral particle tracking. We have published a complete description of the CLEO-II detector in the journal Nuclear Instrumentation Methods[8].

From the center of the detector, where the electron-positron collisions take place, the particles pass through the beam pipe wall into the central detector (CD) region. The particles pass successively through three tracking chambers. They follow a helical path as a result of a magnetic field (see below). The amount of curvature gives us the magnitude of the transverse component of the particles' momenta.

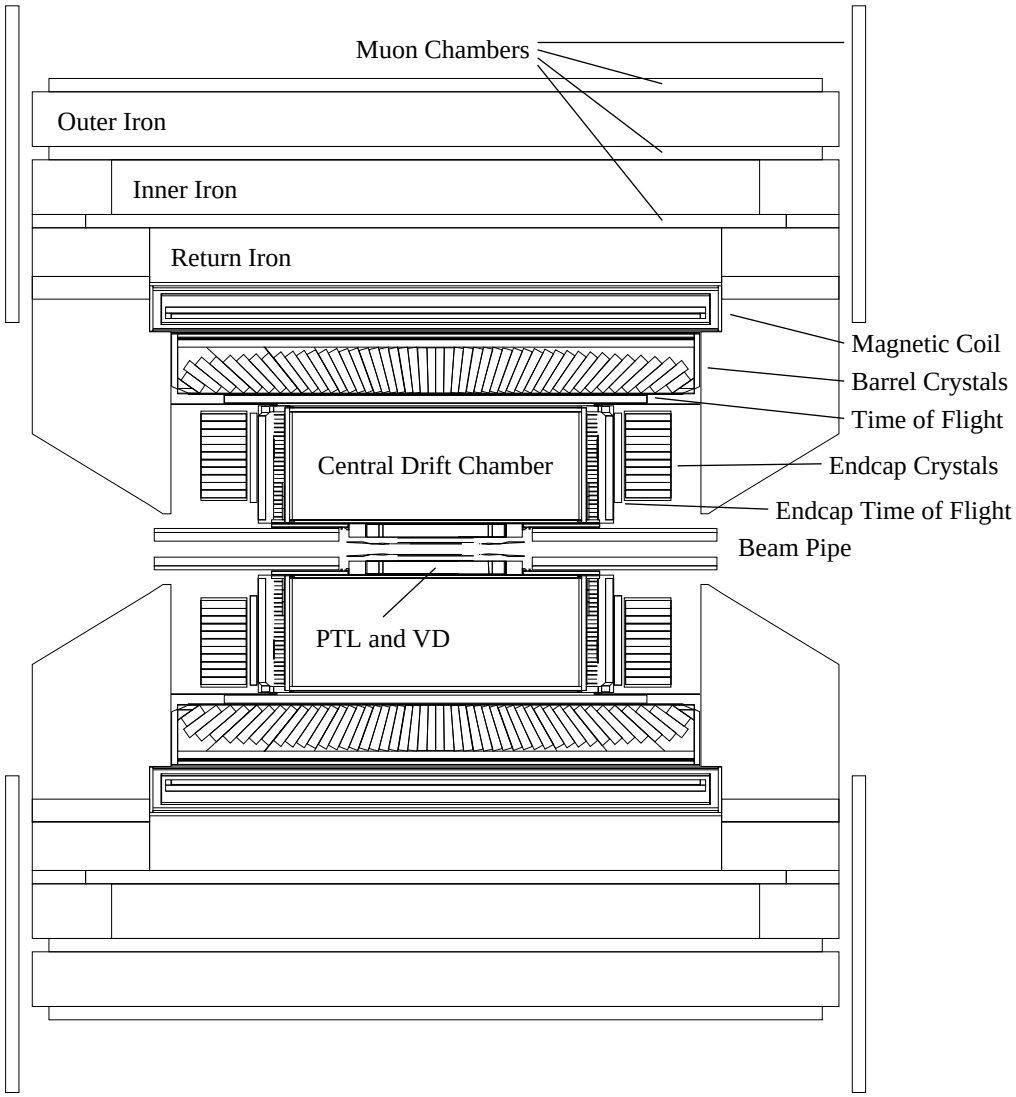

Figure 2.2: CLEO-II Detector: Cross section, side view.

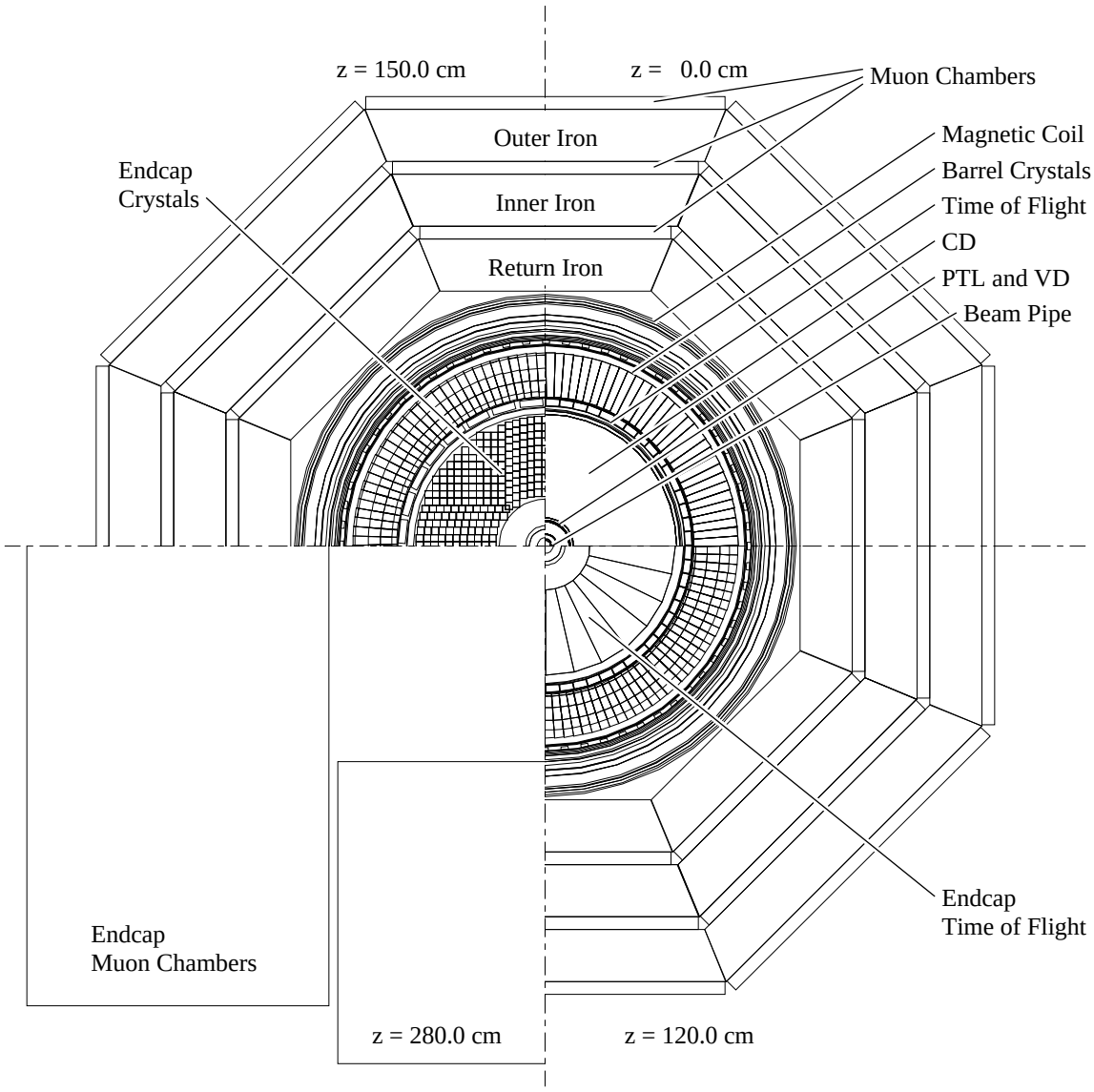

Figure 2.3: CLEO-II Detector: Cross sections at different places, end view. The value 'z' is the number of centimeters from the center of the detector.

Particles that pass all the way through the tracking chambers enter the time-of-flight (TOF) scintillator producing sparks of light. We discriminate between the possible identities of a particle by measuring the elapsed time between beam crossing (the time of the collision) and the arrival of the particles at the TOF detectors. The time a particle takes depends on the length of its path, its momentum (measured with the tracking chambers) and its mass.

Both neutral and charged particles that pass through the TOF detectors enter the cesium iodide calorimeter. The calorimeter measures very accurately the energy and position of the "showers" that the particles leave behind. Photons and electrons lose almost all their energy in these showers, while other particles such as muons lose very little. In the case of photons, the location and magnitude of the shower measures the photon's direction (knowing the photon originated at the collision point) and energy. In the case of a charged particle, a comparison of the energy of the shower to the momentum of the particle allows one to identify electron candidates.

The central detector resides inside a superconducting coil that generates a uniform magnetic field. The field points along the beam line (z axis)[7] and has a magnitude of 1.5 Tesla. The flux returns outside the coil through several layers of steel plates. The steel plates also serve as shielding for the muon detectors. Muons travel significantly further through material than other charged particles. We identify muons as those particles that make it through the steel and create hits in the muon detectors. Some non-muons will "punch" through (creating "fakes") and some lower momenta muons will "range out" (lose all their energy) and not make it to the muon detectors.

---

[7]We use a cylindrical coordinate system for describing the CLEO-II detector where the z axis is parallel to the beam pipe).

2.3.1 The Beam Pipe

A thin-walled beryllium pipe separates the vacuum of the storage ring from the detector. The beryllium pipe has a thickness of 500 microns, a length of 33 cm, and a radius of 3.5 cm. A layer of silver (25 microns) and a layer of nickel (< 1 micron) plate the inside of the pipe to reduce the amount of synchrotron radiation entering the detector. The pipe covers a solid angle of 99% of 4π and presents 0.44% radiation lengths[8] to normally incident outgoing particles. Two cylindrical aluminum pieces connect the beryllium pipe to the rest of the CESR beam pipe. Radiation masks located farther away screen direct synchrotron radiation from the pipe.

2.3.2 The Drift Chambers

As charged particles pass through gas, they leave behind a trail of ionization. In a drift chamber, ions and electrons move in opposite direction in an electric field. The electrons drift toward a "sense" or anode wire while the ions drift towards a cathode wire or pad. The electric field near the sense wire grows in inverse proportion to the radius. As the electrons approach the wire they undergo strong acceleration and cause ionization of the gas. Electrons freed by this ionization cause further ionization as they too undergo acceleration. This creates an "avalanche" of charge which collects on the wire. Electronics at both ends of the sense wire amplify the charge pulses. We can establish a relationship that links the time that the electrons drift to the distance from the wire where the ionization took place. An array of such wires allows the precise measurement of a particle's trajectory. In CLEO-II, we use three chambers concentric with the beam pipe for tracking. The wires in all the chambers run parallel or nearly parallel to the beam pipe, allowing excellent tracking in the r-ϕ plane.

---

[8] A radiation length is the thickness of a material that reduces the energy of an electron to $1/e$ (1/2.718) of its initial value via bremsstrahlung.

The PTL

A particle exiting the beam pipe first passes through the Precision Tracking Layer or PTL (see Fig. 2.4). We use the PTL to locate the origin of a particle track precisely. The PTL consists of six concentric rings with 64 aluminized mylar tubes in each layer. The tubes in one layer are offset from the tubes in the previous layer. Each tube serves as a cathode while a wire strung down the middle serves as an anode. The active region extends from 4.5 cm to 7.5 cm in the radial direction and from -22.5 to 22.5 cm in z. The tubes have a diameter between 2.2 and 3.5 mm, depending on the layer, with those further away from the origin having larger diameters. We operate the chambers with an anode voltage of about 1500 V. For the first half of the data used in this thesis the gas used was a mixture of 50% argon and 50% ethane at atmospheric pressure. With this gas we a achieved a position resolution of $\sim$100 microns. For the second half of the data used in this thesis the gas DME (Dimethyl Ether) was substituted, improving the resolution to $\sim$60 microns. The PTL presents a total of 0.28% radiation lengths radially to a particle that passes through the chamber. The PTL makes measurements only in the r-ϕ plane.

The Vertex Detector

Particles that pass through the PTL next encounter the Vertex Detector or VD. The VD extends from 8.0 to 16.6 cm in the radial direction and from -35.0 cm to 35.0 cm in z. It consists of 10 layers of drift cells with 64 cells per layer for the inner five layers, and 96 for the outer five layers. A sense wire in the center of a hexagonal group of six cathode or field wires creates the potential in each cell. Neighboring cells share field wires in a slightly distorted honeycomb pattern. The VD also uses a 50% argon and 50% ethane gas mixture, but at a higher pressure (20 psi) to reduce the resolution limiting effect of diffusion.

We measure the z position of the track with cathode strips placed on the insides

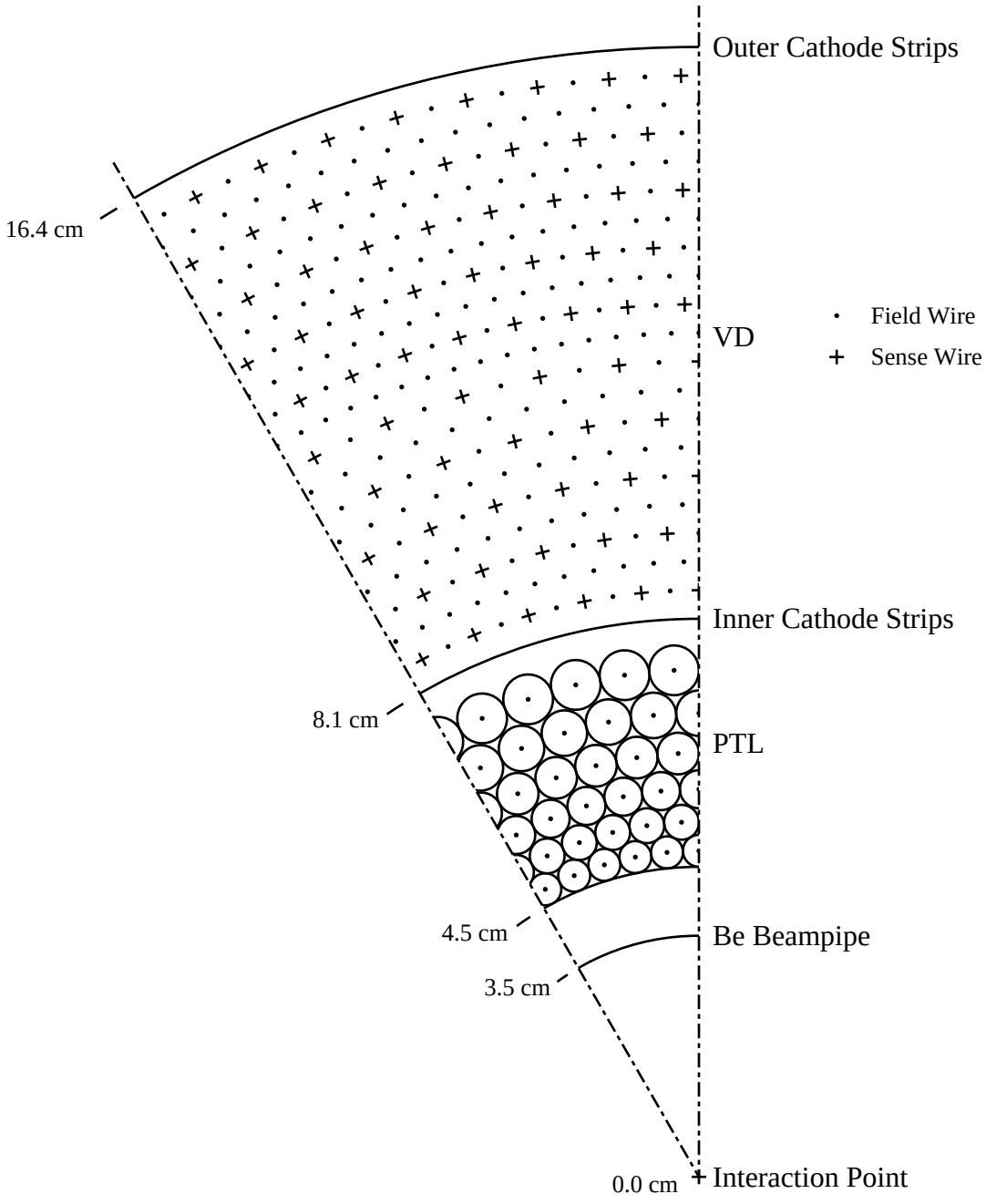

Figure 2.4: Beam Pipe, PTL and VD.

of both the inner and outer radius walls of the VD. The cathode strips pick up an induced charge from the slow moving ions created by passing particles near the VD walls (while the wires collect the electrons). The strips consist of eight microns of aluminum deposited on 75 micron thick mylar. The surface is divided into a series of eight segments around the circumference with 64 4 mm wide strips on the inner surface, and 96 6 mm wide strips on the outer surface. We obtain a resolution of about 800 microns in z from the strips. The cathodes have an efficiency of 83% for the inner layer and 78% for the outer layer.

For about 90% of the data used for this thesis, we used charge division to help measure the z position of a track. The ratio of charge measured at the two ends of the highly resistive sense wire gives a measure of the z position of the track; the closer the track to one end the more of the charge collected at that end.

The Main Drift Chamber

Outside the VD resides the main drift chamber or DR. The DR extends from 17.8 cm to 94.7 cm in radius and -94.5 to 94.5 cm in length. It subtends 94% of 4π at its inner surface and 71% of 4π at its outer surface. We use the DR for accurately measuring a track's momentum and position, as well as for particle identification. It consists of 51 concentric layers with a total of 12,240 sense wires and 36,240 field wires (see Fig 2.1). As with the VD, cathodes for z measurement reside on the inside of both the inner and outer cylindrical walls.

Groups of three or five "axial" layers alternate with a "stereo" layer. Axial layers have their sense wires parallel to the z axis. The stereo layers have a small tilt with respect to the axial layers to help measure tracks' z positions. Within an axial grouping, the sense and field wires line up radially. Adjacent layers have a half-cell azimuthal offset to help resolve which side of the wire the particle passed. Moving radially outward, the number of cells per layer increases from 96 to 384 in order to maintain an approximate

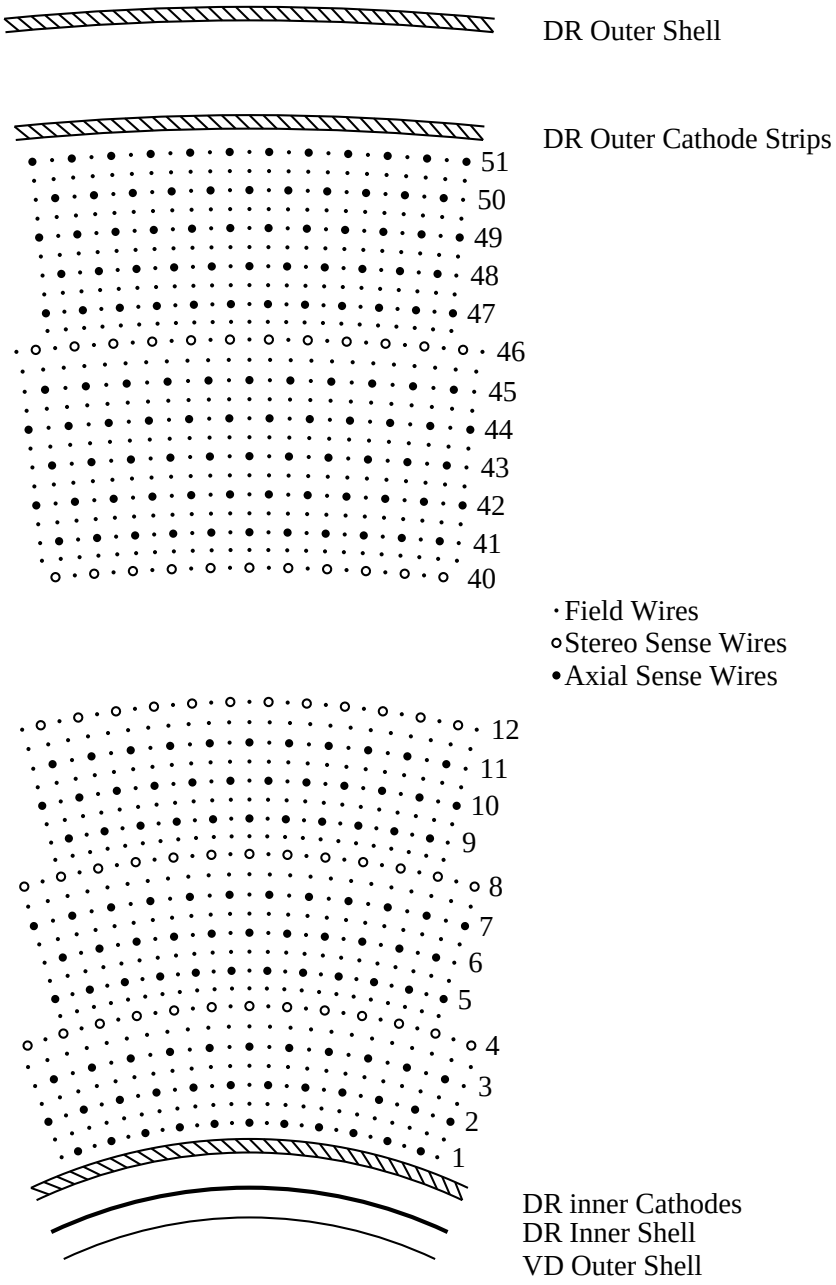

Figure 2.5: Main Drift Chamber.

14 mm by 14 mm cell size. The tilt of the stereo wires ranges from 1.91° for the innermost radial layer to 3.50° for the outermost radial layer in a plane tangent to the layer.

Each cell has a gold-plated 20 micron tungsten sense wire surrounded by eight field wires in a square pattern. The smaller the sense wire, the greater the amplification avalanche. Too small of a wire, however, results in frequent wire breakage. We use aluminum for the field wires in the first forty layers to reduce multiple scattering and copper-beryllium for the wires in the remaining layers.

The amount of ionization a particle leaves behind depends on its speed, and thus its mass and momentum. The magnitude of the signal on the sense wire measures the amount of ionization, providing a useful method of particle identification. Fig 2.6 shows the measured energy loss from our data. Clear bands can be distinguished for various long lived particles.

Two large 1.25 inch thick aluminum plates support the wires at each end. A quarter inch thick cylindrical outer shell provides the axial support to keep the plates apart. A thin inner shell of a graphite epoxy composite provides a gas seal at the center.

As with the VD, cathode pads on both the inner and outer surfaces of the CD provide a measure of the z position of a track.

2.3.3 The Time-of-Flight Detectors

Two sets of scintillation detectors make up the time-of-flight or TOF system. One set forms a cylinder around the CD (the barrel TOF counters), covering from 36° to 144° in polar angle. Another set covers the ends (the end-cap TOF counters), covering from 15° to 36° on one end and from 144° to 165° on the other. The detectors cover a total solid angle of 97% of 4π. We use them to start clocks that stop counting at a precise time after a beam crossing takes place, thereby allowing the determination of the time it takes a particle to travel from the center of the detector to the TOF layer. This time,

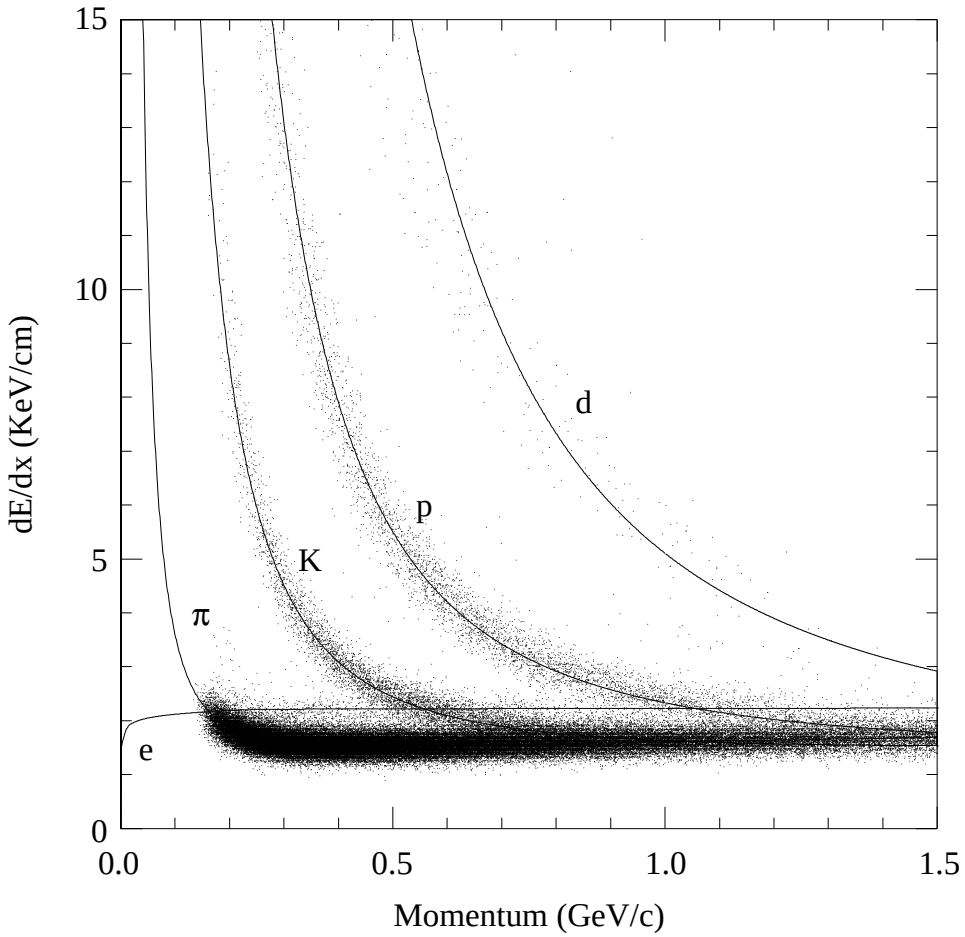

Figure 2.6: Specific ionization (dE/dx) from CLEO-II data. The theoretical energy loss curves for various particles are overlaid.

together with knowledge of a particle's momentum, allows an estimate of the particle's mass and thus its identity. The TOF detectors also serve as a major component of the trigger, the system of electronics that tells us we have a real event and should save the detector output, as is described later in this chapter.

Scintillator material gives off light as particles pass through. We use a plastic doped with organic molecules. A particle passing through the plastic excites the organic molecules. The decaying molecules emit ultraviolet light. Dye molecules embedded with the organic materials then convert the ultraviolet light to light in the blue region. This light internally reflects down the length of the scintillator into a plastic light pipe that directs it into a photomultiplier tube. The photomultiplier tube and the attached electronics amplify and measure the signal. The barrel time-of-flight system consists of 64 separate strips of Bicron BC-408 scintillator, each 5 cm thick. UVT lucite light pipes connect the scintillator to the photomultiplier tubes mounted outside the detector. The end-cap TOF system consist of 28 wedges of the same type of scintillator on each end. A prism reflects the light from the scintillator into photomultipliers mounted parallel to the magnetic field of the detector. This orientation reduces the effect of the magnetic field on the photomultipliers' operation. The resolution for the detectors ranges from 120 picoseconds to 250 picoseconds, with an average of 170 picoseconds.[9] Fig 2.7 shows the measured $1/\beta$ from our data.[10] Clear bands can be distinguished for various long lived particles.

2.3.4 The Crystal Calorimeter

Directly outside both sets of TOF detectors resides the Crystal Calorimeter or CC. The CC, like the TOF system, consists of a barrel and two end caps. The CC is made up of scintillating thallium doped cesium iodide crystal blocks, each typically 30 cm in

[9] A particle traveling at the speed of light travels 3 cm in 100 picoseconds.

[10] β is the ratio of a particle's velocity to that of light.

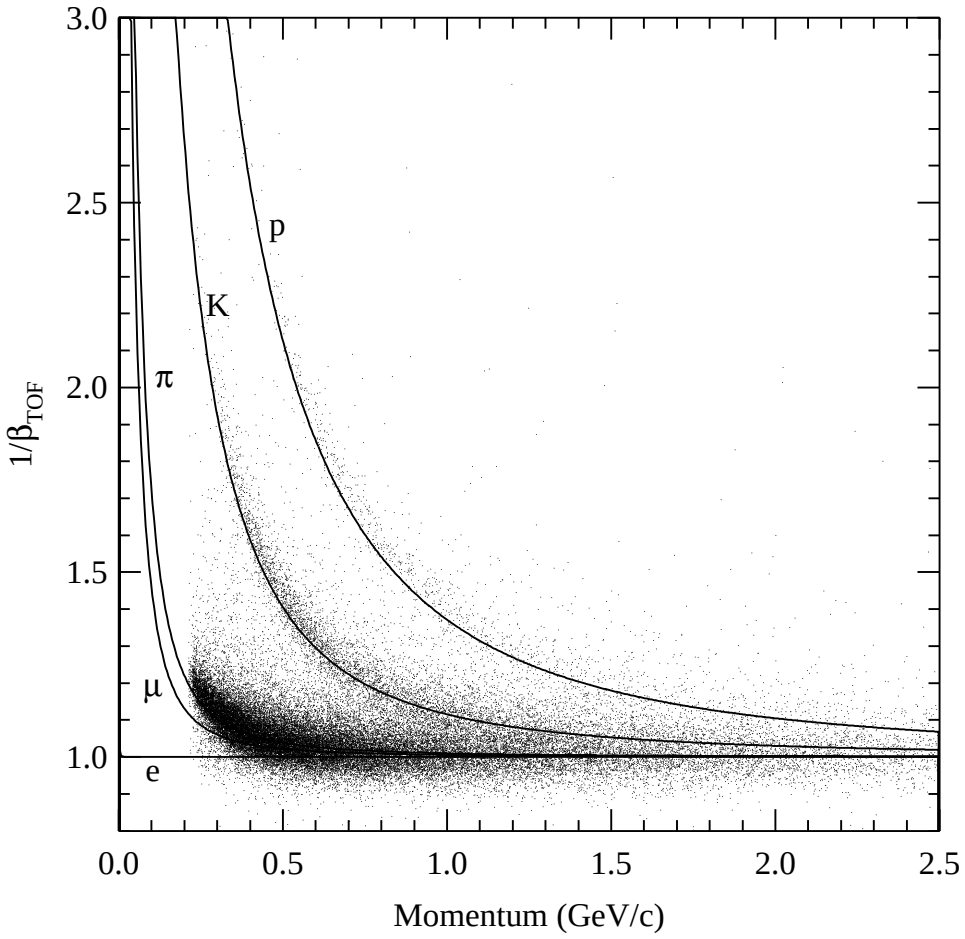

Figure 2.7: $1/\beta$ as measured by TOF from CLEO-II data. The theoretical values for various particles are overlaid.

height by 5 cm in width and length. The barrel crystals taper so that they fit flush to each other in a cylinder with the small end pointing a few centimeters away from the interaction point. The crystals don't point exactly at the interaction point, in order to prevent a photon from slipping through a crack. The cesium iodide crystals have excellent properties for the conversion of electron and photon energy to light through cascade showers. The crystals present 16 radiation lengths to electrons and photons, ensuring that little of the shower leaks out the back of the crystals. Photodiodes matched to the wave length of the light convert the light into a measurable electronic signal. We establish through calibration a relationship between energy deposited and the pulse height of the readout.

The barrel contains 6144 crystals arrayed in 128 rows in the z direction around the circumference of the barrel, with 48 crystals in each row. An aluminum "egg-crate" holds them firmly in place. The design of the system minimizes material in front of the crystals and reduces the chance of a particle beginning to shower before reaching the crystals, which would degrade the crystals' energy and position resolutions. Each end cap contains 828 rectangular crystals stacked in a large annulus. The resolution of the end-cap crystals suffers as the result of their location behind the read-out electronics and support plates of the drift chambers. Showers extend across many crystals. Only crystals which have at least 2 MeV of energy deposited in them, and which are near to a crystal with 10 MeV of energy, have their data read out. We combine the information from neighboring crystals off-line to find a shower's center and magnitude.

2.3.5 The Superconducting Coil

A superconducting coil encircles the crystal barrel. The coil produces a very uniform 1.5-Tesla field in the z direction (parallel to the beam pipe) throughout the drift chambers and the calorimeter. The field causes the charged particles to follow a helical path.

The amount of curvature reflects the momentum of the particle. The 7000-kg cylindrical coil resides outside the crystals, in order not to degrade the crystals' resolution. The coil consists of two layers, each with 650 turns of a cable made by embedding wires of a niobium-titanium-copper alloy in a high purity aluminum stabilizer. Liquid helium from a dewar mounted above the detector provides cooling by a thermosyphon system. The magnetic flux returns outside the coil through a 800,000-kg steel yoke that also screens the muon detectors.

2.3.6 The Muon Chambers

Muons traverse material with less chance of absorption than other charged particles since they are not affected by the strong interaction and they are more massive than electrons. We exploit this property to distinguish them from other particles. Eight "octants," consisting of three layers of 30 cm thick steel interleaved with "super layers" of muon detectors cover the barrel region[9]. A super layer consists of three single layers of proportional drift cells formed from extruded plastic. Graphite coats the inside of the plastic cell to provide a cathode, and a wire strung down the center serves as the anode. Copper strips outside the cell run perpendicular to the wires and measure the z position of a hit by inductive coupling. To reduce the cost of electronics, wires from neighboring counters are connected together in series, each separated by a 100-Ω resistor, to form a "multiplet." Charge division flags the hit wire. Single superlayers cover the end region of the detector.

In the barrel a muon must have at least 0.8 GeV/c of momentum to reach the first super layer, 1.4 GeV/c to reach the second, and 1.8 GeV/c to reach the third; in the end cap a muon must have at least 1.4 GeV/c of momentum to reach the only layer. The total system covers 90% of 4π.

2.3.7 The Trigger

A colliding beam experiment such as ours collects an enormous amount of data. If we did not have a way of sifting out the interesting events from the non-interesting ones, our data acquisition system would be overwhelmed. Even after sifting we write to magnetic tape on the order of 2 gigabytes of data per day (100 kbytes per event, 20,000 events in a day of good running). In addition, it takes a finite time to write the data out from the various detectors to temporary storage on magnetic disk. During the writing, the data acquisition cannot collect data, thus producing a period of dead time. Writing out only the interesting events reduces the dead time and saves storage space. The event-selection process begins with a three-level trigger system[10]. The detector continually collects data with a timing structure based on the crossing frequency at the interaction region. In the absence of a trigger, however, the information disappears after a short time. For example, charges collected on sense wires decay with about a 1.3-μsecond decay time constant. A very fast and very loose first stage trigger freezes the information while two further stages evaluate the event's physics content.

The first-stage trigger, level zero (L0), uses information from the TOF scintillators, the VD and the CsI crystals to decide if an interesting event may have occurred. Different trigger "lines" combine the information in different ways, each line designed to catch some interesting class of events. The trigger fires when any line turns on. When an LO trigger occurs each detector freezes the information it has while the level 1 (L1) trigger checks if its criteria have been met. The bunches of electrons and positrons cross within the detector at a 2.7 MHz rate; L0 triggers occur at a 20-kHz rate.

The L1 trigger uses information from the CD in addition to that from the detectors used by the L0 trigger to make a more sophisticated (but slower) decision on whether the event should be kept. Electronic circuitry checks to see if the data is consistent with having a minimum number of tracks in the event. It takes approximately 1.0 μsecond for all the information to arrive at the L1 circuitry. This introduces a minimum dead

time of 2% at an L0 trigger rate of 20 kHz. The L1 trigger fires at about 25-50 Hz. If the L1 trigger fires, an evaluation of the level 2 (L2) trigger takes place. If the L1 trigger does not fire, the detectors and gates are reset.

The L2 trigger uses information from the VD and CD. It takes approximately 50 μseconds to ready this information. The L2 trigger typically fires between 10 and 20 Hz, depending on CESR's running conditions. When an L2 trigger happens, the CLEO-II data acquisition system writes out data from all the detector components with "hits" to disk. A further filtering of the data takes place with software before dumping the data to tape.

2.4 DATA ACQUISITION AND ONLINE DATA FILTERING

After an L2 trigger has occurred, we write out the data. This process begins with digitization of the analog data from each detector element in parallel. Only elements that meet certain criteria have their data collected, reducing the raw data in each event. For example drift chamber pulses must exceed a predetermined minimum threshold. Local buffers store the data until read by a microprocessor system. Initially we used a VAX-3200 microprocessor which took an average of 12 msec to read out an event. After an upgrade involving four Motorola 68040 microprocessors, it now takes an average of 2 msec to read out an event[11].

Originally all data from events passing the L2 trigger were written to tape. In order to handle the increase in collision rate made possible by improvements to the accelerator, to allow looser triggers and to reduce the amount of data we need to further analyze, we now discard some events after further online processing. A software program called level 3 running on a DECstation 5000 filters the data, discarding uninteresting events. We need some types of events, such as Bhabha scattering, for off-line calibration of

detector components, but the rate with which such events occur exceeds the required need. Level 3 throws away predetermined percentages of such events. In all cases we keep a certain percentage of "random" triggers to check that what we throw away is uninteresting.

We store data that has passed through the online filter temporarily on disk and then permanently on 4 mm DAT tape. Before being useful for analysis the data must be processed off-line to reconstruct details of the events such as the particles' trajectories, momenta and type. The next chapter contains the details of the reconstruction software used for this purpose.

Chapter 3

DATA REDUCTION, DETECTOR SIMULATION, AND PARTICLE IDENTIFICATION

When an interaction occurs in the CLEO-II detector, hundreds or even thousands of sensitive elements record the passage of the particles produced. If the trigger logic determines the event to be of potential interest, the data acquisition system reads out the information and passes it to the on-line computer for preliminary analysis and storage. Events occur at a rate of 10-20 Hz, and the detector collects data around the clock, so the volume of information generated is enormous. To use this information we must process it from the raw format of digitized pulse heights and times into the physical quantities like momentum and energy which we need to reconstruct the production and decay processes. We must also reduce it from the terabytes[1] it occupies in the raw form

[1] A terabyte is equivalent to a trillion characters.

to a size and format which is amenable to off-line physics analysis.

The tasks involved in this process include sophisticated pattern recognition. We must, for example, link together the series of hits on drift chamber wires to reconstruct the particles' trajectories and thus their momenta and direction. This data reduction takes place within the framework of the software program CLEVER. CLEVER reads in raw data an event at a time from the data tapes written by the on-line system. Different "processors" can be called to analyze different parts of the data. For example the processors TRIO and DUET reconstruct tracks in the drift chambers, and the processor CCFC finds "clusters" produced by particles which interact in the CsI calorimeter. Some processors depend on the output of other processors. For example the track-shower matching processor, CDCC, requires output from both the tracking and the shower cluster finding processors.

Short descriptions of the most important processors are given in this chapter. We have constructed a standard sequence of processors which we use on all the data. We call the process of reducing the data set "PASS2." The output of PASS2 is the input data for all CLEO-II analyses.

The CLEO-II detector is a very complex device. We utilize a full simulation ("Monte Carlo") of the physics events and detector response in order to check our understanding of how the detector works and to determine quantities that depend on the correlation of many parameters. One of the important quantities is the "efficiency" for detecting a specific type of event. For example, what percentage of the time do we detect a J/ψ meson produced in a B decay when it decays to an electron-positron pair? This efficiency can be broken down into several parts. First there is the geometric acceptance, which must include the correlation between the electron and positron. Second, for an electron and positron which both go through the drift chamber, there is an efficiency for the successful reconstruction of their tracks. Finally, there is an efficiency associated with correctly identifying the tracks as being from an electron and positron.

Simulation is a multistep process. First, the program "QQ" generates the particles produced by an e^+e^- annihilation. Embedded within QQ are numerous routines that simulate the various production and decay mechanisms[12, 13, 14]. QQ has been tuned to match our current understanding of particle dynamics. Within QQ we can specify a decay chain corresponding to the process we want to study. For example, for determining the efficiency of detecting J/ψ's from B decay, we can cause all B mesons to decay with a J/ψ, while the accompanying $\overline{B}$ mesons decay generically. QQ not only determines what particles are produced but also their momenta and angular distributions.

After QQ has produced a set of events, we use the program "CLEOG" to propagate the particles step by step through a representation of our detector. At each step random numbers are generated to determine if the particle interacts or decays. The probability of interaction or decay is based on our current understanding of particle physics. If an interaction results, its effect on the particle and detector is also randomly determined, again based on physical probabilities. If the particle interacts in an active region of a detector (i.e. one that is instrumented) then the simulation also determines the detector's response. For example, as a particle passes through a drift chamber, first its energy loss is determined for each region around an anode wire. Next the amount of charge and time it takes that charge to reach the wire is calculated. Finally the response of the electronics and the digitization process is determined and the output recorded. In this way, we build up simulated events that look to our analysis programs as identical to the real data as possible.

CLEOG is based on the CERN[2] software "GEANT"[15]. GEANT includes the structure necessary to describe the detector in detail as well as to simulate particle interactions. GEANT models hadronic interactions (through routines called GHEISHA

[2]Formerly: Centre Europeen pour la Recherche Nucleaire, now: Organisation Europeenne pour la Recherche Nucleaire, or in English: European Organization for Nuclear Research.

and NUCRIN), electromagnetic showers (through the EGS package), multiple scattering, annihilation, ionization and many other physics processes.

In order to rely on the simulation for determining detector parameters such as efficiency we need to check on how close the output matches that of the real detector. If we know that the simulation differs systematically from the real output we can correct our results for that difference. We also need to have an idea of how well we know the agreement between the Monte Carlo and the real detector so that we can estimate our systematic errors.

3.1 TRACKING

We utilize the processors TRIO[16] and DUET[17] to find and determine accurately the momentum and direction of particles that leave tracks within the drift chambers. TRIO runs very quickly but misses many tracks, while DUET does a better job of both finding and measuring tracks, but takes considerable computer time. We use TRIO for on-line analysis because of its speed, and DUET for off-line analysis to obtain the best possible track reconstruction.

Once a track has been found, we can calculate its transverse momentum (the component of momentum perpendicular to the beam direction) from

$$p_t = 0.3\mathrm{RB}, \tag{3.1}$$

where p_t is the transverse momentum measured in GeV/c, R is the radius of the helix in meters, and B is the strength of the magnetic field in Tesla. The total momentum of the track is then

$$p = p_t\sqrt{1 + \cot(\theta)^2}, \tag{3.2}$$

where θ is the angle the track makes with respect to the beam direction at the interaction point.

3.1.1 TRIO

TRIO searches for groups of hits in three radially adjoining drift chamber cells. In the PTL, TRIO uses any set of three adjacent layers. In the VD the three hits must come from either the first five layers or the second five layers, because of the different number of cells in each layer. In the CD, the hits must come from the triplet layers between stereo layers. The hits must agree with the hypothesis of a track coming from near the center of the detector.

Once TRIO has found all the triplets in an event, it then tries to combine the innermost triplets with the outermost triplets in each detector to form a track candidate. It uses the two triplets to calculate a helical path. The path must pass near the interaction point. Next TRIO attempts to add triplets in between and near the path. If it has matched enough triplets, usually four, it recalculates the track candidate's parameters and attempts again to add more triplets. Finally, TRIO calculates the quality of the track's fit and adds it to the track list if the fit is satisfactory.

Wire inefficiencies can cause TRIO serious problems as a single missing hit throws out an entire triplet. Also TRIO has trouble with tracks that have a small radius of curvature. It works best for radial tracks.

3.1.2 DUET

DUET builds up tracks by stringing hits together in the r-ϕ plane to form larger and larger segments. Segments begin with two adjacent hits. Nearby hits are then added to form a "tree." DUET searches the tree for the longest segment where all the hits are consistent with a circle. DUET then adds information about the z position using the stereo wires and cathode before refitting the segment to a helix. Next DUET stores the track in a list and deletes the used hits from the tree structure. DUET repeats the search with the remaining segments. To reduce the time taken for the search, DUET uses TRIO tracks as seeds. The track list DUET produces contains track numbers,

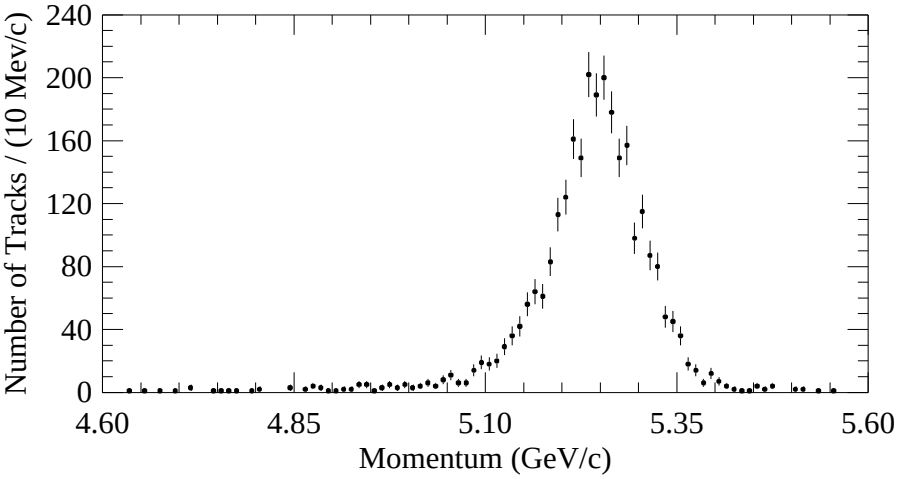

Figure 3.1: Momentum resolution for muons from the process $e^+e^- \rightarrow \mu^+\mu^-$.

momenta, directions, positions and various parameters that characterize the quality of the fits.

DUET has a resolution in the r-ϕ plane of:

$$(\delta p_t/p_t)^2 = (0.0011 p_t)^2 + (0.0067)^2, \tag{3.3}$$

where p_t is measured in GeV/c. The first term is from errors in measuring the electron drift distances (and thus the distance from the wire to the track) while the second term comes from multiple scattering (the particle being deflected by interactions with the gas) which distorts the helix.

The resolution can be checked with a source of monoenergetic tracks. Mu-pairs from $e^+e^- \rightarrow \mu^+\mu^-$ are a clean source of such tracks. Fig 3.1 shows the momentum distribution for mu-pairs. The measured resolution for the 5.28 GeV/c tracks is 0.051 GeV/c compared to the expected resolution of 0.047 GeV/c. The agreement is reasonable since the expected resolution only accounts for the transverse part.

The simulation of track finding has been checked very thoroughly by a number of techniques[18]. For example one can compare the ratio $K^0_S \rightarrow \pi^+\pi^-$/ $K^0_S \rightarrow \pi^0\pi^0$ in Monte Carlo to the same ratio for data. The π^0's decay to photons and thus their detection

does not involve track finding. Each of the checks has its weaknesses. In the K_S^0 method, we depend on the accurate simulation of the crystal calorimeter. By using many methods, we can come up with a number that represents our best guess at the systematic error for how well the Monte Carlo track finding efficiency matches that for data. For most tracks the number is 2%[18, 19]. For high momentum tracks the number is 1%[20].

3.2 SHOWER RECONSTRUCTION

The processor "CCFC" reconstructs showers out of individual crystals with energy deposits[21]. Shower reconstruction begins with a search for "seed" crystals. A seed crystal must have at least 10 MeV of energy deposited in it and have the largest energy in its neighborhood. An algorithm then adds in neighboring crystals to form a cluster. The number of crystals the algorithm uses to form a cluster depends on the cluster's energy logarithmically in a way that minimizes the degradation of energy resolution due to noise (if the number of crystals is too small, energy from the cluster is lost, while if the number is too large, noise is unnecessarily added in). The number of crystals in a cluster ranges from 4 at 25 MeV to 17 at 4 GeV. A cluster may have a non-integer number of crystals and a crystal may have its energy split between adjacent clusters. An energy weighted average over the center of each cell determines the lateral center of the shower. The depth of the shower is calculated from the energy of the shower using a Monte Carlo derived function.

The energy resolution of the calorimeter varies depending on the region. In the center of the barrel the resolution is very good (1.5% at 5 GeV), but it is not as good in the end cap (2.6% at 5 GeV) due to the additional material (drift chamber end plate and electronics) in front of the crystals[8].

A number of other shower parameters are stored. One very useful parameter is the ratio of the energies in the sets of 9 and 25 crystals surrounding and including the seed.

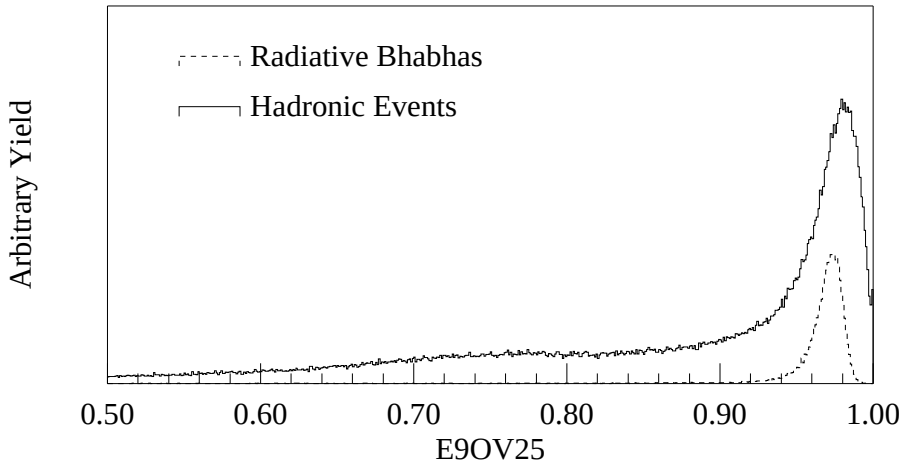

Figure 3.2: The ratio of the energy in the 9 most central crystals in a shower to the 25 most central crystals (E9OV25). The ratio is nearly one for electrons and photons, but often less than one for other particles. Plotted is E9OV25 for electrons from radiative Bhabhas and all particle tracks from generic hadronic decays. The tracks used were restricted to those with momentum between 0.8 and 3.5 GeV/c, and projecting into the center part of the barrel.

This ratio, called E9OE25, is almost 1 for photons and electrons but is generally smaller for hadrons (a consequence of interacting electromagnetically rather than strongly).

The Monte Carlo shower simulation can be checked similarly to the way the drift chamber simulation was checked. For example, we can compare the yields of $\eta \rightarrow \pi^+\pi^-\pi^0$ and $\pi^0 \rightarrow \gamma\gamma$ to $\eta \rightarrow \pi^+\pi^-\gamma$. Since there are two charged pions for each mode, the charged track efficiencies cancel. The presence of an additional photon in the first decay chain allows us to use the ratio to check the photon simulation. From these studies we estimate that the photon finding efficiency for Monte Carlo is within 2.5% of the real efficiency[18].

3.3 TRACK-SHOWER MATCHING

Matching tracks in the drift chamber to showers in the calorimeter is important for two reasons. The first is that it allows us to determine which showers are caused by

charged particles and which are caused by neutral particles (mostly photons). Second, the shower energy and shape are used to help identify electrons. Shower matching is done by the processor "CDCC"[22]. The first step in the matching process is to project the charged track into the crystals. CDCC then calculates the point where the track projection is closest to the shower center. The distance from this point to the line that connects the shower center to the origin is then determined. If this distance is less than 8 cm, the shower and track is tagged as a TYPE 1 match. This algorithm works well for the electromagnetic showers of electrons and muons. However, it has been determined that the centers of hadronic (pion and kaon) showers are often further away than than 8 cm. For this reason there is a second class of matching. In this case the criteria for matching is that the track project to within 8 cm of any crystal in the shower. These are TYPE 2 matches. Showers that are not matched to tracks are interpreted as photons.

3.4 PARTICLE IDENTIFICATION

The identification of particles is fundamental in deciphering what went on in an event. The only detectable particles (those which live long enough for us to detect and which interact with sufficient probability) are photons, electrons, muons, charged pions, charged kaons, protons and antiprotons. Particle identification in general is based on differences in the ways particles behave in the detector. For example, photons leave no tracks in the drift chamber, muons penetrate matter much more easily than other charged particles, and electrons lose almost all of their energy in the calorimeter.

Some of the differences in the behavior of different particle species results from differences in their masses. If you measure the momentum of a particle (which we do for charged particles with the drift chamber) and also measure the particle's speed, then you can determine the particle's mass:

$$\beta = \mathrm{P}/\mathrm{E}, \tag{3.4}$$

β is the ratio of the velocity of the particle to that of light, P is the magnitude of the momentum and E is the energy of the particle.

The particle's speed is measured directly with the TOF system and indirectly by measuring the specific ionization (dE/dx) in the central drift chamber.

3.4.1 dE/dx

For a given material, the amount of ionization that a charged particle deposits when passing through is a good measure of the particle's speed. In a large drift chamber such as the DR, the charge collected in the cells traversed provides a statistical sampling of the energy deposit for roughly equal amounts of gas. For CLEO-II, the CLEVER processor "DEDR" takes the raw data for each wire, corrects it for several effects, and extracts individual measurements of the energy deposited in the cell. For example, for particles that travel parallel to a wire, the ions created near the wire shield from the wire those created farther away. Thus the polar angle of a track will affect the amount of charge deposited. Once these corrections have been done, the value dE/dx can be calculated by dividing the corrected charge by the path length in the cell. From these values, the mean of the lowest 50% of the dE/dx measurements is calculated. The reason for using the lowest 50% is to eliminate the occasional large fluctuations that may occur when a high energy electron is knocked out[23]. The probability of this happening is small, but it causes a large increase in the measured energy loss.

Next DEDR compares the mean dE/dx loss with the expected means for each of the particles e, μ, π, K, and p. The difference between the measured and expected mean is divided by the expected width of the distributions to give a measure of how much the energy loss of the particle deviates from the expected loss. For example, the number of standard deviations the dE/dx measurement is away from the expected value for an electron (SGELDI) is

$$\text{SGELDI} = \frac{E_{measured}(P) - E^{e}_{expected}(P)}{\sigma_e}. \tag{3.5}$$

Both electron and hadron (π and K) identification for this thesis rely on dE/dx information.

3.4.2 TOF

The processor "TFAN" takes the raw TOF data and calculates, with corrections, the time it took a particle to travel from the interaction region to the TOF detector. The path length of the track is also calculated. The speed of the particle is then just $v = L/t$ where v is the speed, L the path length and t the time. Like DEDR, TFAN also calculates for each particle hypothesis (e, μ, π, K, and p) the number of standard deviations from the expected values.

3.4.3 Muon Identification

Muon identification takes place in the CLEVER processor MUTR[24]. Identification relies on the ability of muons to penetrate the cesium iodide crystals, magnet coil and iron to reach the muon detectors. The muon identification package projects each drift chamber track through the coil and iron to the muon detector layers, taking into account the magnetic field, multiple scattering, and energy loss. Under the muon hypothesis, it predicts which if any muon detectors should register hits. A muon candidate must have hits in all superlayers (see Chapter 2) where hits have been predicted as well as two hits in the last superlayer reached. Each muon candidate has a depth assigned to it representing the number of absorption lengths it has passed through.

A check of the Monte Carlo muon detection efficiency can be broken down into three parts: material effects, geometric acceptance and chamber efficiency. The latter two are to a good approximation independent of momentum while the first is significant in the threshold momentum region.

The agreement between Monte Carlo and data of the threshold momentum for detecting muons is very good, indicating that the material in the Monte Carlo description

is an accurate model of the real detector (see Fig. 3.3)[25]. This is verified by the agreement in the *shape* of the inclusive electron and muon momentum spectra, especially in the lower momentum regions (see Fig 3.4). [25, 26]. The shape of the muon spectrum in the region 1.3-1.5 GeV/c is very sensitive to the amount of material in the detector. Here one assumes that there is not a rapid variation in the tracking efficiency with momentum and that the efficiency for producing a hit in the muon chambers does not depend on momentum once the particle has reached the chambers.

Geometric and chamber efficiency can be evaluated with mu-pairs. A high statistics study has been carried out[25]. Fig. 3.5 shows the agreement between Monte Carlo and data muons from $e^+e^- \rightarrow \mu^+\mu^-$. The agreement in the barrel region of the detector is very good. For lower momentum muons the study found a systematic uncertainty of 2% for muon identification efficiency in the barrel. The systematic uncertainty for the end cap is estimated to be 5%.

3.4.4 Electron Identification

Electron identification (CEID) takes advantage of the superb energy resolution of the crystal calorimeter as well as specific ionization measurements (dE/dx) in the main drift chamber[27]. The CEID routine uses additional information such as shower shape and TOF in the barrel region.

Because electrons deposit most of their energy in the CsI calorimeter, electron tracks have a ratio of energy deposited in the calorimeter to momentum (E/P) near 1. All other charged particles (with the exception of anti-protons) leave relatively little energy and thus have an E/P ratio much less than one. See Fig 3.6 for a plot of E/P distribution for electrons.

The CEID code combines E/P and dE/dx information, along with additional information for tracks that pass through the barrel region, to produce the log-likelihood

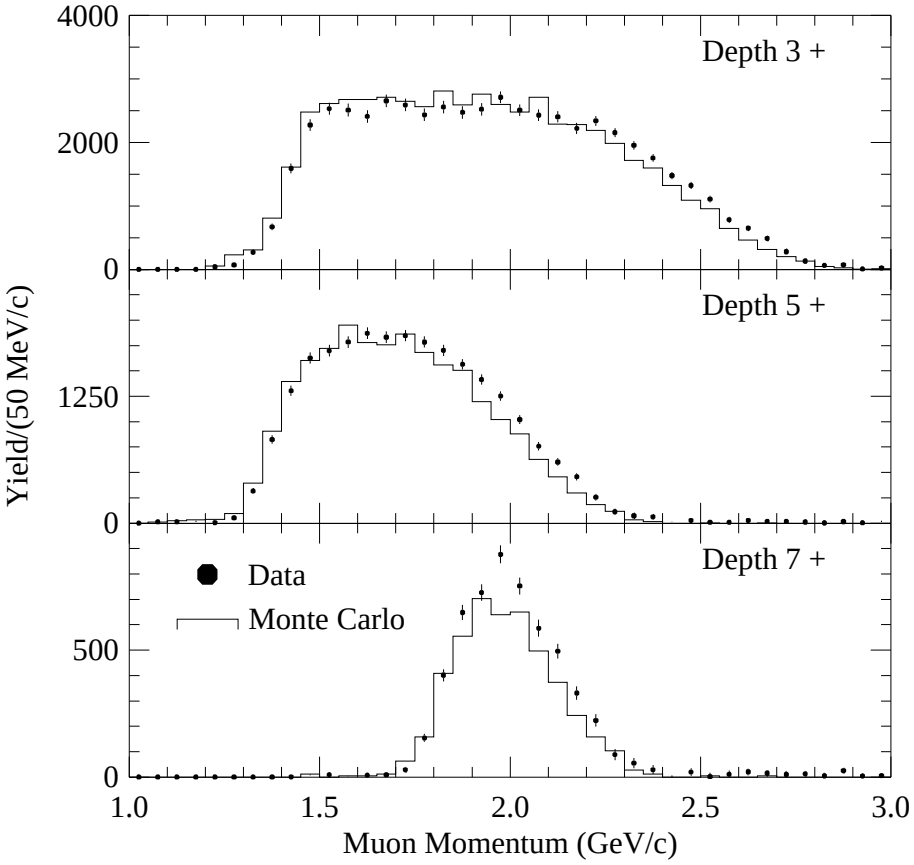

Figure 3.3: Comparison of Monte Carlo and data muon momentum spectra. The scales have been normalized to the same number of events. What is important here is the agreement where the efficiency begins to rise. This is a direct reflection of the amount of material in the detector and detector simulation. The shapes of the spectrum at higher momentum are sensitive to the proportions of specific final states in the Monte Carlo simulation ($D\ell\nu$, $D^*\ell\nu$, $D^{**}\ell\nu$), which are known to be imperfect.

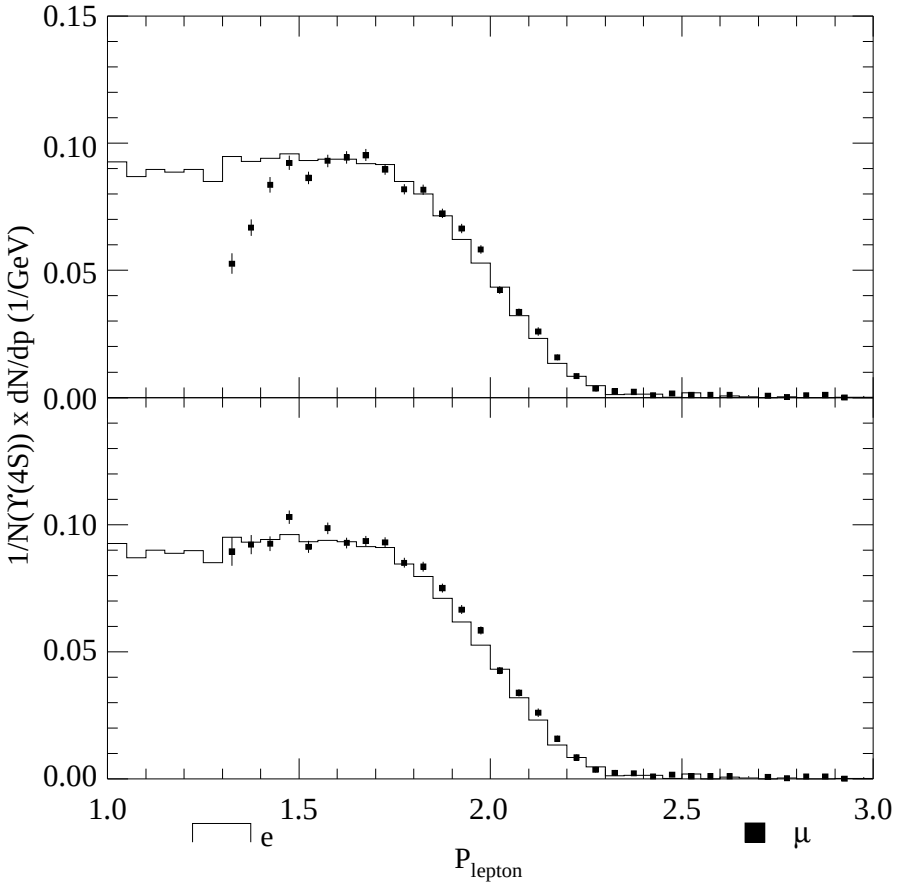

Figure 3.4: Comparison of yields of electrons and muons from semileptonic decays of B mesons. The yields are efficiency and fake corrected. Theoretically the two distributions should be almost identical. The difference between (a) and (b) is that the efficiencies used to correct the yields for the muons in (a) were from a Monte Carlo sample where there was a small amount of material missing from the detector description. In (b) the material is correct. The amount of material missing contributes about 23 MeV/c of additional momentum loss for a muon. When this is compared to the typical momentum of a muon that passes through 5 interaction lengths of material of about 1.5 GeV, one can see that the shape of the momentum spectrum is very sensitive to the amount of material in the detector. The agreement between the whole electron and muon spectrum above 1.3 GeV/c in (b) gives a measure of the systematic error on the electron efficiency.

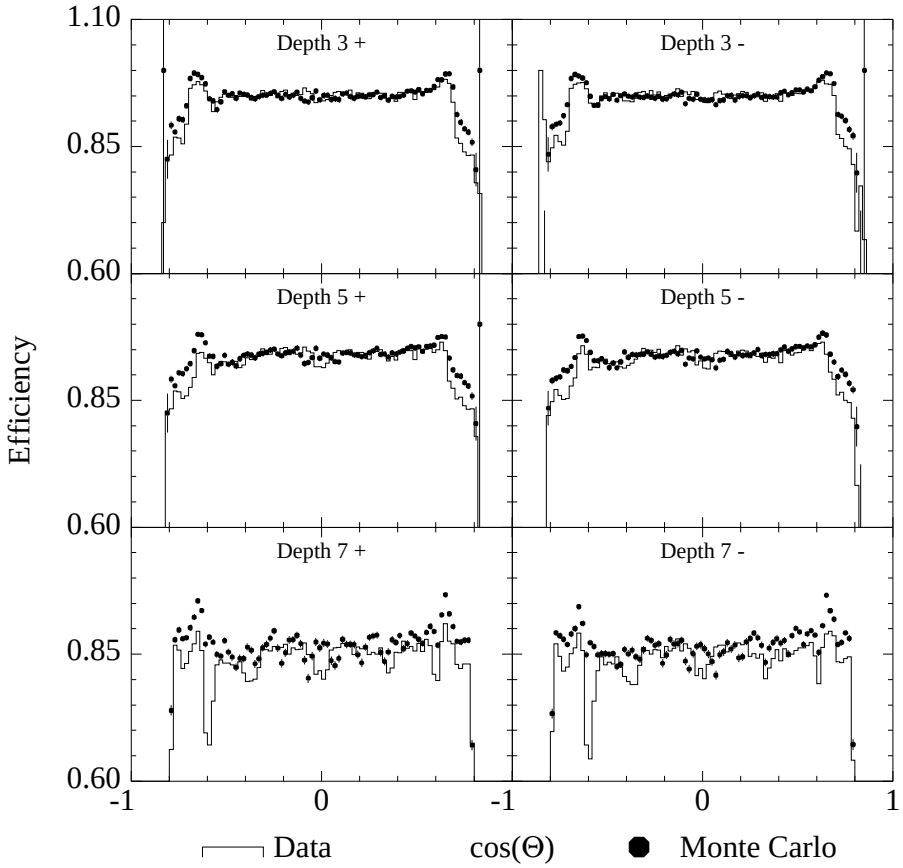

Figure 3.5: Comparison of efficiency between data and Monte Carlo for finding a 5.3 GeV/c momentum muon track at 3, 5 and 7 interaction lengths and for positive and negative charges.

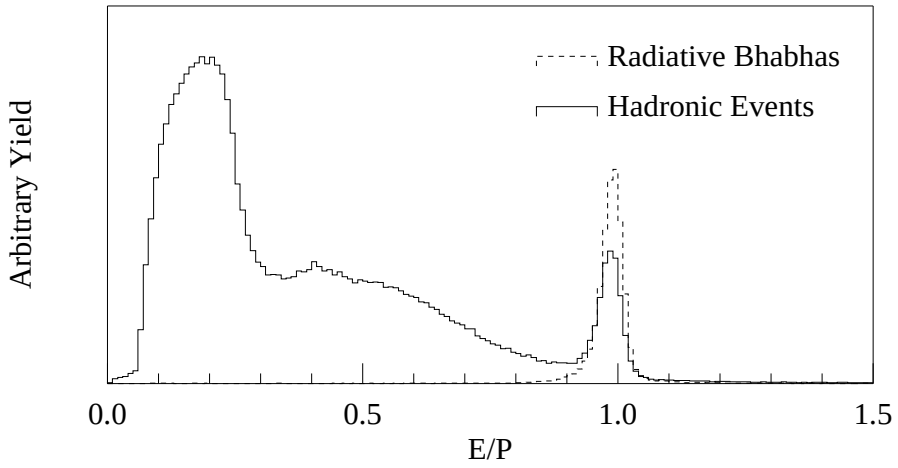

Figure 3.6: E/P for electrons from radiative Bhabha events compared to E/P for all charge tracks in hadronic events. The momentum of both sets of tracks was restricted to the range 0.8 to 3.0 GeV/c and the geometric region was restricted to the center part of the barrel.

(R2ELEC) of a particle being a true electron. The log-likelihood is defined by

$$\mathrm{R2ELEC} = \sum_{variables} \ln \frac{\mathrm{P_e}}{\mathrm{P_{\neq e}}}, \tag{3.6}$$

where $\mathrm{P_e}$ is the probability that an electron will produce a track with the values of the variables measured, and $\mathrm{P_{\neq e}}$ is the probability that a non-electron will produce the same values. The probabilities $\mathrm{P_e}$ were determined by embedding the hits produced by real electron tracks from radiative Bhabha events into hadronic events. The probabilities $\mathrm{P_{\neq e}}$ were determined from data taken at the Υ(1S) resonance. The Υ(1S) rarely produces electrons in its decay. If a variable could not be measured for a given track (say dE/dx information is missing) it is simply left out of the sum.

Unfortunately, not all the variables used in the CEID code are reproduced well with the Monte Carlo simulation. For this reason the value R2ELEC in Monte Carlo is not calculated as above. Instead, if the track is from an electron (for Monte Carlo we can peek at the track type), the R2ELEC value is randomly determined using the

electron distributions described above. Likewise, for a non-electron track, the non-electron probabilities are used.

While the authors of the CEID routine were careful in the design of the routine, they have a few concerns, mostly centered on how well the embedded electrons mimic electrons in real events. For this reason they will not quote a systematic error on how well the Monte Carlo predicts the electron efficiency of less than 5%. However, comparison of the efficiency and fake corrected semileptonic momentum spectra for electrons and muons (which should be theoretically almost identical) gives us confidence that the error on the efficiency of identifying electrons in the barrel region of the detector is reproduced within 3% (see Fig 3.4). Further studies have shown that the efficiency is reproduced within 2% in the barrel[20].

3.5 CLEO-II EVENT DISPLAY

Fig. 3.7 is an example of the CLEO-II event display. In the center are wire hits (dots) in the drift chambers overlaid with reconstructed tracks. The open squares in the center are hits in the end-cap crystals. The flat rectangles just outside the drift chamber represent hit barrel TOF counters. The closely spaced rings of rectangles present a view looking down the inside of the barrel calorimeter. Each rectangle represents a crystal. Filled rectangles represent crystals with hits. The inner circles of rectangles correspond to the far end of the barrel and the outer ones the near end. Outside the calorimeter are the barrel muon detectors, represented by trapezoids. The end-cap TOF and end-cap muon detectors are not shown in this picture (but can be shown if desired).

The event pictured is a candidate for $B^0 \rightarrow J/\psi \mathrm{K}^0$, where $J/\psi \rightarrow \mu^+\mu^-$ and $\mathrm{K}^0 \rightarrow \pi^+\pi^-$. The other high momentum track is identified as an e^- candidate. The muons are identified by the hits in the muon chambers. The K^0 is identified by the $\pi^+\pi^-$ vertex which is displaced slightly from the interaction point. The electron candidate is identified

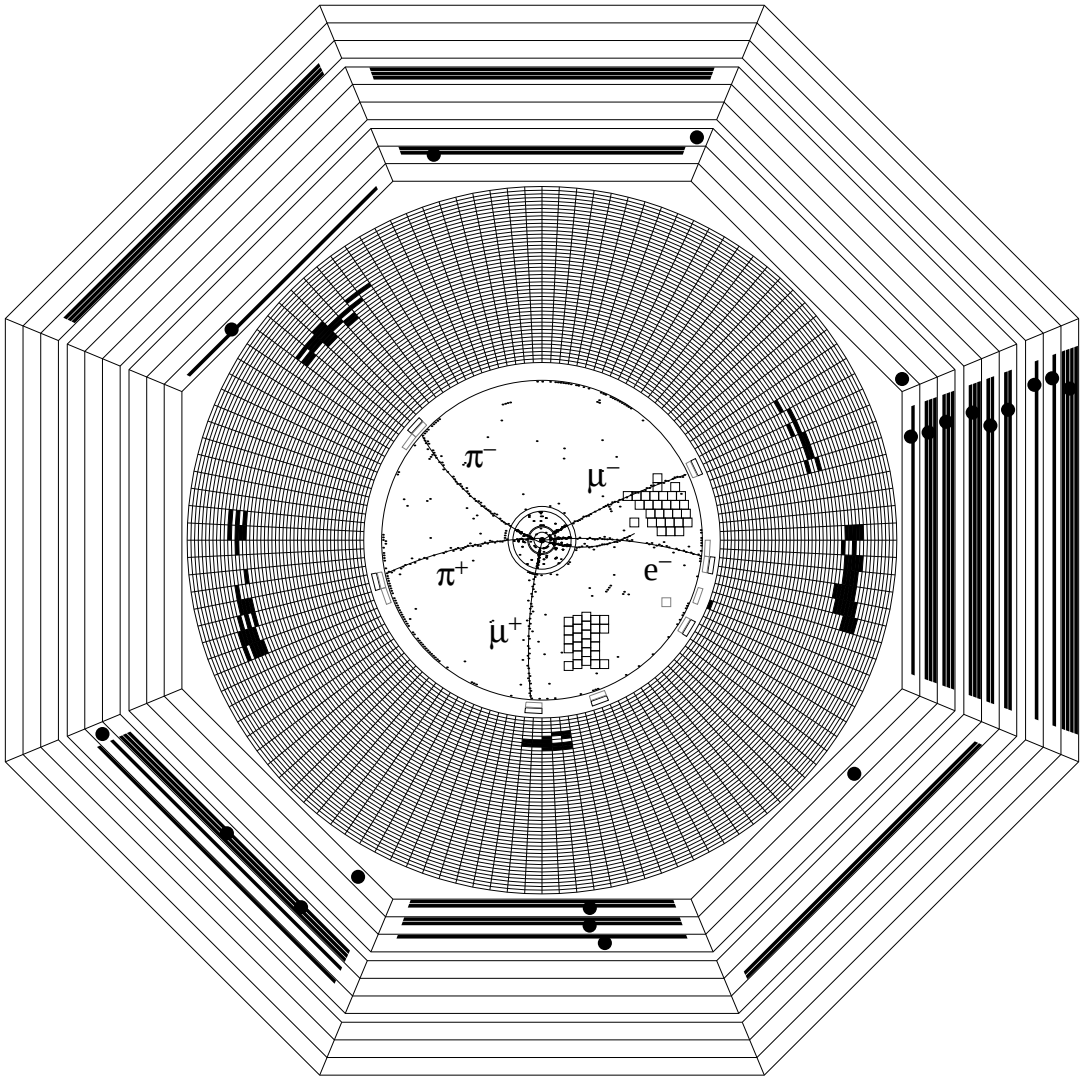

Figure 3.7: An example CLEO-II event display. See text for description.

principally by the match between the track momentum measured by the drift chamber and the energy of the corresponding shower in the calorimeter.

Chapter 4

ANALYSIS

The reduced $\Upsilon(4S)$ data produced by PASS2 (Chapter 3) is the starting point for all of our investigations of B-meson decay. In this chapter I describe analysis procedures which have been employed in extracting information about B-meson decays to charmonium mesons. After a brief introduction to the data set and event selection, the details of the analysis are presented in two sections. The first describes measurements of inclusive charmonium production in B-meson decay, for which we disregard the hadronization of the non-charm quarks. The second discusses exclusive measurements, where we completely reconstruct B mesons from their daughter particles, including a charmonium meson.

These measurements share much in common. The exclusive studies begin with the inclusive charmonium candidate events. This makes both analyses dependent on the reconstruction of J/ψ or ψ' candidates from two leptons. While the branching fraction for the decays of the J/ψ and ψ' to leptons are only 12% and 1.6% respectively, the very small backgrounds render very clean samples. As with all analyses, there are systematic and statistical limitations to the precision of these studies. In the case of inclusive decays to J/ψ the systematic uncertainties are more severe, and our data set has been used selectively. By sacrificing event samples and detector regions which are

less well understood, the overall precision of the measurement has been optimized. For all other measurements other than inclusive J/ψ, the systematic and statistical errors are comparable, or the limitation is from statistics, so our data sample has been fully used.

4.1 DATA SAMPLE AND EVENT SELECTION

The data used in this analysis were recorded between 1990 and 1993. An integrated luminosity of 2.02 fb^{-1} was accumulated at the Υ(4S) resonance, and an additional 0.99 fb^{-1} was collected at energies just below that resonance.[1] Because the $B \to J/\psi$ inclusive measurement is systematics limited, only the data for which the systematic uncertainties are best understood were used to study that decay mode (1.12 fb^{-1} of data taken at the Υ(4S) resonance and 0.53 fb^{-1} at energies just below).

Event-selection criteria were optimized for Υ(4S) events with B or $\overline{B}$ decays to charmonium. Events were required to have a reconstructed vertex consistent with the known interaction region,[2] and to have detected visible energy greater than 15% of the center-of-mass energy. We required at least five reconstructed charged tracks to suppress background from QED processes (such as $e^+e^- \to \tau^+\tau^-$, where the taus decay leptonically). To reduce background from non-resonant $q\overline{q}$ processes we required events to have a normalized Fox-Wolfram second order moment ($R_2 = H_2/H_0$) of less than 0.5[28]. We found $(2.15 \pm 0.04) \times 10^6$ $B\overline{B}$ events in the full sample which satisfied these

[1]The symbol "fb^{-1}" represents an inverse femtobarn, that is $(10^{-15}\text{barns})^{-1}$ or $(10^{-39}\text{cm}^2)^{-1}$. A "barn" is defined as 10^{-24}cm^2. The probability of a particle interacting as it passes through matter (or a bunch of particles circulating the opposite direction in a collider) is proportional to its effective "area" or "cross section." If a particle's cross section is one barn then with an integrated luminosity of one inverse barn one would expect one collision to take place. The effective area for an electron colliding with a positron at the Υ(4S) resonance is approximately 4 nb, of which non-resonant processes contribute 3 nb and $B\overline{B}$ production contributes 1 nb. Thus in 1 fb^{-1} of data one expects roughly a million $B\overline{B}$ events.

[2]Events that have a vertex outside the interaction region are likely to be from interactions of stray electrons or positrons with the beam pipe, or with the residual gas in the beam pipe.

requirements, and $(1.19 \pm 0.02) \times 10^6$ in the smaller sample used to study $B \to J/\psi$X. The largest contribution to the error is the variation in the cross section within each data set.

4.2 INCLUSIVE MEASUREMENTS

4.2.1 Selection of J/ψ and ψ' Candidates

The first step in finding events with charmonium is to find dilepton pairs that may have come from J/ψ's or ψ''s. The J/ψ candidates found this way were also used to look for ψ', where the ψ' decayed to $J/\psi\pi^+\pi^-$, and for χ_c, where the χ_c decayed to $J/\psi\gamma$. In all cases, the maximum momentum of the $J/\psi(\psi')$ state from a B-meson decay is less than 2 GeV/c (1.65 GeV/c). (The maximum momentum occurs for the Cabibbo-suppressed decay $B \to J/\psi(\psi')\pi$.) To reduce continuum background we reject J/ψ and ψ' candidates with momenta greater than the maximum. Slow-moving charmonium states which decay leptonically very rarely produce leptons of momentum less than 0.8 GeV/c. Hence, to suppress combinatorial backgrounds, we demanded that both leptons have momenta above 0.8 GeV/c.

For the inclusive $B \to J/\psi$ measurement we required both electron candidates to project into the region of the calorimeter with the best energy resolution ($|\cos(\theta)| < 0.7$, where θ is the polar angle with respect to the beam direction). For other inclusive measurements we allowed one electron to be in the expanded angular range $|\cos(\theta)| < 0.91$. The tighter requirement for J/ψ candidates was chosen because the measurement of the branching fraction for that mode is limited by systematic uncertainties rather than statistics, and the efficiency for identifying electrons is better known in the central part of the calorimeter than at the ends. The statistical and systematic errors are comparable for the inclusive $B \to \psi'$ and $B \to \chi_c$ modes.

For dimuons, at least one of the muons was required to have penetrated five nuclear

interaction lengths, while the other was required to have penetrated three. This choice maximizes the signal, as at least one of the muons always has a momentum greater than 1.5 Gev/c, sufficient to penetrate to the depth 5 muon counters, while the other muon has a momentum of less than 1.5 GeV/c and a small efficiency for reaching the depth 5 counters.

4.2.2 $B \to J/\psi \mathbf{X}$

Branching Fraction for $B \to J/\psi \mathbf{X}$

The dileptons candidates were combined to calculate the invariant mass of the hypothetical parent particle. Histograms of the invariant mass distributions for (a) dielectrons and (b) dimuons are shown in Fig. 4.1. The background functions for both fits are second-order polynomials. The J/ψ signals were fitted to histograms derived from a Monte Carlo simulation of $B \to J/\psi$X, $J/\psi \to e^+ e^-$ or $\mu^+ \mu^-$. Since the J/ψ detection efficiency is somewhat sensitive to the J/ψ momentum, these Monte Carlo events were generated using an iterative procedure to approximate the observed momentum spectrum in data. This simulation included the effects of bremsstrahlung in the detector material and of final state electromagnetic radiation in the J/ψ decay[29]. Fig. 4.2 shows the dielectron and dimuon mass distributions, generated with and without final-state radiation. Approximately 6% of the detected dimuon and 35% of the detected dielectron J/ψ's have masses between 2.50 and 3.05 GeV/c^2, more than 3σ below the J/ψ mass.

A check was made using the Crystal Ball function[30] of how well the mass and width of the J/ψ mass peak agreed between Monte Carlo and data. The Crystal Ball function fits the J/ψ line shape very well (confidence levels of 64% and 33% for dielectron and dimuon data respectively). For dielectrons, the J/ψ mass was 2.3$\pm$0.8 MeV/c^2 lower in Monte Carlo than in data (3088.2 vs. 3090.7 MeV/c^2). The widths of the signals agreed (15.1 vs. 15.2 MeV/c^2). For dimuons, the Monte Carlo mass

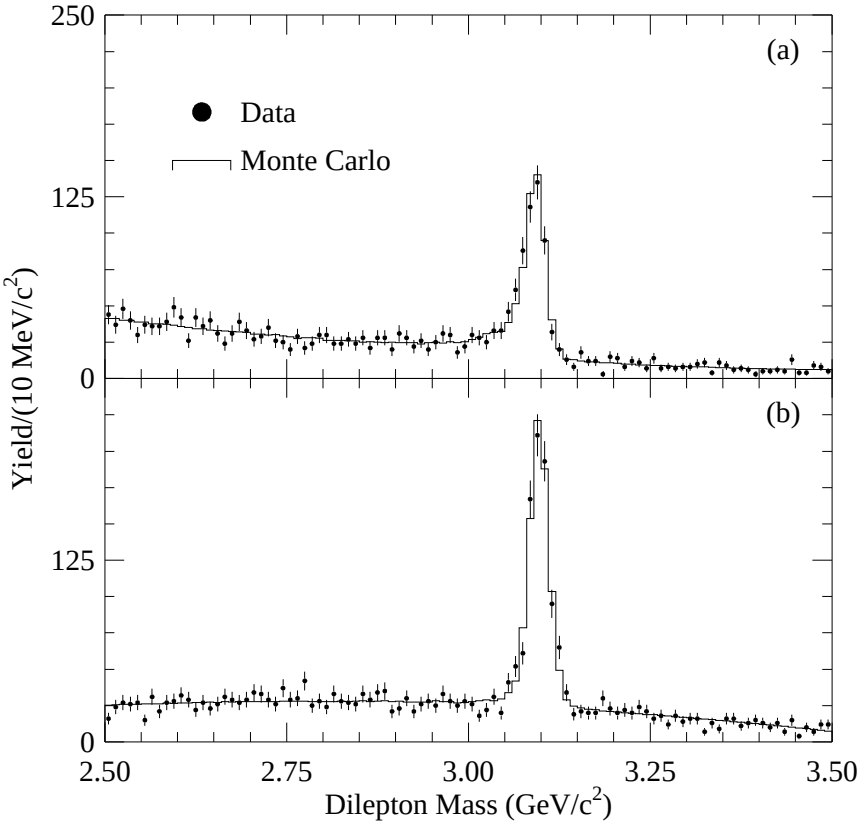

Figure 4.1: Mass distributions for (a) dielectron and (b) dimuon modes from B decays. The fits are to Monte Carlo signal line shapes for $\psi \to \ell^+\ell^-$ and polynomial backgrounds.

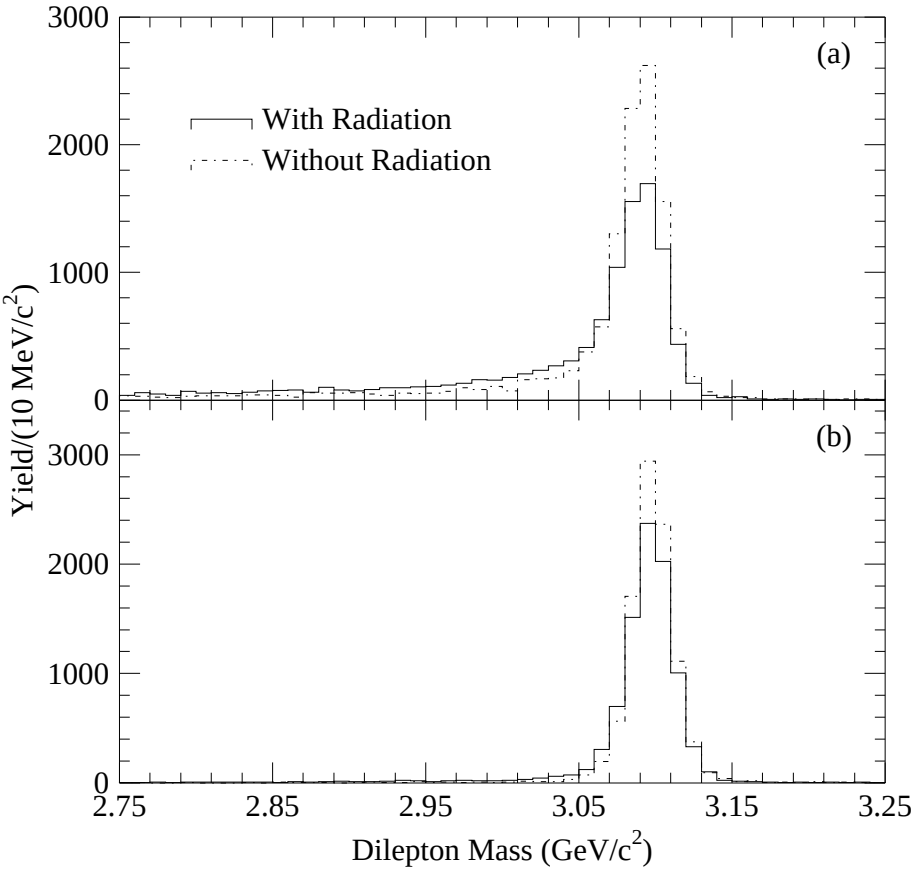

Figure 4.2: Monte Carlo line shapes for $\psi \rightarrow \ell^+\ell^-$ with and without final-state radiation, (a) dielectrons and (b) dimuons. The effect of bremsstrahlung is included in all line shapes.

was low by 0.5±0.6 MeV/c^2 (3097.3 vs. 3097.8 MeV/c^2). The dimuon Monte Carlo width was a bit narrower than in data (13.4 vs. 14.1 MeV/c^2). The dielectron mass was shifted in the Monte Carlo histogram to agree with data. The dimuon mass in the Monte Carlo histogram had a small random value added for each event to adjust the width to match that of data. The systematic errors in the measured yields introduced by the uncertainty in the position of the mass peaks and widths are small compared to other systematic errors (less that 0.5% for the mass peak and 1.0% for the width).

The results of the fits to the dilepton mass distributions in Fig. 4.1 are signals for $B \to J/\psi$X of 741±37 events in the dielectron mode, and 748±32 events in the dimuon mode, where the errors are statistical only. The confidence levels of the fits were 73% for the dielectron mode and 52% for the dimuon mode.

Charmonium is also produced through non-resonant processes[31]. A clear signal is seen in the larger (0.99 fb^{-1}) continuum data sample, and also in the larger (2.02 fb^{-1}) resonant data sample when the momentum of the J/ψ candidate is required to be above 2 GeV/c (see Fig. 4.3). There is not a statistically significant excess in the non-resonant data sample for J/ψ candidates with momentum less than 2 GeV/c (Fig. 4.4), but we must still subtract the observed non-resonant J/ψ yield from the signal. In the continuum sample of 0.53 fb^{-1}, corresponding to the 1.12 fb^{-1} Υ(4S) sample used for $B \to J/\psi$X, we found 8.8±5.3 dielectrons and 7.3±5.0 dimuons. These yields must be scaled by 2.12±0.01, which is the ratio of the integrated luminosities of the samples after correction for the energy dependence of the continuum cross section. The resulting continuum corrections applied to the Υ(4S) J/ψ yields are 18.7±11.3 dielectrons and 15.4±10.5 dimuons.

The efficiencies for detecting dielectron and dimuon J/ψ decays with dilepton masses between 2.5 and 3.5 GeV/c^2 were determined from the Monte Carlo simulation to be (45.3±0.4)% and (46.4±0.4)%, respectively, where the errors are due to the statistics of the Monte Carlo sample. The efficiency for detecting dimuon J/ψ decays is constant

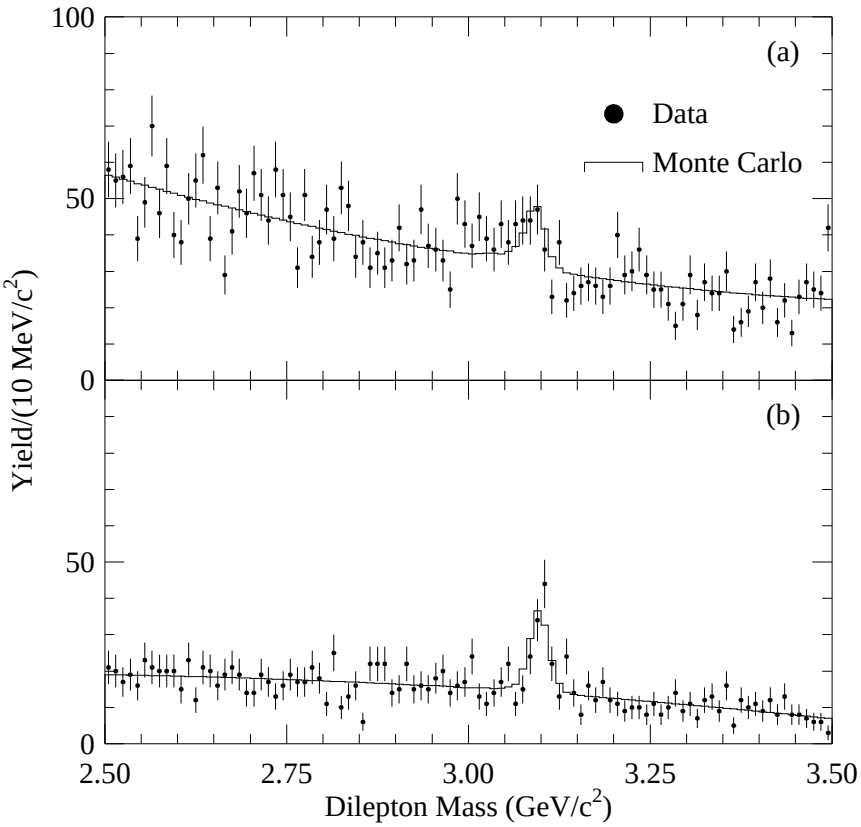

Figure 4.3: Mass distributions for the continuum data sample and for dileptons with momentum above 2 GeV/c in the on resonance data sample; (a) dielectrons and (b) dimuons. The fits are to Monte Carlo signal line shapes for $J/\psi \to \ell^+\ell^-$ and polynomial backgrounds.

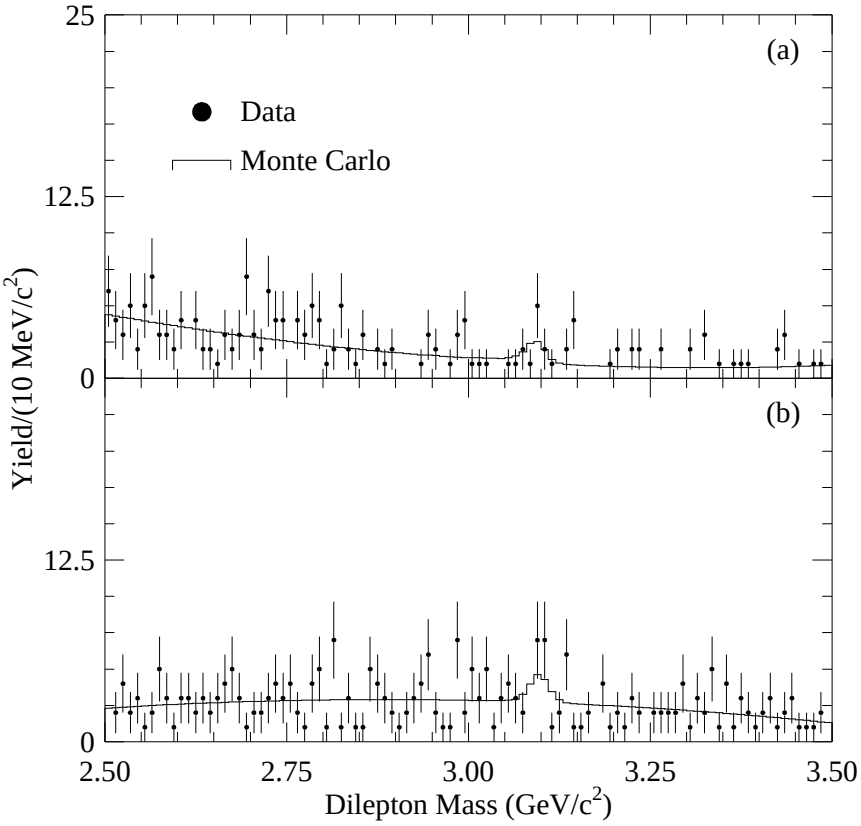

Figure 4.4: Mass distributions from the continuum data sample for (a) dielectrons and (b) dimuons. The dilepton momentum was required to be be less than 2 GeV/c, and the Fox-Wolfram parameter R_2 was required to be less than 0.5. The fits are to Monte Carlo signal line shapes for $\psi \to \ell^+\ell^-$ and polynomial backgrounds.

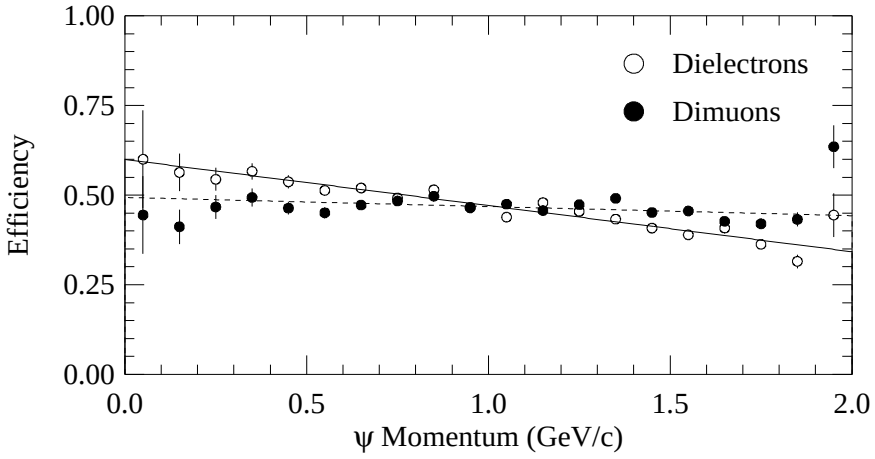

Figure 4.5: Efficiency as a function of momentum for J/ψ's decaying to electrons and muons.

over the J/ψ momentum range of interest (see Fig. 4.5). The efficiency for dielectron J/ψ's decreases with increasing J/ψ momentum as a result of limiting the electrons to the central part of the detector. Slowly moving J/ψ's that decay leptonically produce nearly back-to-back lepton pairs, so if one lepton passes through the barrel region of the detector, the other one is also likely to do so. Leptons from a fast moving J/ψ will be boosted in the direction of the J/ψ, so if one lepton passes through the barrel the other may not. The efficiency for detecting dielectron J/ψ's is independent of momentum when one electron is allowed to be in the end-cap region of the detector. The systematic error introduced by the change in efficiency over the momentum region of interest and the uncertainty in matching the Monte Carlo and data spectra is 2% for the dielectrons and much smaller than 1% for the dimuons. This was checked by weighting the Monte Carlo derived efficiency for each momentum bin by the number of events in each bin.

Using the MARK III[32] values of 5.92±0.25% and 5.90±0.25% for the branching ratios for J/ψ decays to dielectrons and dimuons, we found the branching fraction for $B \rightarrow J/\psi$X to be (1.14±0.06)% using dielectrons and (1.13±0.05)% using dimuons, where the errors are statistical only. These values are in good agreement.

Uncorrelated	e^+e^-	$\mu^+\mu^-$
Branching fraction	4.2%	4.1%
Monte Carlo statistics	0.9%	0.9%
Monte Carlo momentum	2.0%	—
Monte Carlo line shape	1.0%	1.0%
Lepton ID	4.0%	4.7%
Total	6.3%	6.4%
Correlated		
Tracking	2.0%	
Number of B mesons	1.6%	
R_2 Distribution	2.0%	
Total	3.2%	

Table 4.1: Contributions to the systematic uncertainty in the $B \to J/\psi$X branching fraction measurement.

Systematic uncertainties dominate the error on the inclusive B to J/ψ measurement. Significant uncertainties are associated with the lepton identification efficiencies and the J/ψ to dilepton branching fractions. The first of these errors enter twice, once for each lepton. Other smaller errors include those associated with Monte Carlo statistics, the Monte Carlo momentum distribution (through the momentum-dependent efficiency), the Monte Carlo line shape used in the fit, the tracking efficiency, the number of B mesons in the data sample, and the efficiency of the requirement $R_2 < 0.5$. A summary of the systematic errors is given in Table 4.1.

The $B \to J/\psi$X branching fractions measured with dimuon and dielectron events were combined with weights determined from the statistical and uncorrelated systematic errors. The combined branching fraction for $B \to J/\psi$X is $(1.13 \pm 0.04 \pm 0.06)\%$, where the first error is statistical and the second systematic and the "B" represents the mix of B^0 and B^+ in Υ(4S) decays (we expect the number of B^0's and B^+'s to be roughly equal because of the very small mass difference between the two mesons). This can be compared to the Particle Data Group value of $(1.12 \pm 0.16)\%$[1], which increases to $(1.31 \pm 0.19)\%$ if the new MARK III numbers for $J/\psi \to \ell^+\ell^-$ are used. The new result is a large improvement in precision over the previous world average.

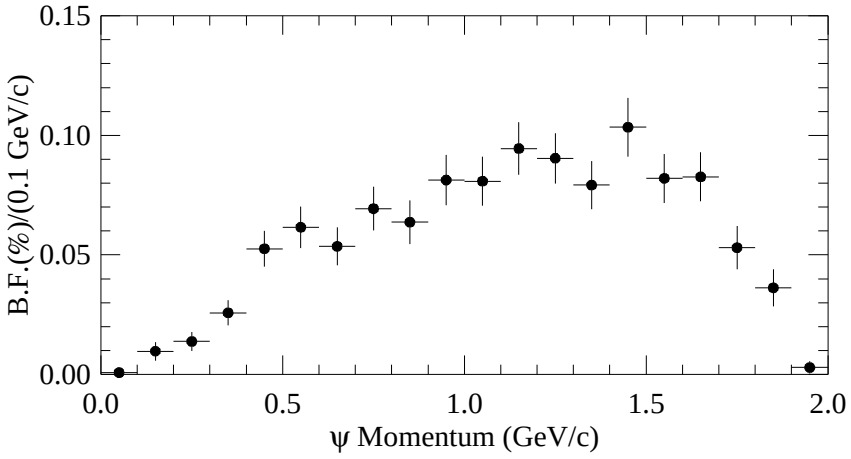

Figure 4.6: Momentum spectrum for inclusive J/ψ production from B decays.

Properties of J/ψ's From B Decay

The momentum spectrum of the inclusive J/ψ's was measured by dividing the data sample into 100 MeV/c bins between 0 and 2 GeV/c. Each of the resulting dielectron and dimuon mass distributions was fitted to determine the J/ψ yield in that bin and then corrected for that bin's efficiency. The resulting momentum distribution is shown in Fig. 4.6. The distribution is discussed in Chapter 5.

The R_2 (second order Fox-Wolfram moment)[28] distribution for $B\overline{B}$ events that include a J/ψ is shown in Fig. 4.7. The distribution was measured by dividing the data sample into 10 R_2 bins and fitting each bin separately. Plotted in the same figure are the expected distributions for generic $B\overline{B}$ events and non-resonant (continuum) events. The R_2 distribution for $B\overline{B}$ events that include a J/ψ falls between the generic $B\overline{B}$ and non-resonant distributions. This is expected because a J/ψ tends to decay with two rather energetic leptons back to back and thus a $B\overline{B}$ event with a J/ψ is less spherical than a generic $B\overline{B}$ event. This is borne out by comparing the distribution of R_2 for $B\overline{B}$ events with a J/ψ to that of $B\overline{B}$ Monte Carlo with a J/ψ (Fig. 4.8). We see good agreement between the data and Monte Carlo. There is a 2% discrepancy between data

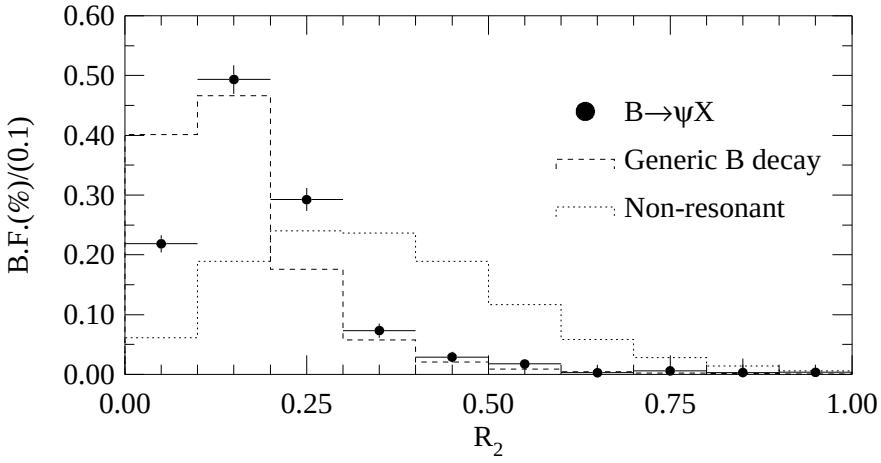

Figure 4.7: The Fox-Wolfram second order moment (R_2) from data for events including the decay $B \to J/\psi X$ and from Monte Carlo for a sample of generic B-meson events and a sample of non-resonant events.

and Monte Carlo in the amount of the distribution that is above $R_2 = 0.5$. We take this as a systematic error.

Consistency Between Data Sets

The data used in this thesis can be divided into sets based on changes in either the accelerator or detector configurations. There are eight standard sets. The first four are used for the measurement of the inclusive $B \to J/\psi X$ branching fraction and the momentum and R_2 spectra of that decay. All eight are used for the rest of the measurements. This is because we have had time to study the systematic errors associated with the older data sets better. It is useful to check the consistency of the $B \to J/\psi X$ branching fraction between the data sets as evidence that there are no significant changes that would effect the measurements made with the entire data set. Table 4.2 shows the measured branching fraction by data set, uncorrected for non-$B\overline{B}$ contributions. The branching fractions are in good agreement within the statistical errors. The branching fraction for $B \to J/\psi X$, corrected for contributions from non-$B\overline{B}$ decay, for the entire data set is

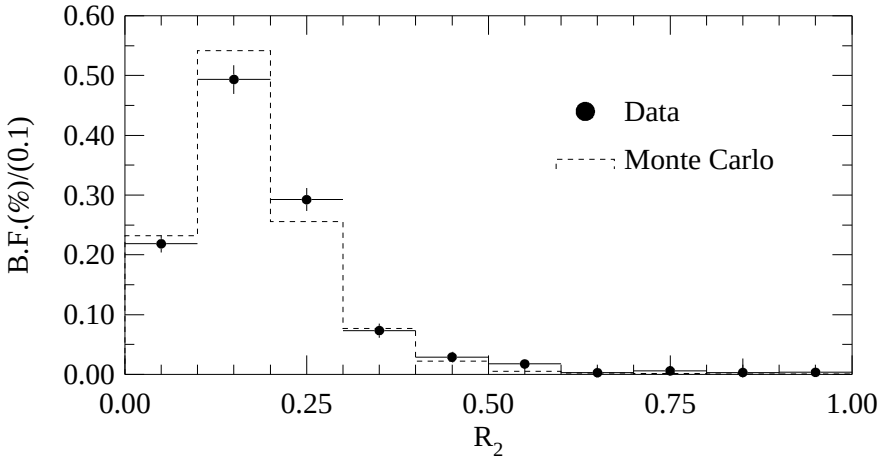

Figure 4.8: The Fox-Wolfram second order moment (R_2) for data and Monte Carlo for the decay $B \to J/\psi X$.

one statistical standard deviation lower than that measured using the smaller part of the data set. This introduces a systematic error in branching fractions measured with the entire data set that is small compared to other systematic uncertainties.

4.2.3 $B \to \psi' X$

We have measured B-meson decays to ψ' using two decay channels. The analysis based on the dilepton decay $\psi' \to \ell^+\ell^-$ is very similar to the J/ψ study, but is hampered by

Data Set	Number of B's	e^+e^-	$\mu^+\mu^-$
4S1	21211	2.10±0.57	1.29±0.39
4S2	497852	1.19±0.09	1.12±0.08
4S3	442800	1.11±0.10	1.13±0.08
4S4	229781	1.11±0.13	1.23±0.12
4S5	231140	1.11±0.13	1.10±0.11
4S6	247514	1.08±0.13	0.94±0.10
4S7	288969	1.14±0.12	1.08±0.10
4S8	200207	0.81±0.12	1.21±0.13

Table 4.2: $B \to J/\psi X$ branching fractions by data set, uncorrected for non-$B\overline{B}$ contributions. The error is statistical only.

a much smaller leptonic branching fraction. A second analysis, based on the hadronic transition $\psi' \to J/\psi \pi^+ \pi^-$ followed by the leptonic decay of J/ψ, provides an independent measurement with different systematic considerations. In the following sections we describe these measurements separately, and conclude with a brief description of how they have been combined.

$\psi' \to \ell^+ \ell^-$

The distributions of dielectron and dimuon invariant masses in the ψ' region are shown in Fig. 4.9, both separately and combined. We determined the ψ' yield by fitting the separate distributions with Monte Carlo signal shapes and polynomial backgrounds. We found signals of 68 ± 17 dielectrons and 59 ± 13 dimuons, where the errors are statistical only. The confidence level for the dielectron mode was 93% and for the dimuon mode 79%. The efficiency for detecting the ψ' is 59% in both the dielectron and dimuon modes, significantly higher than the corresponding efficiencies for J/ψ. The higher dielectron efficiency results from using the end-cap region of the calorimeter. The higher dimuon efficiency is a consequence of the greater momentum of muons from ψ' decay, which allows a higher fraction to penetrate the iron absorber.

Using the Particle Data Group[1] branching fractions for $\psi' \to e^+ e^-$ and $\psi' \to \mu^+ \mu^-$ of $(0.88 \pm 0.13)\%$ and $(0.77 \pm 0.17)\%$, respectively, we find branching fractions for $B \to \psi' \mathrm{X}$ of $(0.31 \pm 0.08)\%$ and $(0.30 \pm 0.07)\%$. The sources of systematic uncertainty are the same as for the J/ψ, except that the error on the ψ' to dilepton branching fraction is much larger (15% for $\psi' \to e^+ e^-$ and 22% for $\psi' \to \mu^+ \mu^-$), and dominates the systematic error. The error in the efficiency for identifying both electrons increases from 4% to 6% as a result of using the end-cap region of the detector. We have combined the two modes with weights given by the statistical and uncorrelated systematic errors. The resulting branching fraction for $B \to \psi' \mathrm{X}$ is $(0.30 \pm 0.05 \pm 0.04)\%$.

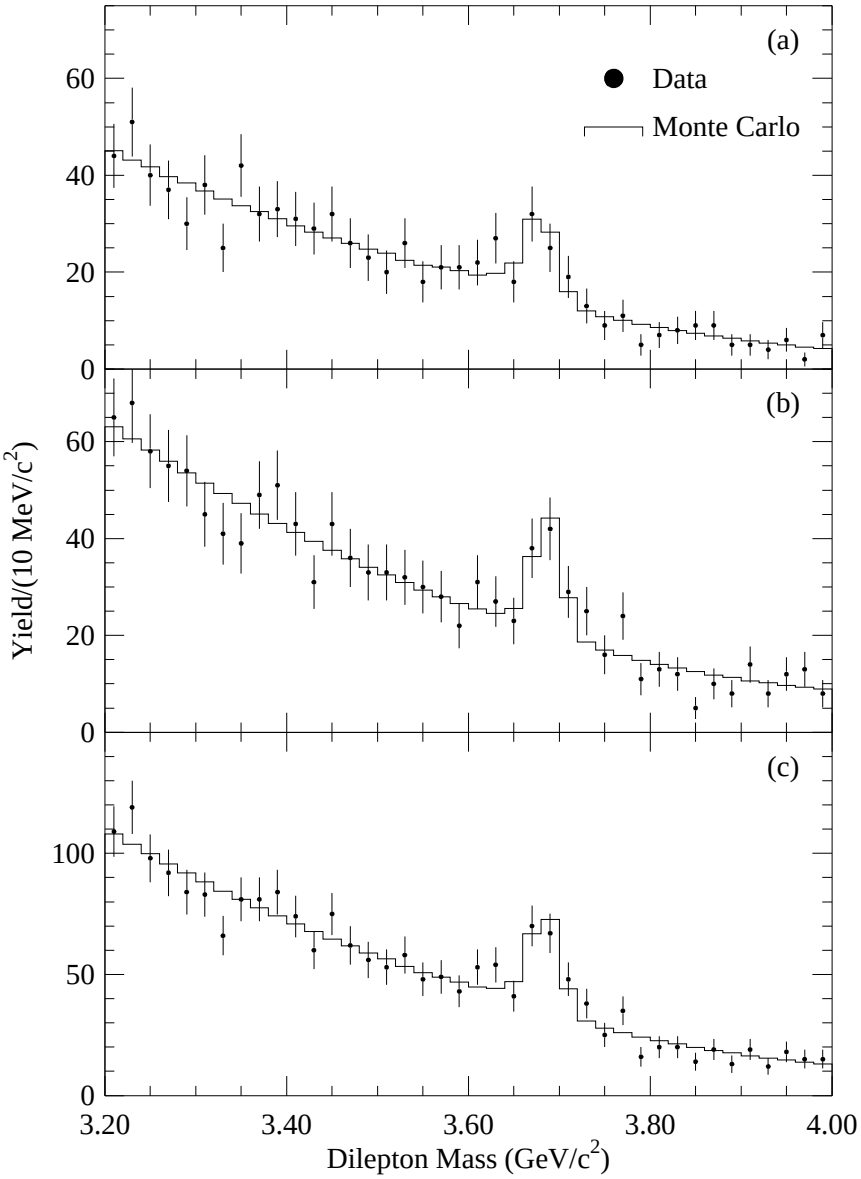

Figure 4.9: Dilepton mass distributions for (a) dielectrons, (b) dimuons, and (c) the sum of dielectrons and dimuons. The fits are to a Monte Carlo signal line shape for the process $B \to \psi' X$, $\psi' \to e^+e^-$ or $\psi' \to \mu^+\mu^-$, and a polynomial background.

$\psi' \to J/\psi \pi^+ \pi^-$

A second, statistically independent, measurement of the $B \to \psi'$X branching fraction has been made using the decay chain $\psi' \to J/\psi \pi^+ \pi^-$, $J/\psi \to \ell^+ \ell^-$. The product branching fraction for this process (32.4% for $\psi' \to J/\psi \pi^+ \pi^-$[1], 11.8% for $J/\psi \to \ell^+ \ell^-$) is roughly a factor of 2 greater than the $\psi' \to \ell^+ \ell^-$ branching fraction. This advantage is diminished by the inefficiencies involved in reconstructing the two charged pions. The overall efficiency for detecting ψ' mesons in this channel is comparable to that of the dilepton measurement.

To search for ψ' decays in this mode we first selected events where the J/ψ candidates had an invariant mass within two standard deviations (σ = 15 MeV) of the measured J/ψ mass. The width of the J/ψ was determined by fitting the data to the Crystal Ball function[30], which provides an adequate description of the radiative tail. The efficiency for J/ψ's that pass the mass criterion (including tracking and lepton identification) is 35% for dielectrons and 41% for dimuons. Note that we allowed the second electron in the J/ψ candidate to be outside the central region of the detector.

Pion candidates were required to have ionization rates within three standard deviations of the expected value. Tracks that were identified as daughters of a K^0_S were vetoed. It has been shown that the $\pi^+\pi^-$ invariant mass spectrum from ψ' decays favors larger values than would be expected from phase space (Fig. 4.10)[32]. We required the invariant mass of the dipion system to be between 0.45 and 0.58 GeV/c^2. This cut has an efficiency of (86$\pm$5)% while rejecting over half of all random dipions.

In Fig. 4.11 we present the distributions of the difference between the masses of reconstructed ψ' and J/ψ candidates for dielectrons, dimuons and both combined. Using the mass difference reduces the effect of the error in the J/ψ mass measurement. The data were fitted to a second order polynomial with a Monte Carlo signal shape. We found signals of 48$\pm$10 in the dielectron channel and 65$\pm$12 in the dimuon channel, where the errors are statistical only. The confidence levels of the fits were 6% and

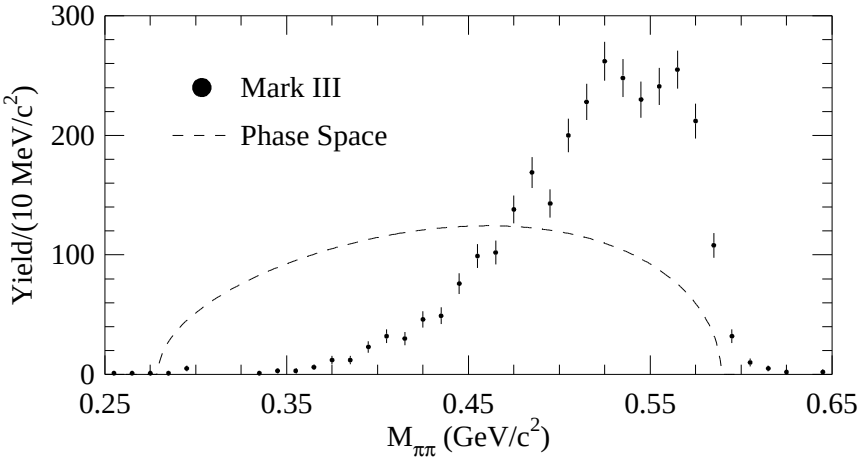

Figure 4.10: Dipion mass distribution for the decay $\psi' \to J/\psi\pi^+\pi^-$. The dashed line is for the spectrum expected from phase space while the points are the spectrum measured by Mark III.

42%, respectively. The efficiency for finding $\psi' \to J/\psi\pi^+\pi^-$ in the dielectron mode is 17%, while for the dimuon mode it is 20%. We find branching fractions for $B \to \psi'$X of (0.35 ± 0.08)% for the dielectron mode and (0.40 ± 0.07)% for the dimuon mode. The sources of systematic uncertainty include those for the $B \to J/\psi$X measurement as well as a 2% error in the efficiency for finding each pion track, a 2% error in the efficiency for identification for each pion, a 6% error in the efficiency of the dipion mass requirement, and an 8% error in the $\psi' \to J/\psi\pi^+\pi^-$ branching fraction. For the dielectron mode, the error in the efficiency for identifying both leptons is 6%, since we include the end-cap region of the detector.

The dielectron and dimuon modes have been combined, weighted by the statistical and uncorrelated systematic errors, to give a B to ψ' inclusive branching fraction of $(0.38\pm0.05\pm0.05)$%.

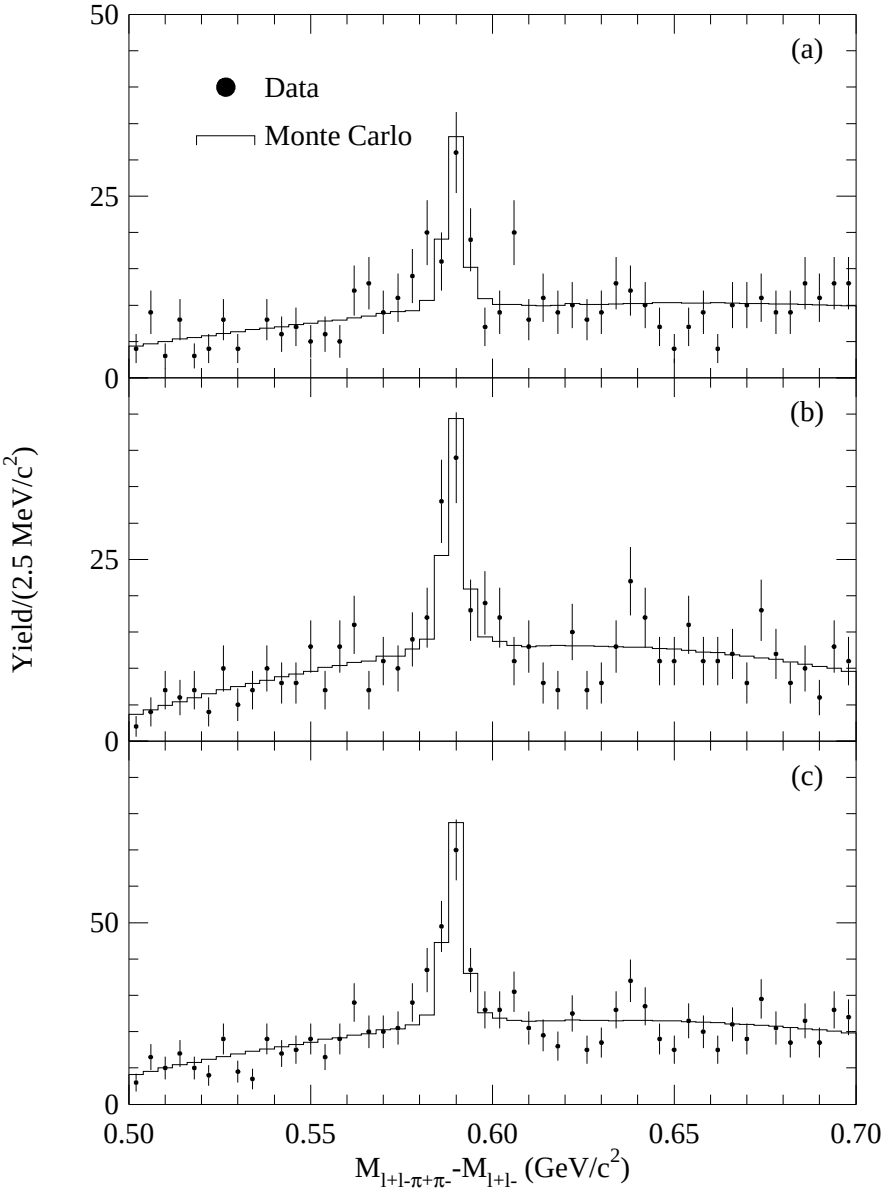

Figure 4.11: Distributions of the difference between the $\ell^+\ell^-\pi^+\pi^-$ and $\ell^+\ell^-$ masses for (a) dielectrons, (b) dimuons, and (c) the sum of dielectrons and dimuons. The fit is to a Monte Carlo signal line shape from the $\psi' \to J/\psi\pi^+\pi^-$ signal and a polynomial background.

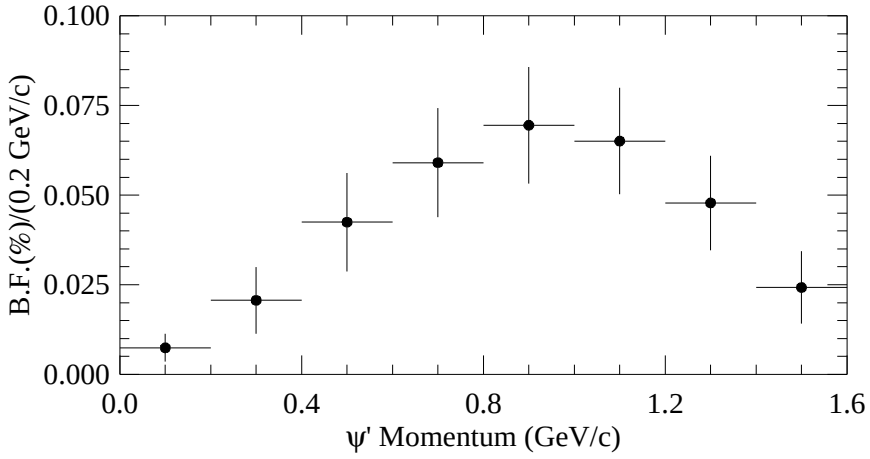

Figure 4.12: Momentum spectrum for inclusive ψ' production from B decays.

Combining the Two $B \to \psi' X$ Modes

Our two measurements of the branching fraction for $B \to \psi' X$ are in good agreement. Since the samples are statistically independent they can be combined into a single result. Using relative weights determined from the statistical and uncorrelated systematic errors, we find the branching fraction for $B \to \psi' X$ to be $(0.34 \pm 0.04 \pm 0.03)\%$.

The momentum distribution of the ψ''s is shown in Fig. 4.12. The momentum spectrum was obtained by fitting the data split into eight momentum bins for each mode separately. The momenta spectrum for the two modes were combined with the same weights as used for combining the two branching fractions. As in the case of direct J/ψ production, the observed shape suggests a sizable contribution from higher K^* resonances or nonresonant multiparticle final states.

4.2.4 $B \to \chi_c X$

Inclusive χ_c events were reconstructed by combining photons detected in the cesium iodide calorimeter with any accompanying J/ψ candidates. The distribution of the mass difference between the χ_c and J/ψ candidates was fitted to the distribution expected

for the decay chain $B \to \chi_c X$, $\chi_c \to J/\psi\gamma$, $J/\psi \to \ell^+\ell^-$. We demanded the mass of the J/ψ candidate for the χ_c search to be within two standard deviations of the nominal J/ψ mass, just as was done for the $\psi' \to J/\psi\pi^+\pi^-$ search.

Selection of Photon Candidates

We selected photon candidates from showers in the cesium iodide calorimeter with energies of at least 75 MeV. We rejected shower that were matched to charged tracks or were in the region of the end-cap calorimeter with inferior resolution.

The largest background to the χ_c signal is due to random combinations of photons from π^0's with correctly reconstructed J/ψ's from B-meson decays. Monte Carlo studies showed that the statistical significance of the $B \to \chi_c X$ measurement is optimized by rejection of these photons. Therefore any candidate photon which could be combined with another photon to produce an effective mass near the π^0 mass was rejected. The Monte Carlo studies revealed that signal photons were occasionally vetoed when they were combined with a low-energy photon from an uncorrelated π^0. The reduction of this effect was the primary motivation for the 75 MeV energy cut. If the invariant mass of a photon pair was within a range of -5 to 3 standard deviations of the measured π^0 mass, the photons were flagged as being part of a π^0 and were not used. The width of the π^0 peak was determined by fitting the π^0 mass plot (Fig. 4.13) for different momentum intervals with the Crystal Ball function[30]. This function adequately describes the long tail on the lower side, which results from photon energy leaking out of the crystals and the shower energy being underestimated.

Further selection criteria were imposed on the remaining showers. We required showers to be in the central region of the calorimeter ($|\cos\theta| < 0.7$), and to have a shape consistent with that expected for a photon. Finally, we rejected showers that were within 9° downstream of the intersection of a charged track with the crystals, eliminating the debris from charged particle interactions.

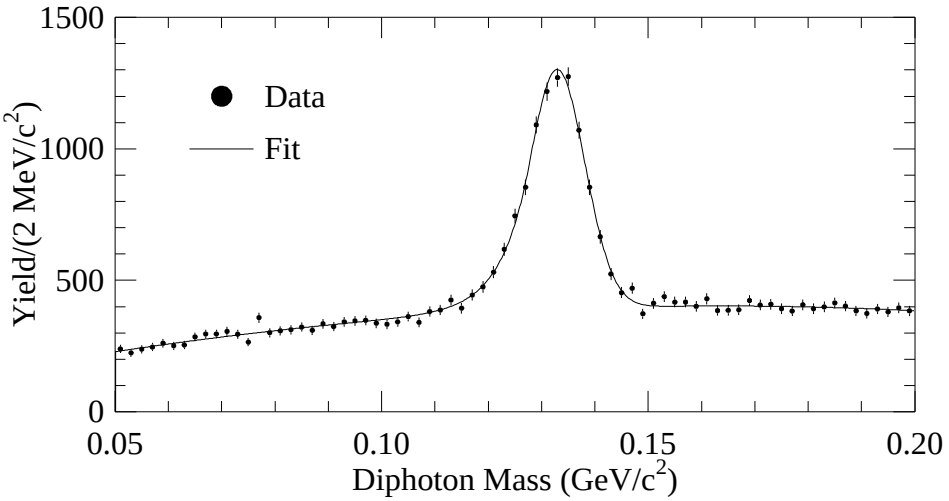

Figure 4.13: Mass spectrum for diphotons with momenta between 0.4 and 0.8 GeV/c^2. Both photon candidates were required to be in the barrel region of the calorimeter. The fit to the signal is with the Crystal Ball function.

Monte Carlo studies showed that the remaining background photons consists predominantly of photons from unsuppressed π^0's (73%), and photons from η decay (18%).

Fitting the Mass Difference

Since the background to the χ_c signal comes mostly from real J/ψ's combined with uncorrelated photons, a Monte Carlo simulation should model the background well. We verified this expectation by making various combinations of Monte Carlo and data photons with Monte Carlo and data J/ψ candidates. The magnitude of the background is simulated to within one standard deviation by the J/ψ Monte Carlo, if one scales the Monte Carlo prediction to the observed number of J/ψ candidates plus the random dilepton background within the J/ψ mass window.

Fig. 4.14 shows a fit with only χ_{c1} allowed. The χ_{c1} line shape was determined from Monte Carlo. In this case we find 112$\pm$17 events in the peak with a confidence level of 0.05%, indicating poor agreement with the observed mass difference distribution.

A better fit is obtained by allowing for both the χ_{c1} and χ_{c2} (Fig. 4.15), with the mass difference between the χ_{c1} and χ_{c2} fixed in the fit. We find the χ_{c1} signal to be unchanged, 112±17 events, and also find 35±13 events in the χ_{c2} region. The confidence level of this fit is still only 0.2%. To help investigate the sensitivity of the result to background shape, we also used a second order Chebychev polynomial for the background shape. In this case, the fitted number of events in the χ_{c1} peak is 110±18, and the excess in the χ_{c2} region is 37±14. The confidence level for this fit improves to 7%.

The world average branching fractions for the decays $\chi_{c1}\rightarrow J/\psi\gamma$ and $\chi_{c2}\rightarrow J/\psi\gamma$ are (27.3±1.6)% and (13.5±1.1)%, respectively[1]. We would not expect to see χ_{c0} even if it were produced, because the branching fraction for $\chi_{c0}\rightarrow J/\psi\gamma$ is only (0.66±0.18)%. The efficiencies for detecting χ_{c1} and χ_{c2} were determined from Monte Carlo to be 20% for each state. We use the numbers from the fit with the Monte Carlo background shape to determine the branching fraction, and use the alternative fit with the polynomial background to help assess the systematic error. The branching fraction for $B\rightarrow\chi_{c1}$X is (0.40±0.06±0.04)%. The dominant systematic errors are associated with identifying the leptons and with the $\chi_{c1}\rightarrow J/\psi\gamma$ branching fraction. The systematic error in the efficiency for identifying the photon is 2.5%. The upper limit for the decay $B\rightarrow\chi_{c2}$X branching fraction is 0.38% at 90% confidence level. If we interpret the excess in the χ_{c2} signal region of the mass difference plot as $B\rightarrow\chi_{c2}$X, then we find a branching fraction of (0.25±0.10±0.03)%.

4.2.5 Summary of Inclusive Results

Table 4.3 summarizes our inclusive measurements and, for comparison, presents the corresponding values compiled by the Particle Data Group (PDG). The new branching fraction for $B\rightarrow J/\psi$ X is about the same as that from the PDG, but this agreement is accidental, as the branching fraction used by the PDG was determined using older

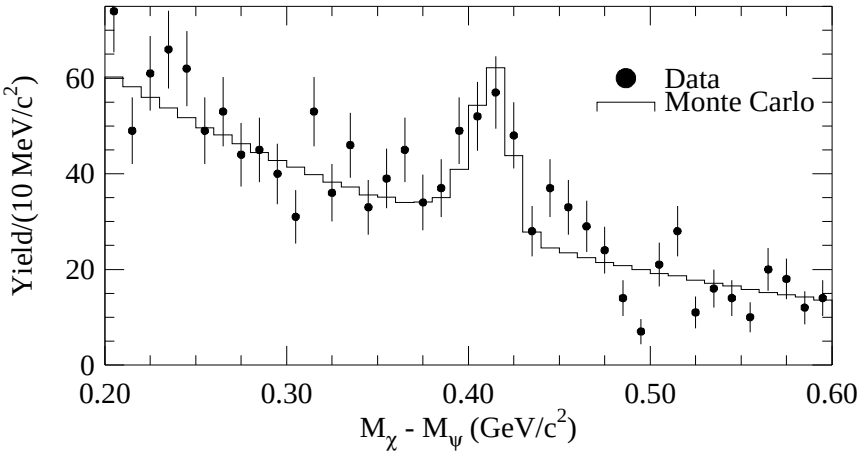

Figure 4.14: Mass-difference distribution for $J/\psi\gamma$ candidates, with fit to $B\to\chi_{c1}$X Monte Carlo and polynomial background.

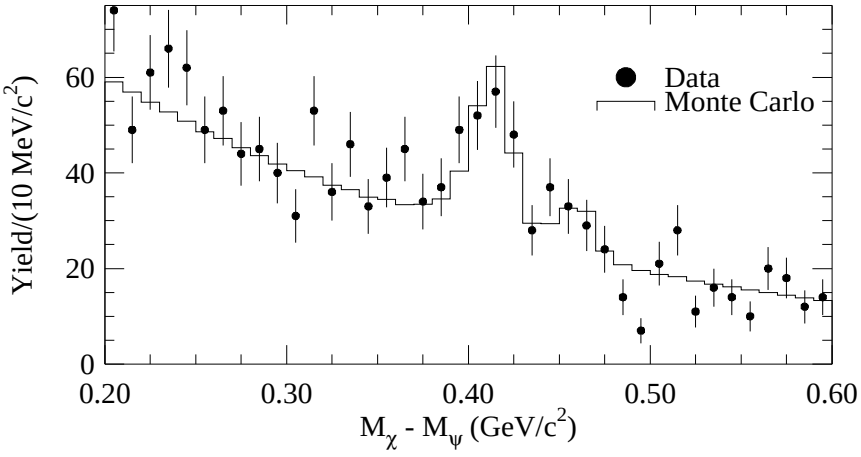

Figure 4.15: Mass-difference distribution for $J/\psi\gamma$ candidates, with fit to $B\to\chi_{c1}$X and $B\to\chi_{c2}$X Monte Carlo and polynomial background.

Charmonium	Yield	Branching Fraction (%)	PDG[1]	PDG Corrected
J/ψ	1455±49	1.13±0.04±0.06	1.12±0.16	1.31±0.19
$\psi'\to\ell^+\ell^-$	127±21	0.30±0.05±0.04		
$\psi'\to J/\psi\pi^+\pi^-$	113±16	0.38±0.05±0.05		
ψ' combined		0.34±0.04±0.03	0.46±0.20	0.53±0.23
χ_{c1}	112±17	0.40±0.06±0.04		
χ_{c2}	35±13	0.25±0.10±0.03		

Table 4.3: Inclusive $B\to$Charmonium X.

and larger $J/\psi\to\ell^+\ell^-$ branching fractions. The PDG value for $B\to J/\psi$X, corrected to use the newer $J/\psi\to\ell^+\ell^-$ branching fraction, is also given in Table 4.3. It is somewhat larger than, but consistent with, our result. The new ψ' branching fraction is consistent with the old PDG value as well as the corrected value. The errors for both the J/ψ and ψ' modes have been reduced by a factor of 3. In addition, our measurement of the ψ' momentum spectrum is the first which has been made.

Argus has reported a $B\to\chi_{c1}$X branching fraction of (1.05±0.35±0.25)%[33]. Their study did not have sufficient energy resolution to distinguish a χ_{c1} signal from possible χ_{c2} production. On theoretical grounds they assumed that their signal was entirely $B\to\chi_{c1}$X. The new CLEO-II measurement is 1.5 standard deviations lower than the ARGUS measurement. It is 2.2 standard deviations lower than the L3 measurement of [(2.4±0.9±0.2)%][34]. It is consistent with a preliminary CLEO-II measurement (0.54±0.15±0.09)%[31], which was based on the first 30% of the data sample used for this analysis. The χ_{c2} measurement is 2.5 standard deviations in statistical significance. The theoretical implications of these measurements are discussed in Chapter 5.

4.3 EXCLUSIVE MEASUREMENTS

Beginning with the inclusive sample described in Section 4.2, we searched for several exclusive two-body B decays to charmonium. A total of twelve decay channels were investigated: $B^-\to$charmonium K^-, $\overline{B}^0\to$charmonium $\overline{K^0}$, $B^-\to$charmonium K^{*-}, and

$\overline{B}^0 \rightarrow$charmonium $\overline{\mathrm{K}}^{*0}$, where charmonium refers to J/ψ, ψ' or χ_{c1}. The strategy for reconstruction exploited the fact the B-meson energy is equal to the well known beam energy. We calculated the invariant mass of the B meson using the three-vector momenta of all constituent particles and the beam energy. The use of the beam constraint provides a factor of ten better mass resolution than using the sum of the energy of all the B-decay products. We required the difference (ΔE) between the sum of the decay product energies to be within 2.5 standard deviations of the beam energy, as determined by Monte Carlo for each decay channel.

Charmonium candidates were reconstructed for exclusive measurements in the same way they were for inclusive ones. For all modes with a J/ψ dielectron final state we used an asymmetric cut around the measured J/ψ mass of (3091^{+45}_{-150}) MeV/c^2, to reduce the loss from final-state radiation. This represents -10 standard deviations below and 3 above the J/ψ mass. (For both dielectron and dimuon events, the J/ψ mass resolution without final-state radiation is 15 MeV/c^2.) For the dimuon mode the mass cut was (3097 ± 45) MeV/c^2. The efficiency for a J/ψ to pass the mass cuts as well as the tracking and lepton identification cuts is 48.5% for dielectrons and 42.6% for dimuons. To increase efficiency for the very clean modes $B^- \rightarrow J/\psi \mathrm{K}^-$ and $\overline{B}^0 \rightarrow J/\psi \overline{\mathrm{K}^0}$ we require only one identified lepton. This improved the efficiency for finding a J/ψ to 54.6% for the dielectron mode and 68.0% for the dimuon mode.

Reconstruction of the ψ' in the decay mode $\psi' \rightarrow \ell^+\ell^-$ follows that for reconstruction of the decay of the J/ψ but with the mass cuts changed to (3678^{+54}_{-180}) MeV/c^2 and (3686 ± 54) for the dielectron and dimuon modes respectively; the ψ' mass resolution without final-state radiation is 18 MeV/c^2.

For reconstruction of a ψ' with the decay mode $\psi' \rightarrow J/\psi\pi^+\pi^-$, the mass difference between the ψ' candidate and J/ψ candidate, was required to be within the range (589 ± 10) MeV/c^2, representing a ±3 standard deviation window around the $\psi' - J/\psi$ mass difference. For reconstruction of the χ_{c1} the mass difference between the χ_{c1}

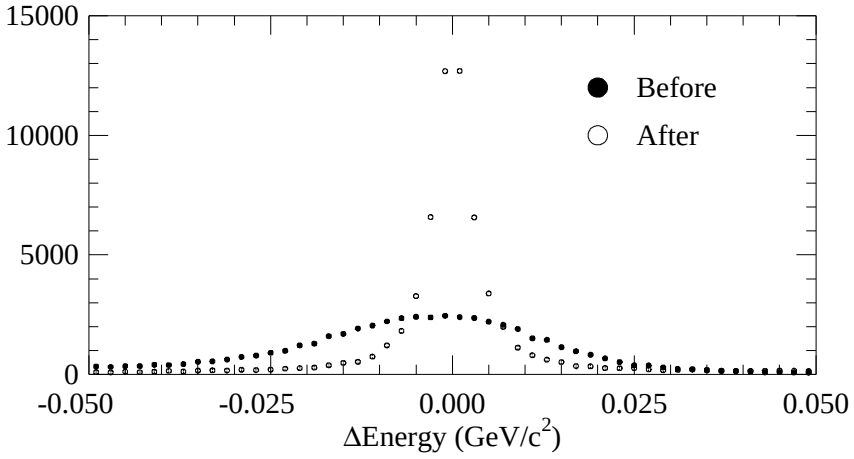

Figure 4.16: The difference between the generated and reconstructed energies for Monte Carlo J/ψ's, before and after kinematically constraining the dileptons to the known J/ψ mass.

candidate and J/ψ candidate was required to be within the range (413^{+15}_{-30}) MeV/c^2, representing a -3 to $+1.5$ standard deviation window around the known $\chi_{c1}-J/\psi$ mass difference. The narrow region above is to avoid contributions from the χ_{c2} (ignoring the small non-Gaussian tail, the cut is 3 standard deviations below the known $\chi_{c2}-J/\psi$ mass difference).

For use in the calculation of the energy of the B, the dilepton mass of the J/ψ or ψ' candidate, where $\psi' \to \ell^+\ell^-$, was kinematically constrained to the known values. This increased the resolution on the $J/\psi(\psi')$ energy by a factor of six (most of the energy of the J/ψ and ψ' is in the mass). Fig. 4.16 shows the effect of the constraint on the energy resolution of the J/ψ.

The K and K* candidates were formed from the charged tracks left over from the formation of charmonium candidates, and in one case also from π^0 candidates. Loose track quality cuts were applied to remove poorly measured tracks. The distance of closest approach of the track to the beam spot was required to be less than 5 mm in the x-y plane and less than 50 mm in the z direction. The residual of the hits used in

reconstructing the track was required to be less than 1 mm.[3] A 2.0 GeV/c momentum cut was also applied to each track. The K^- and π^- candidates were required to have dE/dx measurements within three standard deviations of that expected for a charged kaon or pion if that information was available. K^0_S's were reconstructed from pairs of oppositely charged tracks where the reconstructed vertex was at least 0.5 mm away from the event vertex. π^0 candidates were required to have a mass within 2.5 standard deviations of the nominal π^0 mass. The π^0 photons were kinematically constrained to the π^0 mass and the χ^2 of the fit was required to be less than 10. The $\overline{K}^{*0}$ was reconstructed only in the $K^-\pi^+$ channel while the K^{*-} was reconstructed in both the $\overline{K^0}\pi^-$ and $K^-\pi^0$ modes. The mass of K^* candidates was required to be within 75 MeV of the known K^* mass.

Results for modes with ψ' were combined by adding the background subtracted yields for the $\psi' \to \ell^+\ell^-$ and $\psi' \to J/\psi\pi^+\pi^-$ channels, and dividing by the total efficiency (including branching fractions for $\psi' \to \ell^+\ell^-$, $\psi' \to J/\psi\pi^+\pi^-$ and $J/\psi \to \ell^+\ell^-$). Systematic errors were combined by first separating out the common errors and then averaging the non-common errors weighted by the relative expected yields.

Systematic errors on the efficiency derived from the Monte Carlo simulation were calculated by the formula:

$$\sqrt{(\mathrm{J} * \sigma_{lepid})^2 + (\mathrm{K} * \sigma_{leptrk})^2 + (\mathrm{L} * \sigma_{hadid})^2 + (\mathrm{M} * \sigma_{track})^2 + (\mathrm{N} * \sigma_{shower})^2}. \quad (4.1)$$

J is the number of identified leptons, and σ_{lepid} is the error on the simulation of the lepton identification (2.7%, accounting for barrel versus end cap and dielectron versus dimuon). K is the number of lepton tracks and σ_{leptrk} is the error in the tracking simulation for the relatively high momentum lepton tracks (1%). L is the number of identified hadrons, and σ_{hadid} is the error on the simulation of the hadron identification (2%). M is the number of charged hadron tracks in the reconstructed B, and σ_{track} is the

[3]The residual is the root-mean-square difference between the expected and measured distances hits are from the reconstructed track.

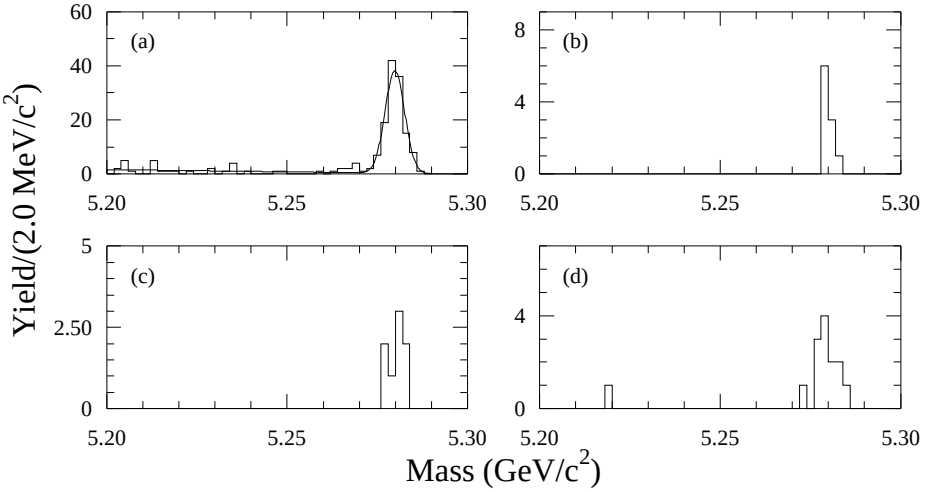

Figure 4.17: Exclusive $B^-\rightarrow$Charmonium K^-: (a) $B^-\rightarrow J/\psi K^-$; (b) $B^-\rightarrow\psi' K^-$, $\psi'\rightarrow\ell^+\ell^-$; (c) $B^-\rightarrow\psi' K^-$, $\psi'\rightarrow J/\psi\pi^+\pi^-$; (d) $B^-\rightarrow\chi_{c1} K^-$.

error on the tracking simulation (2%). N is the number of photons in the reconstructed B, and σ_{shower} is the error on the photon shower simulation (2.5%). The errors on the number of B mesons (1.6%), on the R_2 cut (2%) and the Monte Carlo statistics (1.3-13%) were also included in the systematic error.

Except for the decay mode $B^-\rightarrow J/\psi K^-$ the background for each K^- and $\overline{K^0}$ mode was measured by taking the yield between 5.20 and 5.25 GeV/c^2 and scaling to the width of the signal region (0.016 GeV/c^2). The background for K^* modes was estimated from energy sidebands, as discussed below.

4.3.1 $B^-\rightarrow$Charmonium K^-

The reconstruction of $B^-\rightarrow$charmonium K^- was very clean. Fig. 4.17 shows the B-mass plots for the four charmonium channels. In order to increase the efficiency in the $J/\psi K^-$ mode, the requirement that two leptons be identified was relaxed to require only one identified lepton. The yield for this mode was estimated by simultaneously fitting the signal region to a Gaussian with a width fixed to the beam energy resolution (2.7

MeV/c^2) and the background to a straight line over the region 5200 to 5290 MeV/c^2. The mode provides a very clean signal for determining the B^--meson mass. The B^--meson mass in the fit is (5279.6±0.3) MeV/c^2 where the error is from the fit. Correcting for initial state radiation[35, 36] the value would be (5278.5±0.3±0.5±2.0) MeV/c^2. The first systematic error is due to the uncertainty in the correction for initial state radiation while the second, and dominant error, is for uncertainties in the absolute value of the CESR energy scale. Part of the data sample used here has been used in combination with other fully reconstructed decay modes with D mesons to measure not only the B^--meson mass but also the $B^- - \overline{B}^0$ mass difference[36]. Background for the ψ' and χ_c modes was determined by scaling the number of events in the region between 5200 and 5250 MeV/c^2 to the width of the signal region (16 MeV/c^2).

In Table 4.4 are the measured branching fractions. In most cases the statistical error is larger than the systematic.

4.3.2 $\overline{B}^0 \rightarrow$ Charmonium $\overline{\mathrm{K}^0}$

In the reconstruction of $\overline{B}^0 \rightarrow$charmonium $\overline{\mathrm{K}^0}$, the $\overline{\mathrm{K}^0}$ was reconstructed through the K^0_S channel. The requirement that the K^0_S vertex be separated from the beam spot lead to a very clean signal. As with the $J/\psi\mathrm{K}^-$ mode, for the $J/\psi\overline{\mathrm{K}^0}$ only one lepton was required to be identified. Figs. 4.18 show the $\overline{B}^0$-mass plots for the four charmonium channels.

4.3.3 $B^- \rightarrow$ Charmonium K^{*-}

The K^{*-} is detected through both the $\mathrm{K}^-\pi^0$ and $\mathrm{K}^0\pi^-$ modes. Background to the K^* modes comes predominantly from a real J/ψ and a real K that has been matched to a real but unrelated π. The mode $\mathrm{K}^{*-} \rightarrow \mathrm{K}^-\pi^0$ is particularly subject to background from the large number of low momentum π^0's produced in hadronic B decay. These π^0's can combine with a K^- from $\overline{\mathrm{K}}^{*0} \rightarrow \mathrm{K}^-\pi^+$ to fake a K^{*-}. If one assumes that the

Charmonium	Kaon	Yield†	Scaled B.G.	Energy Resol.	MC Eff.	Branching Fraction (%)
J/ψ	K^-	125	Fit	13	46.5	0.104±0.010±0.006
	$\overline{K^0}$	29	0.8	13	34.4	0.092±0.018±0.008
	$K^{*-}\to K^-\pi^0$ ‡	17	1.0	21	7.2	0.256±0.068±0.028
	$K^{*-}\to\overline{K^0}\pi^-$	15	0.5	11	16.4	0.149±0.040±0.018
	$\overline{K}^{*0}\to K^-\pi^+$	67	5.8	12	22.4	0.158±0.022±0.015
$\psi'\to\ell^+\ell^-$	K^-	10	0.0	10	36	0.076±0.024±0.011
	$\overline{K^0}$	2	0.0	8	28	0.058±0.041±0.009
	$K^{*-}\to K^-\pi^0$ ‡	2	0.9	18	7.7	0.120±0.180±0.020
	$K^{*-}\to\overline{K}^*\pi^-$	0	0.0	8	16.0	< 0.17
	$\overline{K}^{*0}\to K^-\pi^+$	7	0.5	10	24	0.112±0.046±0.018
$\psi'\to J/\psi\pi^+\pi^-$	K^-	8	0.0	11	14.4	0.066±0.023±0.009
	$\overline{K^0}$	3	0.0	10	10.7	0.098±0.056±0.017
	$K^{*-}\to K^-\pi^0$ ‡	4	0.0	18	2.3	0.637±0.318±0.118
	$K^{*-}\to\overline{K^0}\pi^-$	1	0.0	9	5.3	0.099±0.099±0.020
	$\overline{K}^{*0}\to K^-\pi^+$	5	0.5	10	8.5	0.094±0.048±0.015
ψ': Combined	K^-					0.072±0.017±0.011
	$\overline{K^0}$					0.076±0.034±0.012
	$K^{*-}\to K^-\pi^0$ ‡					0.330±0.168±0.055
	$K^{*-}\to\overline{K^0}\pi^-$					0.043±0.043±0.008
	$\overline{K}^{*0}\to K^-\pi^+$					0.104±0.033±0.016
χ_{c1}	K^-	13	0.3	17	13.7	0.087±0.025±0.009
	$\overline{K^0}$	0	0.0	15	14.6	< 0.07
	$K^{*-}\to K^-\pi^0$ ‡	0	1.5	15	3.4	< 0.29
	$K^{*-}\to\overline{K^0}\pi^-$	1	0.0	15	10.7	< 0.39
	$\overline{K}^{*0}\to K^-\pi^+$	6	2.2	14	13.0	< 0.17

Table 4.4: Exclusive $B\to$Charmonium X. Limits are 90% confidence level. †Before Background Subtraction. ‡With helicity cut.

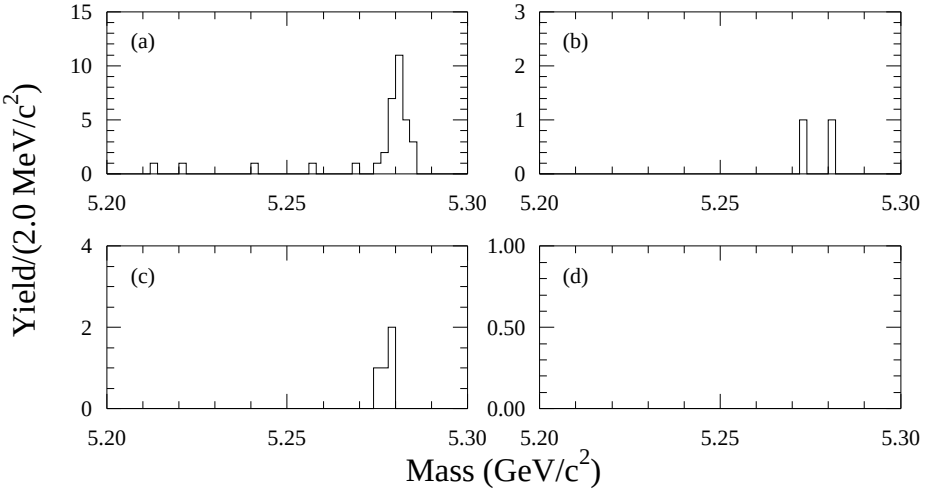

Figure 4.18: Exclusive $\overline{B}^0 \rightarrow$Charmonium $\overline{\mathrm{K}^0}$: (a) $\overline{B}^0 \rightarrow J/\psi \overline{\mathrm{K}^0}$; (b) $\overline{B}^0 \rightarrow \psi' \overline{\mathrm{K}^0}$, $\psi' \rightarrow \ell^+\ell^-$; (c) $\overline{B}^0 \rightarrow \psi' \overline{\mathrm{K}^0}$, $\psi' \rightarrow J/\psi\pi^+\pi^-$; (d) $\overline{B}^0 \rightarrow \chi_{c1} \overline{\mathrm{K}^0}$.

Mode	Branching Fraction	Fake Rate	Yield
$J/\psi \mathrm{K}^-$	0.104%	0.06%	0.2
$J/\psi \overline{\mathrm{K}^0}$	0.092%	0.5%	0.5
$J/\psi \overline{\mathrm{K}}^{*0}$	0.158%	2.7%	8.8
J/ψ Other	0.776%	0.13%	3.1
Total			12.6

Table 4.5: Monte Carlo calculation of fakes for $\mathrm{K}^{*-} \rightarrow \mathrm{K}^-\pi^0$. The daughter branching fractions and reconstruction efficiency are not included in the fake rates.

branching fraction for $\overline{B}^0 \rightarrow$charmonium $\overline{\mathrm{K}}^{*0}$ is the same as $B^- \rightarrow$charmonium K^{*-} then one expects twice as many K^-'s from $\overline{\mathrm{K}}^{*0}$'s than from K^{*-}'s. (The branching fraction for $\overline{\mathrm{K}}^{*0} \rightarrow \mathrm{K}^-\pi^+$ is 66.6% while that for $\mathrm{K}^{*-} \rightarrow \mathrm{K}^-\pi^0$is 33.3%.)

From Monte Carlo we determined the rate for various exclusive modes faking a $J/\psi \mathrm{K}^{*-}$ (see Table 4.5). This background has a broad peak that contributes in the signal region (see Fig. 4.19). The total number of fakes predicted is 12.6. An alternative way to estimate background is to examine the energy sidebands, that is the region where ΔE is outside the range where correctly reconstructed B mesons lie. We use 50 MeV/c^2

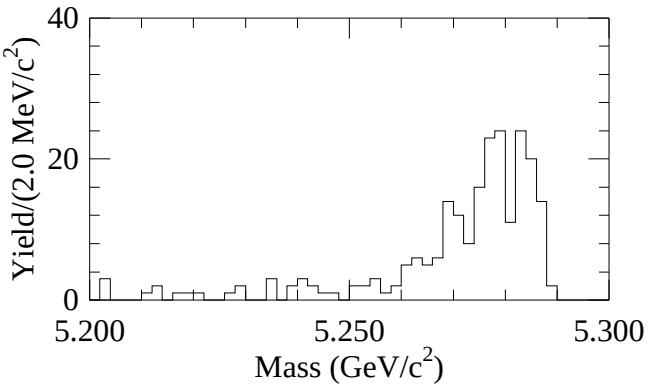

Figure 4.19: Line shape of $\overline{B}^0 \rightarrow J/\psi \overline{\mathrm{K}}^{*0}$, $\overline{\mathrm{K}}^{*0} \rightarrow \mathrm{K}^- \pi^+$ Monte Carlo reconstructed as $B^- \rightarrow J/\psi \mathrm{K}^{*-}$, $\mathrm{K}^{*-} \rightarrow \mathrm{K}^- \pi^0$.

regions that begin ± 5 standard deviations away from ΔE equal zero to avoid the non-Gaussian tails that result from constraining the J/ψ or ψ' candidate to their known masses. The background found this way is 10.1, consistent with that found using Monte Carlo. Fig. 4.20 shows the yields for the four charmonium channels.

Monte Carlo studies also showed that 80% of the background that comes from K^{*-} decays with a helicity angle such that the π^0 is moving opposite to the direction of the K^{*-} (i.e. slow π^0s). Making a helicity cut at zero degrees should eliminate 80% of the background but keep 50% of the signal. Fig. 4.21 shows the yield with the helicity cut applied.

A much cleaner way to reconstruct K^{*-} is to use the mode $\overline{\mathrm{K}^0}\pi^-$. This mode is cleaner for several reasons. First, the energy resolution for this mode is half as that for the $\mathrm{K}^-\pi^0$ mode (π^0's have relatively poor energy resolution). Second the feed across from the decay of $\overline{\mathrm{K}}^{*0} \rightarrow \overline{\mathrm{K}^0}\pi^0$, where the $\overline{\mathrm{K}^0}$ combines with an uncorrelated π^- contributes a relatively smaller amount than feed across from $\overline{\mathrm{K}}^{*0} \rightarrow \mathrm{K}^- \pi^+$ into the $\mathrm{K}^{*-} \rightarrow \mathrm{K}^- \pi^0$ mode. This is due to the relative branching fractions. The branching fraction for (1) $\overline{\mathrm{K}}^{*0} \rightarrow \mathrm{K}^- \pi^+$ is 66.6% while the branching fraction for (2) $\overline{\mathrm{K}}^{*0} \rightarrow \overline{\mathrm{K}^0}\pi^0$ is 33.3%. The branching fraction for (3) $\mathrm{K}^{*-} \rightarrow \mathrm{K}^- \pi^0$ is 33.3% while the branching

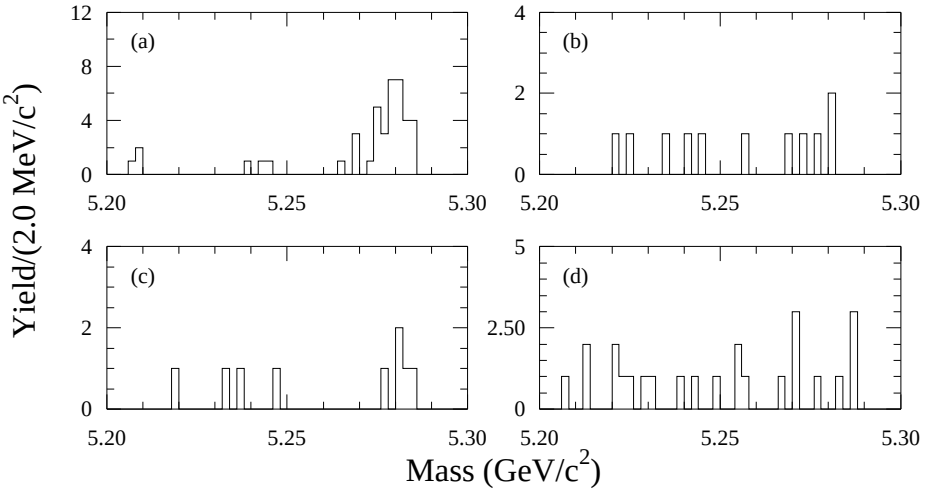

Figure 4.20: Exclusive $B^-\to$Charmonium K^{*-}, $K^{*-}\to K^-\pi^0$: (a) $B^-\to J/\psi K^{*-}$; (b) $B^-\to\psi' K^{*-}$, $\psi'\to\ell^+\ell^-$; (c) $B^-\to\psi' K^{*-}$, $\psi'\to J/\psi\pi^+\pi^-$; (d) $B^-\to\chi_{c1}K^{*-}$.

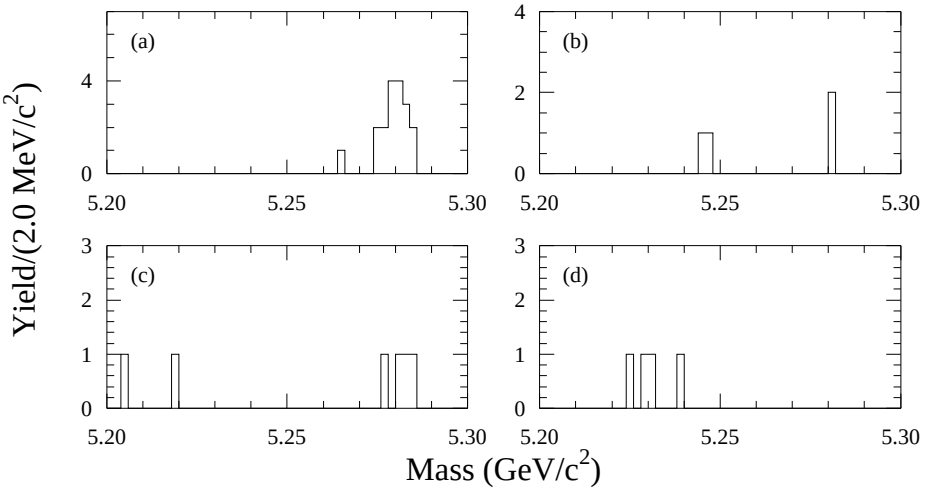

Figure 4.21: Exclusive $B^-\to$Charmonium K^{*-} with helicity cut, $K^{*-}\to K^-\pi^0$: (a) $B^-\to J/\psi K^{*-}$; (b) $B^-\to\psi' K^{*-}$, $\psi'\to\ell^+\ell^-$; (c) $B^-\to\psi' K^{*-}$, $\psi'\to J/\psi\pi^+\pi^-$; (d) $B^-\to\chi_{c1}K^{*-}$.

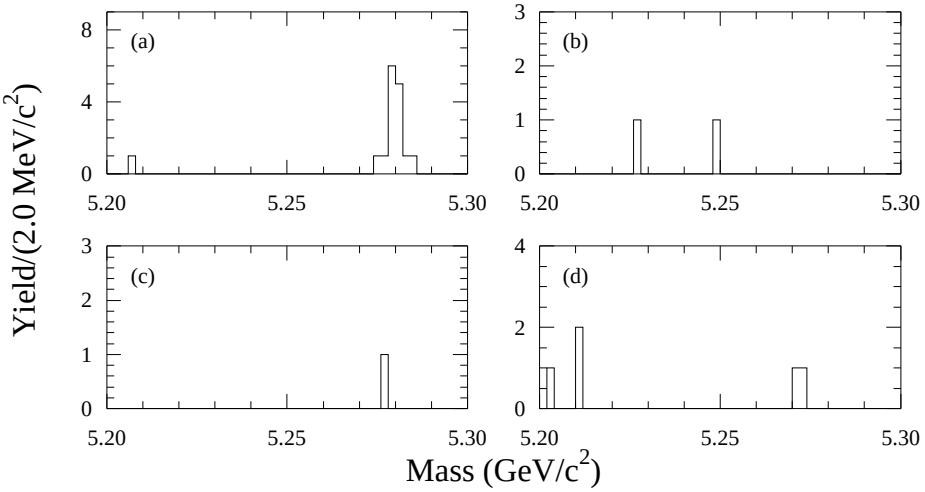

Figure 4.22: Exclusive $B^-\to$Charmonium K^{*-}, $K^{*-}\to\overline{K^0}\pi^-$: (a) $B^-\to J/\psi K^{*-}$; (b) $B^-\to\psi' K^{*-}$, $\psi'\to\ell^+\ell^-$; (c) $B^-\to\psi' K^{*-}$, $\psi'\to J/\psi\pi^+\pi^-$; (d) $B^-\to\chi_{c1}K^{*-}$.

fraction for (4) $K^{*-}\to\overline{K^0}\pi^-$ is 66.6%. Thus the contribution to the background of (3) to (1) is 25% of the contribution of (4) to (2). (50% from relative signal size and 50% from relative background size.) The advantage of the relative branching fractions is partially offset by the larger number of π^-'s in B-meson decay as compared to π^0's. A third reason is that it is easy for a π^- to fake a K^- but difficult for anything to fake a K^0_S.

The yields for this mode are shown in Fig. 4.22. From ΔE sidebands there is no background to these modes.

4.3.4 $\overline{B}^0\to$Charmonium $\overline{K}^{*0}$

We only reconstructed the $\overline{K}^{*0}$ in the relatively clean mode $\overline{K}^{*0}\to K^-\pi^+$. The yields for this mode are shown in Fig. 4.23. The relatively small background was estimated from ΔE sidebands.

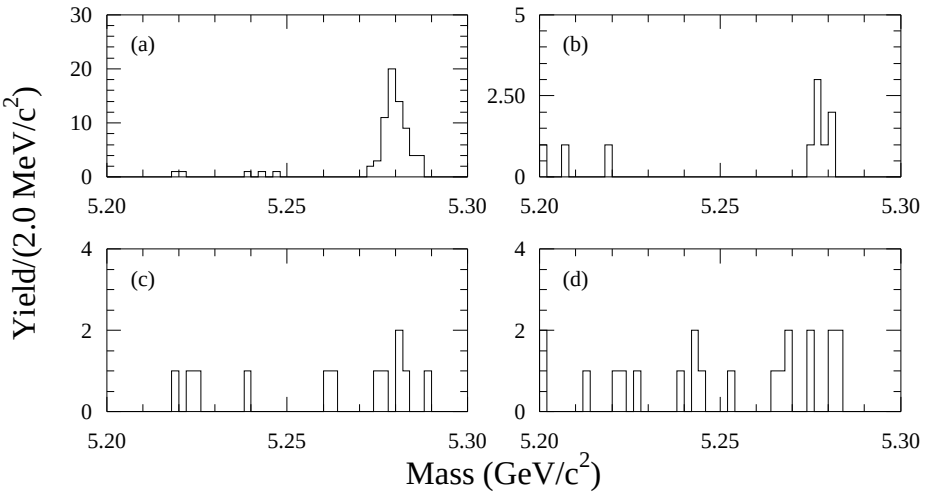

Figure 4.23: Exclusive $\overline{B}^0 \rightarrow$Charmonium $\overline{\mathrm{K}}^{*0}$: (a) $\overline{B}^0 \rightarrow J/\psi \overline{\mathrm{K}}^{*0}$; (b) $\overline{B}^0 \rightarrow \psi' \overline{\mathrm{K}}^{*0}$, $\psi' \rightarrow \ell^+\ell^-$; (c) $\overline{B}^0 \rightarrow \psi' \overline{\mathrm{K}}^{*0}$, $\psi' \rightarrow J/\psi\pi^+\pi^-$; (d) $\overline{B}^0 \rightarrow \chi_{c1} \overline{\mathrm{K}}^{*0}$.

4.3.5 Summary of Exclusive Results

In Table 4.6 is a comparison of the new CLEO-II results with earlier measurements. For this table the background subtracted yield from the mode $\mathrm{K}^{*-} \rightarrow \mathrm{K}^-\pi^0$ with helicity cut was added to the yield from $\mathrm{K}^{*-} \rightarrow \overline{\mathrm{K}^0}\pi^-$. In calculating the branching fraction the total efficiencies of both modes were added together. The two ψ' modes were added together in the same way.

The results are consistent with and a approximately a factor of two better in statistical precision than previous measurements. The largest discrepancy is with the branching ratio for $B^- \rightarrow J/\psi \mathrm{K}^-$ which is 1.2 sigma larger than the PDG value. We now see the decays $B^- \rightarrow \psi' \mathrm{K}^-$, $B^- \rightarrow \psi' \mathrm{K}^{*-}$, and $\overline{B}^0 \rightarrow \psi' \mathrm{K}^0$ for which previously existed only upper limits.

Charm	Kaon	PDG (ARGUS χ_{c1})	CLEO II 1994 PRD[36]	CLEO II (Here)
J/ψ	K^-	0.077±.020	0.110±0.015±0.009	0.104±0.010±0.006
	$\overline{K^0}$	0.065±.031	0.075±0.024±0.008	0.092±0.018±0.008
	K^{*-}	0.14±.07	0.178±0.051±0.023	0.191±0.036±0.022
	$\overline{K}^{*0}$	0.13±.04	0.169±0.031±0.018	0.158±0.022±0.015
ψ'	K^-	< 0.2	0.061±0.023±0.009	0.072±0.017±0.011
	$\overline{K^0}$	< 0.15	< 0.08	0.076±0.034±0.012
	K^{*-}	< 0.35	< 0.30	0.157±0.068±0.027
	$\overline{K}^{*0}$	0.14±0.09	< 0.19	0.104±0.033±0.016
χ_{c1}	K^-	0.19±0.13±0.06	0.097±0.040±0.009	0.087±0.025±0.009
	$\overline{K^0}$		< 0.27	< 0.07
	K^{*-}		< 0.21	< 0.15
	$\overline{K}^{*0}$		< 0.21	< 0.17

Table 4.6: Exclusive branching fractions for $B\rightarrow$Charmonium X (in %). Comparison with previous results. The CLEO II PRD 1994 numbers are based on the first half of the data set used here. Limits are 90%.

Chapter 5

CONCLUSIONS

In the previous chapter we have extracted various parameters describing the decays of B mesons to final states that include charmonium mesons. In this chapter those results will be compared to theoretical predictions.

Predictions of experimental observables like branching fractions can be divided into two classes: absolute and relative. An absolute prediction of the branching fraction for $B \to J/\psi X$, for example, would give the fraction of all B decays with a J/ψ among the daughter particles. A relative prediction of the branching fraction for $B \to \psi' X$, on the other hand, would be a statement that the ratio of the branching fraction for $B \to \psi' X$ to the branching fraction for $B \to J/\psi X$ would have some particular value. The latter type of prediction is in many respects easier, as many of the uncertainties cancel.

5.1 INCLUSIVE

The measured branching fraction for $B \to J/\psi X$ can be broken down into two parts. The first, and most important, is that which results from "direct" production. The second is the part that comes from the "feed-down" from other charmonium modes, such as $B \to \psi' X$, $\psi' \to J/\psi \pi^+ \pi^-$. The natural thing for theorists to calculate is the

Decay Mode	Feed Down Mode	Feed Down BF[1]	Measured BF	Contribution to J/ψ
$B \to J/\psi X$			1.13±0.04±0.06	1.13±0.07
$B \to \chi_{c1} X$	$\chi_{c1} \to J/\psi\gamma$	27.3±1.6	0.40±0.06±0.04	0.10±0.02
$B \to \chi_{c2} X$	$\chi_{c2} \to J/\psi\gamma$	13.5±1.1	0.25±0.10±0.03	0.03±0.01
$B \to \psi' X$	$\psi' \to J/\psi X$	57±4	0.34±0.04±0.03	0.19±0.03
$B \to J/\psi X$ (direct)				0.81±0.08
$B \to \chi_{c1} X$			0.40±0.06±0.04	0.40±0.07
$B \to \psi' X$	$\psi' \to \chi_{c1}\gamma$	8.7±0.8	0.34±0.04±0.03	0.03±0.01
$B \to \chi_{c1} X$ (direct)				0.37±0.07
$B \to \chi_{c2} X$			0.25±0.10±0.03	0.25±0.10
$B \to \psi' X$	$\psi' \to \chi_{c2}\gamma$	7.8±0.8	0.34±0.04±0.03	0.03±0.01
$B \to \chi_{c2} X$ (direct)				0.23±0.10

Table 5.1: Calculation of direct branching fractions for $B \to J/\psi X$, $B \to \chi_{c1} X$, and and $B \to \chi_{c2} X$. All branching fractions are in (%).

direct production. To make comparisons with such predictions, experimentalists must reduce the measured inclusive $B \to J/\psi X$ branching fraction by the best estimate of the feed-down contributions. In many cases feed-down corrections must be based on theoretical prediction, or conjecture. With our extensive set of inclusive measurements we can compute all expected contributions.

We assume the feed down to the inclusive J/ψ signal comes from ψ' and χ_c. Applying the corrections outlined in (Table 5.1), we find the direct branching fraction to be (0.81±0.08)%. The $B \to \chi_c X$ branching fractions must also be adjusted slightly for feed down from ψ''s, again as shown in Table 5.1. Since there is no known feed-down mechanism for ψ' production, we assume that the direct branching fraction for $B \to \psi' X$ is equal to the measured branching fraction. (Charmonium states above with masses above the ψ' are above the threshold for $D\overline{D}$ meson production and decay almost exclusively through that mode.)

Theoretical predictions of the inclusive decay $B \to J/\psi X$ began with the suggestion by Fritzsch that B mesons would be most easily seen through this mode due to the clean dilepton signature of the J/ψ[37]. His basic assumption was that the $B \to J/\psi X$

process is described by $b \to J/\psi s$. The assumption that the quark paired to the b can be ignored is known as a spectator model. He made a rough estimate that the percentage of B decays that include a J/ψ should be in the range of 3-5%, if strong interactions are ignored. He also estimated that half of those J/ψ's should come from feed-down from other charmonium states. Wise expanded on the spectator model[38]. His calculation of the direct branching fraction agrees with Fritzsch, if he also ignores strong interactions. Using the leading logarithmic approximation to estimate the effect of strong interactions, Wise finds the branching fraction is smaller, as the $c\overline{c}$ pair must be in a color singlet. This effect is referred to as color suppression. Higher order corrections may reduce (or enhance) this suppression.

The relative rates for $B \to J/\psi$X and $B \to \psi'$X differ to first order only in the radial wave function of the charmonium meson[5, 38, 39].

$$\Gamma(b \to J/\psi + s) = \frac{G_F^2}{12\pi^2} \mathrm{V}_{cb}^2 \mathrm{V}_{cs}^2 |R(0)|^2 f(m_{J/\psi}, m_b), \tag{5.1}$$

$$\Gamma(b \to \psi' + s) = \frac{G_F^2}{12\pi^2} \mathrm{V}_{cb}^2 \mathrm{V}_{cs}^2 |R'(0)|^2 f(m_{\psi'}, m_b). \tag{5.2}$$

The ratio of $|R(0)|^2$ to $|R'(0)|^2$ is also the ratio of the electronic decay rates of J/ψ and ψ'[5]. The rate for $J/\psi \to e^+e^-$ is 5.36±0.29 keV while for $\psi' \to e^+e^-$ it is 2.14±0.21 keV[1]. Thus one expects the direct branching fraction for $B \to \psi'$X to be 40% of that for $B \to J/\psi$X. This is in reasonable agreement with the 42±6% we measure.

Predicting the relative branching fractions for B decays to χ_c's is more tricky. The transitions to χ_{c1} are mediated by an axial vector current rather than the vector current which is responsible for decays to J/ψ and ψ', and there is no experimental handle on the χ_c wave functions. Using a theoretical based wave function Kühn and Rückl find that the direct branching fraction of $B \to \chi_{c1}$X should be 27% of that for $B \to J/\psi$X[4]. Their prediction is two standard deviations smaller than our finding of 46±10%. Kühn and Rückl also argue from conservation rules that χ_{c0} and χ_{c2} can not be produced.

The difficulty of calculating absolute branching fractions for hadronic decays is

demonstrated by the spread of values calculated by theorists following similar recipes. Recall from Chapter 1 the effective Hamiltonian for charmonium production (Eq. 1.9), composed of a color singlet part and a color octet part:

$$\mathrm{H}_{Effective} = \frac{G_F}{\sqrt{2}}\mathrm{V}_{cb}\mathrm{V}_{cs}^{*}\left[\left(\frac{1}{3}c_1(\mu)+c_2(\mu)\right)(\overline{c}c)(\overline{s}b)+\frac{1}{2}c_1(\mu)(\overline{s}\lambda_i b)(\overline{c}\lambda_i c)\right]. \qquad (5.3)$$

The predicted branching fractions for $B\rightarrow J/\psi$X are proportional to the square of the coefficient of the singlet part:

$$(c_2+\frac{1}{3}c_1)^2. \qquad (5.4)$$

As was also described in Chapter 1, if the $\frac{1}{3}$ is replaced by $1/\mathrm{N}_c$, then the coefficient of the color singlet part is equivalent to the a_2 term in the factorization model of Wirbel, Stech and Bauer for exclusive decays[6]. The difference between $1/\mathrm{N}_c$ and $\frac{1}{3}$ parameterizes the non-factorizable contributions to B-meson decay[40].

Predicted branching fractions for direct $B\rightarrow J/\psi$X range from 0.2% to 2.0%, depending on the value selected for α_s (on which the Wilson coefficients c_1 and c_2 depend) and the magnitude of the color suppression (the $1/\mathrm{N}_c$ coefficient) assumed[3, 4, 5, 39, 41]. With the number of colors set to three, contributions of c_1 and c_2 almost cancel in the color-singlet term. Following the method of Ref. [5] and using the values $c_1 = 1.13$ and $c_2 = -0.29$, which include next-to-leading log corrections[40], and a b mass of 5.0 GeV/c^2, we find the prediction for the direct branching fraction for $B\rightarrow J/\psi$X to be 0.10%. However, if one replaces $(\frac{1}{3}c_1 + c_2)$ by the measured value of a_2 from exclusive decays ($0.23\pm0.01\pm0.01$[47]) then one predicts the direct branching fraction for $B\rightarrow J/\psi$X to be 0.75%, in good agreement with our measured value.

More recently Bodwin *et al.* have asserted that one should expect χ_{c0} and χ_{c2} production in B decays[5]. The contribution comes from the "color-octet" mechanism, where a color-octet $c\overline{c}$ pair is formed in an S state and then radiates a soft gluon to form a color-singlet state. This mechanism can also contribute to χ_{c1} production. The difference in the predicted χ_{c1} branching fraction from Kühn and Rückl and our

measured branching fraction may be explained by the color-octet mechanism. From this difference one can estimate χ_{c2} production. Bodwin *et al.* find the ratio of χ_{c2} production to χ_{c1} production to be 1.3:1.0. Following their method, but with the values of c_1, c_2 and b mass given above, and using the branching fraction for χ_{c1} presented here, we find that the ratio should be 1.6:1.0. This leads to a predicted branching fraction for $B\rightarrow\chi_{c2}$X of (0.56±0.15)%, where the error is limited to the experimental error of the inputs. This prediction is larger than the direct χ_{c2} branching fraction we measure. They have assumed $1/\mathrm{N}_c = \frac{1}{3}$, implying a very small contribution from the color-singlet mode, and therefore that the major contribution to the $B\rightarrow\chi_{c1}$X branching fraction is the color-octet mechanism.

When we replace $(\frac{1}{3}c_1 + c_2)$ by the a_2 from exclusive decays, the predicted color-singlet contribution to χ_{c1} production is 0.19%, leaving 0.18% for the color-octet contribution. This leads to a prediction for the direct $B\rightarrow\chi_{c2}$X branching fraction of (0.30±0.11)%. This number is in good agreement with the branching fraction of (0.23±0.10)% we obtain if we assume the marginal χ_{c2} signal is real.

Some theorists have tried to determine α_s from the branching fractions of $B\rightarrow J/\psi$X and $B\rightarrow\chi_{c1}$X[42]. The above uncertainties certainly make this suspect.

5.2 EXCLUSIVE

The models for exclusive $B\rightarrow$charmonium rely on factorization, as was discussed in Chapter 1. Much justification for factorization has been given[6, 43, 44]. The B-meson to charmonium decay modes can only measure the $|a_2|$ term. Many authors have followed the Bauer, Stech and Wirbel (BSW) model[6, 7, 45, 46]. Using fits to the BSW model, as updated by Neubert *et al.*, Browder, Honscheid and Playfer find [7, 47]

$$|a_1| = 1.07 \pm 0.04 \pm 0.06, \tag{5.5}$$

$$|a_2| = 0.23 \pm 0.01 \pm 0.01. \tag{5.6}$$

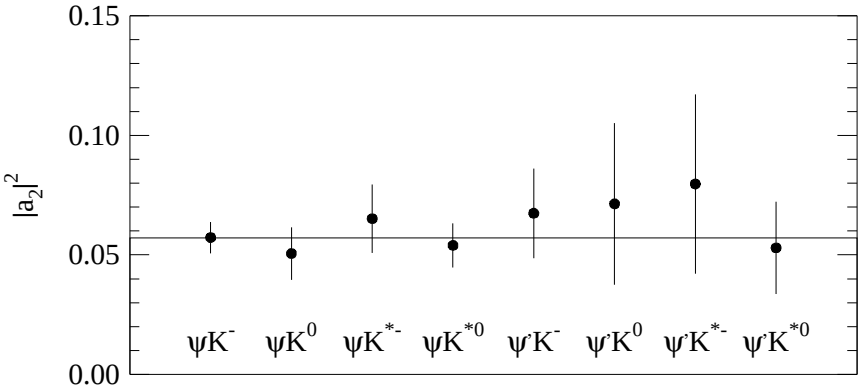

Figure 5.1: The fit to $|a_2|^2$ for eight exclusive decays using the BSW model as updated by Neubert *et al.*[7].

The first error is from the error in the measurement of the branching fractions while the second is due to uncertainties in the B-meson production fractions and lifetimes. Their determination of $|a_2|$ is based on a subset of the data used here. Using all of our data for $B \to J/\psi \mathrm{K}^{(*)}$ and $B \to \psi' \mathrm{K}^{(*)}$, we find

$$|a_2| = 0.24 \pm 0.01 \pm 0.01. \tag{5.7}$$

The χ^2 of the fit is 1.7 for 7 degrees of freedom, indicating that factorization predicts the relative rates well (Fig. 5.1). In principle, since $|a_2|$ comes from the fit to the data, the absolute rates are not tested.

From the measured value of $|a_2|$ we can extract $1/\mathrm{N}_c$. There are two solutions, one corresponding to a negative value of a_2 and one corresponding to a positive value. The negative solution gives a value of $1/\mathrm{N}_c$ very close to zero (0.04 ± 0.02). There has been some theoretical work to justify this value for $1/\mathrm{N}_c$[43]. A second solution gives $1/\mathrm{N}_c = 0.47 \pm 0.02$ (the error is experimental). To determine which of these values is correct we can look in the greater context of all exclusive B-meson decays. We know from experiment that $|a_1|$ is roughly 1.07[47]. Given the values of c_1 and c_2 from Bigi *et al.*

only the positive value for a_1 makes sense. The relative sign between a_1 and a_2 can be determined by comparing branching ratios of B^- and $\overline{B}^0$ decay modes. From fits to the data, Browder, Honscheid and Playfer determined that a_1 and a_2 have the same relative sign. Thus the value for $1/\mathrm{N}_c$ of 0.47 makes more sense.

Another check on the value of $1/N_c$ is to calculate a_1 from c_1 and c_2 using $1/\mathrm{N}_c = 0.47$. The value of a_1 found this way is 0.99. This can be compared to the experimental value from Browder, Honscheid and Playfer of $1.07\pm0.04\pm0.06$, again in good agreement. We cannot exclude the alternative of $1/\mathrm{N}_c = 0.04$, however, since in this case a_1 would be 1.11, which is also in good agreement with the experimental result. Note that the exclusive predictions using the BSW model are only valid where the color-octet mechanism, or any mechanism other than color suppression, contributes a negligible amount to the branching fractions.

Relative branching ratios can also be compared directly with predictions. Neubert *et al.* predicted the ratio of vector to pseudoscalar to be 1.6 for $B\to J/\psi\mathrm{K}^{(*)}$ and 1.9 for $B\to\psi'\mathrm{K}^{(*)}$[7]. We find 1.66 ± 0.28 for the first and 1.57 ± 0.59 for the second ratio, in good agreement. Neubert *et al.* also predict the ratio of $B^-\to J/\psi\mathrm{K}^-$ and $B^-\to\psi'\mathrm{K}^-$ to be 1.7. We find 1.4 ± 0.4, again in agreement within statistical errors.

Predictions for the exclusive branching fraction to all χ_c states (including χ_{c1}) have been made by Ward[48]. He finds that the branching fraction for $B\to\chi_c\mathrm{K}^*$ should be 1.1 times that for $B\to J/\psi\mathrm{K}^*$. Of that rate 36.5% should be to χ_{c1}. Thus $B\to\chi_{c1}\mathrm{K}^*$ should be 40% of $B\to J/\psi\mathrm{K}^*$. This is well below our upper limits, which are on the order of the $B\to J/\psi\mathrm{K}^*$ branching fractions.

5.3 SUMMARY

A good picture of the experimental knowledge of B meson decay to charmonium states is represented by the inclusive J/ψ momentum spectrum in Fig. 5.2. The exclusive

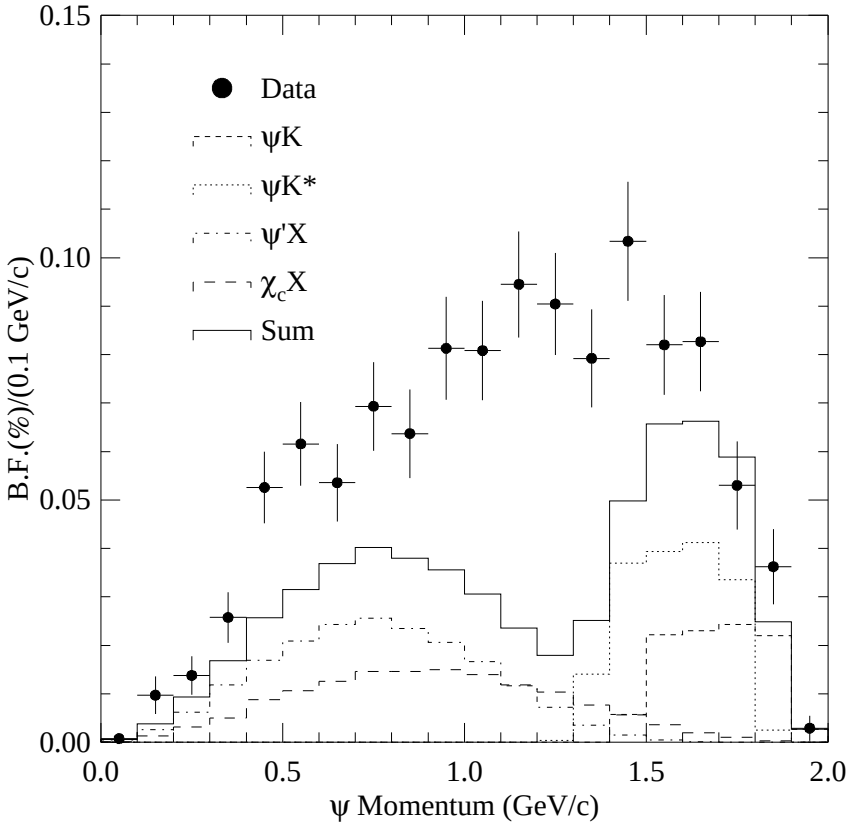

Figure 5.2: The inclusive J/ψ momentum spectrum from B-meson decays overlaid with the contributions from the inclusive decays to J/ψK and J/ψK* along with the contributions from feed down from $B \to \psi'$X and $B \to \chi_c$X. The momentum spectra for the feed-down modes is a rough estimate from Monte Carlo, where the ψ' and χ_c have a similar momentum spectra to the measure J/ψ spectrum.

decays saturate the upper two bins. One can see that there is a large contribution from higher K^* resonances or nonresonant multiparticle final states at smaller J/ψ momenta. Of the 1.13% inclusive $B \to J/\psi X$ branching fraction, the source of 0.59% is accounted for by the exclusive and feed-down modes measured in this thesis.

We have made numerous improvements to the picture of B-meson decays to states with charmonium. We find that these decays fit into a consistent picture, when the value of $|a_2|$ measured in exclusive decays is used to predict the inclusive rates. This is not too surprising, as hidden in this term are the effects of hard gluon interactions and the rearranging of the quarks to their final pairings. These effects should be independent of how the $c\overline{c}$ and $s\overline{u}$ or $s\overline{d}$ quarks hadronize. The formation of the charmonium and kaon mesons can then be treated separately. Work still needs to be done to understand the theoretical basis for $|a_2|$.

The future looks promising. We have models that give qualitative predictions for B-meson decays to states with charmonium, and new measurements which should guide the way to a still more complete understanding. In the future, both CESR, and KEK and the SLAC B factories, will provide much larger data sets. The continuation of the work in this thesis will be an important ingredient as theorists learn better how to apply QCD to the problem of hadronic B-meson decays.

Appendix A

ANGULAR MOMENTUM, SPACE AND CHARGE PARITY

A.1 Angular Momentum

There are two type of angular momentum, orbital **L** and spin **S**. In "classical" mechanics the orbital angular momentum of a particle can be defined with regard to a specific origin as $\mathbf{L} = \mathbf{r} \times \mathbf{p}$, where **L** is the angular momentum, **r** is the position vector from the origin and **p** is the momentum vector. An example component of **L** is $L_z = xp_y - yp_x$ where L_z is the component of angular momentum in the z direction, x and y are the displacement of the particle from the origin in the x and y direction, and p_x and p_y are the x and y components of the linear momentum. The magnitude of **L** is $\sqrt{L_x^2 + L_y^2 + L_z^2}$. In quantum mechanics the idea of orbital angular momentum is preserved by translating the momentum vector to its quantum mechanical equivalent. Two values can be measured at the same time: the magnitude of the angular momentum and the projection of the angular momentum in a particular direction (usually taken to

be the z direction). Both the total and z component of the orbital angular momentum are "quantized" in dimensionless integer units (i.e. 0, 1, 2, ...). For example if the total angular momentum is 2, the z projection can be -2, -1, 0, 1, or 2.

Particles also have intrinsic angular momentum called spin. Like orbital angular momentum one can measure only the magnitude and z projection of the spin at the same time. In quantum mechanics the spin is quantized in units of half integers (i.e. 0, 1/2, 1, 3/2, ...).

Angular momenta can be added together in different ways. Consider a meson. The two quarks both have spin of 1/2. The spins can be parallel or antiparallel (other orientations are not allowed). The preferred orientation (and the lowest energy state) is when the spins are antiparallel. One can equate this to two bar magnets, which "prefer" to have their N pole next to the other's S pole. The sum of the spin angular momentum is then 0. If the spins are parallel the sum is 1.

The allowed values for the total angular momentum (J) when adding orbital angular momentum to spin range from $|L-S|$ to $|L+S|$ in integer steps. For example if the two quarks are in an $\mathbf{L = 1}$ state with spins parallel then total angular momentum is either 0 ($\mathbf{J = L - S}$), 1 ($\mathbf{J = L}$) or 2 ($\mathbf{J = L + S}$). The total z component is just the simple sum of the orbital angular momentum and spin z components. In any interaction the z component of angular momentum must be conserved.

A.2 Parity and Charge Conjugation

Parity refers to what happens to a state when the x, y and z coordinates are inverted. We can write $\mathrm{P}|\psi>$ to represent the effect of inverting the coordinate system on the state ψ. If we apply the parity "operator" P twice we should get back the original state: $\mathrm{P}^2|\psi>=|\psi>$, so $\mathrm{P}|\psi>=\pm|\psi>$. For each particle or quantity we can ask whether we get + (even parity) or $-$ (odd parity).

For example a scalar quantity such as mass does not care about direction; (see Fig. A.1) its parity is even. A vector, on the other hand, changes direction; its parity is odd ($\mathrm{P}(V) = -(V)$). The cross product of two vectors ($A = i \times j$) behaves in an interesting way. When the coordinates are flipped the two vectors (i, j) point in the opposite directions but their vector cross product (A) does not; its parity is even. This kind of vector is called a pseudovector or axial vector. Each particle has a positive or negative parity. In some cases we cannot measure the intrinsic parity, so it is chosen by convention. For example, we know that a spin 1/2 particle has the opposite parity of its antiparticle but we cannot measure its parity. In other cases we can combine the information we have about a particle to deduce its parity. From the mathematical properties of orbital angular momentum we can determine the parity of all mesons. The parity of a group of particles is equal to the product of all the individual parities. Parity is conserved in electromagnetic and strong interactions, but not in weak interactions.

Charge conjugation refers to what happens to a state when negative charges are replaced by positive and vice versa. Consider an η_c. If the c quark is replaced by the $\overline{c}$ and the $\overline{c}$ is replaced by a c you still have the same particle, but with the c and $\overline{c}$ in different positions. This can be written as $\mathrm{C}|\eta_c>$. If you do the same replacement a second time you get back exactly what you started with. Thus $\mathrm{C}^2|\eta_c> = |\eta_c>$. From this we know that $\mathrm{C}|\eta_c> = \pm|\eta_c>$, but the appropriate sign is uncertain. Note that charge conjugation only makes sense when talking about neutral particles. Figuring out the intrinsic charge conjugation "parity" of a particle is a bit trickier than figuring out the space parity. Like parity, the charge conjugation value of a group of particles is the product of the individual charge conjugation values. Charge conjugation is conserved in electromagnetic and strong interaction, but like parity, not in weak interactions.

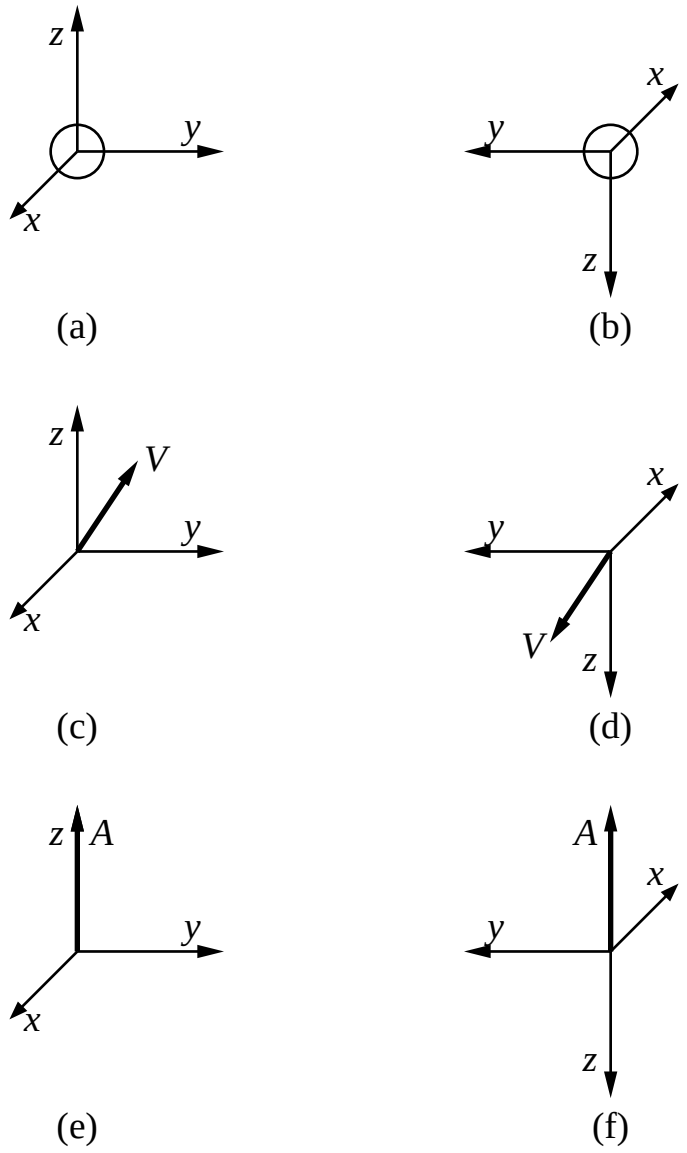

Figure A.1: Transformation of quantities under space inversion ($x \to -x$, $y \to -y$, $z \to -z$). (a) A spherically symmetric object. (b) A spherically symmetric object under space inversion, note that it is not distinguishable from the object in (a). (c) A vector. (d) A vector under space inversion. Note that this vector is the same as the vector in (c) multiplied by -1. (e) An axial vector: $A \equiv \hat{x} \times \hat{y}$. (f) The same axial vector as in (e) under space inversion. Note that this vector points in the same direction as the vector in (e).

A.3 P and C for Charmonium States

The intrinsic parity of a meson can be determined from its orbital angular momentum. If the orbital angular momentum of a $c\overline{c}$ meson is $\mathbf{L}$ then $\mathrm{P} = (-1)^{\mathbf{L}+1}$. This can be shown by noting that, one, from experiment, the parity of the π^0 is -1, and two, from wave functions under space inversion, mesons with even $\mathbf{L}$ have opposite parity of those with odd $\mathbf{L}$. The charge conjugation number is determined from both the angular momentum and spin of the meson. If the spin of a $c\overline{c}$ meson is $\mathbf{S}$ then $\mathrm{C} = (-1)^{\mathbf{L}+\mathbf{S}}$. This follows in a similar way as was used to determine P for mesons. From experiment the charge parity of the π^0 is $+1$. From examining the effect on the wave function of interchanging particles with spin $\pm\frac{1}{2}$ it can be shown that mesons in a spin singlet state ($\mathbf{S} = 0$) have opposite charge parity from those in a spin triplet state ($\mathbf{S} = 1$). Particle interchange also has the effect of space inversion on the wave functions, thus states with even $\mathbf{L}$ have opposite charge parity than states with odd $\mathbf{L}$.

Now we can systematically write down the values of P and C for the charmonium mesons. The η_c is in a 1S state, $\mathbf{L} = 0$ and $\mathbf{S} = 0$, thus $\mathrm{P} = -1$ and $\mathrm{C} = +1$. The J/ψ and ψ' have $\mathbf{L} = 0$ and $\mathbf{S} = 1$, thus $\mathrm{P} = -1$ and $\mathrm{C} = -1$. The h_c has $\mathbf{L} = 1$ and $\mathbf{S} = 0$, thus $\mathrm{P} = +1$ and $\mathrm{C} = -1$. And the χ_c states have $\mathbf{L} = 1$ and $\mathbf{S} = 1$, thus $\mathrm{P} = +1$ and $\mathrm{C} = +1$.

Appendix B

CONSERVATION LAWS IN B-MESON DECAY VIA THE COLOR SINGLET MECHANISM

Kühn, Nussinov and Rückl have stated that the inclusive decay of $B \rightarrow$charmonium X can only take place by producing the $c\overline{c}$ pair in a color singlet state. This hypothesis makes several predictions on which charmonium final states are allowed to be produced. This short section gives some of the details of the arguments.

In the absence of gluon interactions the the Hamiltonian:

$$H_W = \frac{G_F}{\sqrt{2}} \mathrm{V}_{cb} \mathrm{V}_{cs}^* (\overline{s}c)(\overline{c}b). \tag{B.1}$$

cannot produce all charmonium states. After the Fierz transformation, the production of charmonium comes from the $(c\overline{c})$ color singlet term (see Eq. 1.8). The matrix element for this is:

$$< [c\overline{c}]|\overline{c}(\gamma_\mu - \gamma_\mu\gamma_5)c|0 > \tag{B.2}$$

where $[c\overline{c}]$ represents the final charmonium state, $\overline{c}(\gamma_\mu - \gamma_\mu\gamma_5)c$ represent the creation of a c and $\overline{c}$ with a $V-A$ (Vector - Axial Vector) interaction, 0 represent the vacuum. Now one can proceed through the various charmonium states to see which are allowed. The η_c is in a $\mathrm{J^{PC}}$ state of 0^{-+}; thus it is a pseudoscalar particle. It can couple to the axial part of the V−A current through the contraction of γ_μ with the four momentum P^μ. The J/ψ and ψ' are in a 1^{--} state; thus they are vector particles. They directly couple to the vector part of the V-A current. The χ_{c1} is an axial vector (1^{++}) and thus couples directly to the axial part of the V−A current. The χ_{c0} is a scalar. It can only couple to the vector part of the $V-A$ current, however the vector part has a charge conjugation value of -1, while the χ_{c0} and the vacuum both have a C value of 1 thus the χ_{c0} can not be produced by the $V-A$ current. The χ_{c2} has similar problems. The h_c is an axial vector and thus couple to the axial part of the $V-A$ current. However it has a C value of -1 while the axial current has a C value of 1, thus it too is not allowed.

References

[1] K. Hikasa, *et al.* (Particle Data Group), "Review of Particle Properties," Phys. Rev. **D45**, 1 (1992).

[2] T.A. Armstrong, *et al.*, "Observation of the P Wave Singlet State of Charmonium," Phys. Rev. Lett. **69**, 2337 (1992).

[3] J.H. Kühn and R. Rückl, "Clues on Color Suppression From $B \to J/\psi$X," Phys. Lett. **135B**, 477 (1984). ERRATUM-ibid **B258**, 499 (1991).

[4] J.H. Kühn, S. Nussinov, and R. Rückl, "Charmonium Production in B-Decays," Z. Physik **C5**, 117 (1980).

[5] G.T. Bodwin, E. Bratten, T.C. Yuan, and G.P. Lepage, "P-wave charmonium production in B-meson decays," Phys. Rev. **D46**, 3703 (1992).

[6] M. Bauer, B. Stech, and M. Wirbel, "Exclusive Non-Leptonic Decay of D-, D*- and B-Mesons," Z. Physik **C34**, 103 (1987).

[7] M. Neubert, V. Rieckert, Q.P. Xu and B. Stech, "Exclusive Weak Decays of B Mesons," in *Heavy Flavours*, edited by A. J. Buras and H. Lindner (World Scientific, Singapore, 1992).

[8] Y. Kubota, *et al.*, "The CLEO-II Detector," Nucl. Instrum. Meth. **A320**, 66–113 (1992).

[9] D. Bortoletto, *et al.*, "A Muon Identification Detector for B Physics Near $e^+e^- \rightarrow B\overline{B}$ Threshold," Nucl. Instr. Meth. **A320**, 114 (1992).

[10] C. Bebek, *et al.*, "CLEO-II Trigger System," Nucl. Instr. Meth. **A302**, 261 (1991).

[11] C.J. Bebek, *et al.*, "A New Data Acquisition System for CLEO-II," Nucl. Instr. Methods **A338**, 447 (1994).

[12] LUND / JETSET7.3

We use a hybrid scheme where the LUND symmetric scheme is used for light quarks and a decay according to the Peterson function is used for heavy quarks (c,b).

[13] F. Berends and R. Kleiss, "Distributions in the Process $e^+e^- \rightarrow e^+e^-\gamma$," Nucl. Phys. **B228**, 537 (1983).

[14] S. Jadach and Z. Was, "KORALB Version 2.1: An Upgrade with TAUOLA Library of Tau Decays," Comput. Phys. Commun. **64**, 267 (1991).

[15] R. Brun *et al.*, "GEANT3," CERN document DD/EE/84-1 (unpublished).

[16] K. Berkelman, CLEO internal software note CSN 87-261 (1987).

[17] D.C. Cassel and H. Kowalski, "Pattern Recognition in Layered Track Chambers Using a Tree Algorithm," Nucl. Instr. Meth. **185**, 235 (1981). This article explains the DUET algorithm.

D.S. Riley, "Inclusive and Exclusive Decays of B Mesons to Charmed Vector Mesons," Cornell University Dissertation (1989). This thesis includes some details of upgrades to the DUET track finder.

[18] D. Besson, "Charged and Neutral Particle Detection Efficiency in Data and Monte Carlo," CLEO internal note CBX 93-01 (1993).

[19] D. Besson, "More on Charged and Neutral Particle Efficiency," CLEO internal note CBX 93-96 (1993).

[20] R. Wang, "Measurements of the Inclusive Semileptonic Branching Fraction of B Mesons at the Upsilon(4S) Resonance," Ph.D. Thesis, University of Minnesota (1994).

[21] B. Heltsley, CLEO internal note CBX 88-39 (1988).

[22] B. Heltsley, "CDCC Track-Shower Matching," CLEO internal note CBX 92-108 (1992).

[23] R. Talman, "On the Statistics of Particle Identification Using Ionization," Nucl. Instr. Meth. **159**, 189 (1979).

[24] T. Skwarnicki, CLEO internal software note CSN 90-301 (1990).

[25] S. Schrenk, "Two Studies of the CLEOG Muon Detector Simulation," CLEO internal note CBX 93-20 (1993).

[26] R. Wang, R. Poling and D. Perticone, "Inclusive Measurement of B-meson Semileptonic Branching Fractions," CLEO internal note CBX 93-71 (1993).

[27] B. Gittelman, C. O'Grady, and M. Sapper, "Electron Identification with CLEO II," CLEO internal note CBX 91-82 (1991).

[28] G. Fox and S. Wolfram, "Observables for Analysis of Event Shapes in e^+e^- Annihilation and Other Processes," Phys. Rev. Lett. **23**, 1581 (1978).

[29] D. Coffman. "Electromagnetic Radiative Corrections to the Process J/$\psi \to \ell^+\ell^-$," In preparation (1994).

[30] Skwarnicki T., Ph.D. Thesis, Institute for Nuclear Physics, Krakow 1986; DESY Internal Report, DESY F31-86-02 (1986).

[31] R. Poling (CLEO Collaboration), "Selected New Results from CLEO-II on c and b Decays," Proceedings of the Joint Lepton-Photon Symposium and Europhysics

Conference on High Energy Physics, eds. S. Hegarty, K. Potter and E. Quereigh, World Scientific, Singapore, 546 (1992).

[32] D. Coffman *et al.*, "Direct Measurement of the J/ψ Leptonic Branching Fraction," Phys. Rev. Lett. **68**, 282 (1992).

[33] H. Albrecht, *et al.* (ARGUS Collaboration), "First Evidence of χ_c Production in B Meson Decays," Phys. Let. **B277**, 209 (1992)

[34] L3 Collaboration (O. Adriani, *et al.*) "χ_c Production in Hadronic Z Decays," Phys. Lett. **B317**, 467 (1993).

[35] J.D. Jackson and D.L. Scharre, "Initial State Radiative and Resolution Corrections and Resonance Parameters in e^+e^- Annihilation." Nucl. Instr. Methods **128**, 13 (1975).

[36] M.S. Alam *et al.* (CLEO Collaboration), "Exclusive Hadronic B Decays to Charm and Charmonium Final States." submitted to Phys. Rev. **D** (1994).

[37] H. Fritzsch, "Seeing the B Mesons in Hadronic Collisions," Phys. Lett. **86B**, 164 (1079).

[38] M.B. Wise, "An Estimate of J/ψ Production on B Decays," Phys. Lett. **89B**, 229 (1980).

[39] T. DeGrand and T. Toussaint, "The Decay of B Quarks into ψ's," Phys. Lett. **89B**, 256 (1980).

[40] I. Bigi *et al.*, "Non-Leptonic Decays of Beauty Hadrons – from Phenomenology to Theory," Preprint UMN-TH-1234/94, to appear in the second edition of the book B **Decays**, S. Stone (ed.), World Scientific.

[41] P.H. Cox, S. Hovater, S.T. Jones, and L. Clavelli, "QCD Corrections to the Decay $B \to \psi$X," Phys. Rev. **D32**, 1157 (1985), ERRATUM-ibid D33 295 (1986).

[42] S.T. Jones and P.H. Cox, "Leading Log and α_s Corrections to the Decay $B \to \psi$X," Phys. Rev. **D35**, 1064 (1987).

[43] Buras, Gerald and Rückl, "1/N Expansion for Exclusive and Inclusive Charm Decays," Nucl. Phys. **B268**, 16 (1986).

[44] M.J. Dugan and B. Grinstein, "QCD Basis for Factorization in Decays of Heavy Mesons," Phys. Lett. **B255**, 583 (1991).

[45] N.G. Deshpande, J. Trampetic, "Estimate of Exclusive B Decays into Charmonia and K/K* Meson," Phys. Rev. **D41**, 986 (1990).

[46] M.R. Ahmady and D.-s. Liu, "Exclusive Decays $B \to$ Kψ, $B \to$ K$^*\psi$ Using Heavy Quark Symmetries," Phys. Lett. **B302**, 491 (1993).

[47] T. Browder, K. Honscheid and S. Playfer, "A Review of Hadronic and Rare B Decays," Preprint CLNS 93/1261, to appear in the second edition of the book B **Decays**, S. Stone (ed.), World Scientific (1994).

[48] B.F.L. Ward, "Theoretical Analysis of $\overline{B} \to \chi_{c1} \mathrm{K}^0_\mathrm{S}$," Phys. Rev. **D47**, 2832 (1993).